TEMPERATURE DEPENDENCE OF THE CHEMICAL SHIFT OF LIPID-DISSOLVED ^{129}XE AND ITS APPLICATIONS IN MR THERMOMETRY

Le Zhang

A dissertation submitted to the faculty of the University of North Carolina at Chapel Hill in partial fulfillment of the requirements for the degree of Doctor of Philosophy in the Department of Applied Physical Sciences.

Chapel Hill
2017

Approved by:

Tamara Branca

Jianping Lu

Sean Washburn

Yue Wu

Hong Yuan

© 2017
Le Zhang
ALL RIGHTS RESERVED

ABSTRACT

Le Zhang: Temperature Dependence of the Chemical Shift of Lipid-dissolved ^{129}Xe and Its Applications in MR Thermometry
(Under the direction of Rosa Tamara Branca)

The ability to measure tissue temperature non invasively and *in vivo* is critical to a number of applications, including the monitoring of thermal therapy in cancer patients. The resonance frequency of water protons is the most commonly used probe to measure relative temperature changes with MRI. The water proton resonance frequency (PRF) shifts linearly with temperature with a coefficient of -0.01ppm/°C for almost any tissue type and is as a result suitable to measure relative temperature changes *in vivo*. It has also been suggested that PRF could be used for absolute temperature measurements if a temperature independent resonance frequency, like that of neighboring fat spins (methylene protons), could be used to remove the effect of field drift and magnetic field inhomogeneities. Similarly, intermolecular zero-quantum coherences (iZQCs) between water and fat spins have also been suggested as a possible means of correcting for the effect of macroscopic susceptibility gradients at the microscopic scale, a scale much smaller than that typically probed by MRI.

However water and fat do not mix and water and fat tissues have very different magnetic susceptibilities. In this thesis we analyze the effect of microscopic susceptibility gradient generated at water-fat interfaces on fat-referenced PRF thermometry methods and on iZQC water-fat thermometry methods. Specifically, by using a combination of simulations and high-resolution spectroscopic measurements, we show that by referencing the water resonance frequency to that of nearby methylene protons one could obtain very inaccurate temperature measurements. We also show that the impact of microscopic susceptibility gradients is even stronger on the iZQC water-fat resonance frequency, which probes into the difference in resonance

frequencies between water and fat spins more heavily at water-fat interfaces, where microscopic magnetic susceptibility gradients the strongest.

At the same time we investigate the temperature dependence of the chemical shift of lipid-dissolved ^{129}Xe (LDX). We show that the temperature coefficient of LDX resonance frequency is 20-fold higher than that of water and it is linear within the most clinically-relevant temperature range (20~45°C) used in thermotherapies. Since LDX and methylene protons reside in the same environment, the effect of both macro and microscopic susceptibility gradients can be completely removed by referencing LDX to the nearby methylene protons, providing the opportunity to measure absolute temperature. We validated this method both *in vitro* and *in vivo* in rodents. We then applied this method in humans to directly measure the temperature of brown adipose tissue, which is a type of adipose tissue with clinical significance.

ACKNOWLEDGEMENTS

First and foremost, I would like to express my deepest gratitude to my advisor, Prof. Rosa Tamara Branca, for giving me guidance and help throughout my PhD study. Her deep knowledge of MR physics, her attention to details and her passion for our research work have never ceased to amaze me. The five years of working with here were filled with her personally teaching me how to conduct scientific experiments, patiently answering my questions, meticulously reviewing my manuscripts and generously teaching me how to become not only a better researcher but a person. Her influence on me will last far beyond my graduation.

I am also grateful to Dr. Karl M. Koshlap from Eshelman School of Pharmacy, who taught me how to operate and program a new NMR sequence on the 500MHz NMR spectrometer. A lot of the work presented in this thesis would not have been accomplished with his expertise and patient assistance.

I would like to express my special gratitude to Dr. Brian M. Dale from Siemens Healthcare. He guided me through the complicated task of pulse sequence programming in Siemens' IDEA environment, as well as the unfamiliar territory of writing coil files for a number of our xenon coils on the 3T MRI scanner. I owe a lot of the credit for our work with xenon on the Siemens scanner to his selfless and timely help.

I would like to thank Prof. Warren Warren from Duke University who allowed me to audit his NMR class in the spring of 2013 and Prof. Shumin Wang who also allowed me to sit in his MRI class in the fall of 2016. They showed me the beauty of magnetic resonance with their deep knowledge and clear explanations, as well as many beautiful applications that I had never dreamt about. The theories and techniques I learned from his class were extremely helpful for my research.

I am grateful to my committee members, Profs. Yue Wu, Sean Washburn, Hong Yuan, Otto Zhou and Jianping Lu for their advice on the research project and the valuable suggestions on my dissertation.

I have had a lot of help from the other members of Dr. Branca's Group and of BRIC. They include: Dr. Ting He, Alex Burant, Andrew McCallister and Michael Antonacci, Dr. Xiaopeng Zong, Dr. Cihat Eldeniz, and many others. My thanks also go to the BRIC human imaging and small animal imaging staff, who helped us with the scheduling of volunteers, the drafting and submitting of paperwork, the designing of protocols, and the operating of the instruments.

I also cherish the friendship I have formed over the years with fellow graduate students from the then-named Curriculum of Applied Sciences and Engineering, Drs. Yuan Chong, Lei Zhang, Yanchun Ling, Xing Zhang and Craig Cavanaugh. We came into the same office seven years ago and they have always been there to cheer me up when I was down and share my joy when my work came to fruition.

Last but not least, I want to take this opportunity to thank my family. I couldn't have achieved this without their selfless support, both financially and spiritually. Their love is priceless.

TABLE OF CONTENTS

LIST OF TABLES xi

LIST OF FIGURES xii

LIST OF ABBREVIATIONS xvi

1 Dissertation Outline 1

2 Magnetic Resonance with ^{129}Xe 3

  2.1 The Origin of NMR Signal 3

    2.1.1 Nuclear Spin Hyperpolarization of ^{129}Xe 6

  2.2 Relaxation Mechanism 10

    2.2.1 Characteristic Relaxation Times of ^{129}Xe 12

  2.3 Chemical Shift 14

    2.3.1 Characteristic Chemical Shift of ^{129}Xe 15

  2.4 Applications of HP ^{129}Xe 16

3 Effects of Microscopic Susceptibility Gradients on PRF Thermometry 20

  3.1 MR Thermometry Methods 20

    3.1.1 PRF-Based MR Thermometry 21

  3.2 Effect of Microscopic Susceptibility Gradients on PRF-based MR Thermometry: Numerical Simulations 26

    3.2.1 Mathematical Modeling of Microscopic Susceptibility Gradients 26

    3.2.2 Numerical Simulations 28

      3.2.2.1 Method Validation 28

      3.2.2.2 Simulated Geometries 29

3.2.2.3 Simulation Results 31

3.3 Effect of Microscopic Susceptibility Gradients on PRF-based MR Thermometry: Experimental Work 33

3.3.1 *In Vitro* NMR Methods 33

3.3.2 *In Vitro* NMR Results 33

3.3.3 *In Vivo* MRI Methods 35

3.3.4 *In Vivo* MRI Results 36

3.4 Discussion 38

3.5 Conclusions 40

4 Effects of Microscopic Susceptibility Gradients on Water-Fat iZQC Thermometry 41

4.1 Distance Dipolar Field and Its Applications in Magnetic Resonance 41

4.1.1 Density Matrix of an Ensemble 42

4.1.2 How to Observe Multiple Quantum Coherences 43

4.1.3 Distant Dipolar Field Interactions 44

4.1.4 Applications of IMQCs 46

4.2 MR Thermometry Using iZQC 46

4.2.1 Effects of Microscopic Susceptibility Gradients on Water-Fat iZQC Thermometry: Simulations 47

4.2.2 Effects of Microscopic Susceptibility Gradients on Water-Fat iZQC Thermometry: *In Vitro* Experiment 52

4.2.2.1 Water-fat iZQC Sequence 52

4.2.2.2 Experimental Methods 53

4.2.2.3 Experimental Results 54

4.2.3 Discussion and Conclusions 56

5 Temperature Dependence of Lipid-dissolved ^{129}Xe Resonance Frequency 58

5.1 Temperature Dependence of ^{129}Xe Resonance Frequency 58

5.2 Effects of ^{129}Xe-^{129}Xe Interaction on ^{129}Xe Resonance Frequency 63

5.3 Characterization of LDX Chemical Shift 65

5.3.1 Methods 65
5.3.2 Results 65
5.4 Discussion and Conclusions 68
6 Application of LDX-based MR thermometry 70
6.1 *In Vivo* Validation in Rodents 70
6.1.1 *In Vivo* Temperature Measurement Results in Rodents 71
6.2 *In Vivo* Application of LDX-based Thermometry in Human BAT 74
6.2.1 *In Vivo* Temperature Imaging Methods in Humans 75
6.2.2 Results of LDX Thermometry in Human BAT 76
6.2.3 Discussion and Conclusions 79
7 Distant Dipolar Field Effect and Its Applications in LDX Thermometry 80
7.1 Remote Detection of ^{129}Xe Using ^{1}H via DDF 80
7.1.1 Theory 81
7.1.2 Methods 84
7.1.2.1 Remote Detection Experimental Setup 84
7.1.2.2 Measurements of T_1 and T_2 Relaxation Times 85
7.1.3 Results 86
7.1.3.1 T_1 and T_2 Results 86
7.1.3.2 Remote Detection in Pure Ethanol 86
7.1.3.3 Remote Detection in Mixed Deuterated/undeuterated Methanol 88
7.1.4 Discussions 89
7.2 LDX-methylene iZQC MR Thermometry 91
7.2.1 Heteronuclear iZQC Sequence 91
7.2.2 Methods 96
7.2.3 Results 97
7.2.4 Discussion 99
7.2.4.1 Accuracy of LDX iZQC/iDQC methods 99

        - 7.2.4.2 Density dependence of LDX iZQC/iDQC 100
    - 7.2.5 Conclusions 101

8 Conclusions 102

REFERENCES 104

LIST OF TABLES

2.1 List of gyromagnetic ratios of several common spin-1/2 nuclei. 4

3.1 Computed resonance frequency shifts of water and fat spins caused by magnetic susceptibility field for different water-fat distributions at two different temperatures. The table also shows the temperature error made when the water-fat resonance frequency difference is used to calculate absolute temperature (abs temp) and relative temperature (rel temp) changes. 32

LIST OF FIGURES

2.1 Graphics demonstrating the generation of a net magnetization in a spin system placed in an external magnetic field. 4

2.2 Graphics demonstrating the 90°-acquisition NMR experiment. 5

2.3 Setup of the SEOP process. Reproduced from [1]. 7

2.4 Simplified schematic showing the optical pumping of rubidium, adapted from [2]. 8

2.5 Simplified schematic showing the spin exchange process between rubidium and xenon, adapted from [3]. 9

2.6 Graphics describing the T_1 and T_2 relaxation mechanisms. 11

2.7 Xenon spectrum acquired after inhalation of HP ^{129}Xe from a human subject. (a) NMR spectrum obtained using a hard, 7° RF pulse. The gaseous HP ^{129}Xe signal is used as the 0ppm reference. (b) Spectrum from a selective, 7° pulse centered at 218ppm. Reproduced from [4]. 16

2.8 (a) Coronal HP ^{129}Xe GRE images of lungs showing various degree of airway obstructions due to mucus accumulation. (b) Sagittal slices of 3D UTE proton images with the yellow circles highlighting the possible sites of mucus in the airways. (c) Post-mortem histology results showing mucus. 18

3.1 Illustration showing the impact of lipid spins to the change of the phase of net magnetization. The blue vector is a sum of the corresponding fat and water vectors. 23

3.2 Cartoon illustrating the relation between the variables in Equation 3.5. 27

3.3 Comparison between the numerical simulation results presented in [5] (dashed line in (a)) and our results (b) for a straight line crossing the center of the spherical geometry along the y-direction. 29

3.4 Comparison between the numerical simulation results presented in [5] (dashed line in (a)) and our results (b) for the cylindrical geometry. 29

3.5 Water-fat distribution patterns simulated in this study. The yellow color represents the fat compartment while the blue color represents the water compartment. 30

3.6 The susceptibility field maps reported for the center YZ slice (dotted square in Fig.3.5(a)), which are produced by the magnetic susceptibility mismatch between water and fat compartments. 32

3.7 ^{1}H spectra acquired on the rWAT sample. (a) ^{1}H spectrum at 34°C. (b) Shift of the methylene resonance frequency line with temperature. (c) Shift of the water resonance frequency line with temperature. 34

3.8 Temperature dependence of water and methylene resonance frequencies for five different adipose tissue samples under different xenon gas pressures. (a) Temperature dependence of the methylene resonance frequency. (b) Temperature dependence of the water resonance frequency. (c) Temperature dependence of the water-methylene resonance frequency difference. 35

3.9 Frequency and temperature maps acquired *in vivo* from an obese mouse. (a) Anatomical image showing the slice selection. (b) Representative CSI spectral from a voxel in the abdomen. (c~e) Relative temperature maps calculated from fat-referenced PRF frequency. (f~h) Relative temperature change maps calculated from fat-referenced PRF frequency. 37

3.10 Frequency and temperature maps acquired *in vivo* from another obese mouse. (a) Water, methylene and water-methylene resonance frequency maps. (b) Temperature maps showing the relative temperature change between the two measurements. 38

4.1 (a) Uniform distribution of magnetization in the sample. (b) Symmetry is broken up by the application of pulsed gradient in the CRAZED sequence. Adapted from [6]. 45

4.2 (a) Modified CRAZED sequence diagram. (b) Sketch showing two spin species residing in different compartments. (c) Sketch showing two spin species residing in the same compartments in an inhomogeneous field. 48

4.3 Plot of the $F(r/d_c)$ function calculated using Equation 4.12, which shows that most of the iZQC signal originates from spins that are about 1 correlation distance away. 50

4.4 Frequency offset generated by water/fat susceptibility mismatch for (a) a $50\mu m$-diameter fatty droplet and (b) a $100\mu m$-diameter fatty droplet. 50

4.5 Computed water-fat iZQC frequencies for the geometries shown in Fig.4.4 as a function of correlation distance d_c. 51

4.6 Water-fat iZQC sequence used in this study as a modification to the original CRAZED sequence. 53

4.7 2D spectra acquired from the WAT/Muscle sample at four temperatures showing the water-methylene iZQC peak between water and fat spins. 54

4.8 Dependence on correlation distance and temperature displayed by water-fat iZQC frequency. 55

5.1 Schematic showing a xenon atom diffusing through a polymer matrix. Reproduced from [7]. 60

5.2 Potential $U(y)$ described in Equation 5.3 for a xenon atom in a layerlike pore as a function of the position of the xenon atom and layer separation. Reproduced from [7]. 61

5.3 Schematic showing the simplification of the potential energy as paired double quantum-well. Reproduced from [7]. 63

5.4 (a) Example of an LDX spectrum at 26°C for the rWAT sample. (b) Drifting of the LDX peak with temperature. (c) MATLAB fitting of the peak shown in (a) using a Voigt peak shape. . . . 66

5.5 (a) LDX spectra at 26°C for the rWAT sample at different xenon gas pressures. (b) Temperature and pressure dependence of LDX resonance frequency. (c) Temperature and pressure dependence of LDX-methylene resonance frequency difference. . . . 67

6.1 *In vivo* temperature maps obtained from an obese mouse using the LDX frequency as temperature sensor. (a) Coronal view showing the selected axial slice. (b) LDX temperature map overlaid on the axial ^{1}H reference image. (c)~(e) LDX temperature maps acquired with the mouse body temperature equilibrated at 3 different temperatures. (f)~(h) Relative temperature change maps showing the correct average temperature change (2°C for f and g, and 4°C for h). . . . 72

6.2 LDX and LDX-methylene resonance frequency maps acquired *in vivo* from an obese mouse. . . . 73

6.3 (a) and (b) Absolute temperature maps calculated *in vivo* for the same mouse shown in Fig.6.2. (c) Temperature dependence of LDX-methylene resonance frequency obtained from both *in vitro* and *in vivo*. . . . 74

6.4 Setup of *in vivo* human scans with HP ^{129}Xe. . . . 76

6.5 HP ^{129}Xe spectra obtained in one of the subjects analyzed at thermoneutrality (a) and cold exposure (b). (c) HP LDX image in BAT obtained in the same subject showing intense xenon uptake in the supraclavicular fat region. . . . 77

6.6 Temperature maps calculated using fat-referenced LDX resonance frequency and *in vitro* calibrations at three stages of the study in the second lean subject. . . . 78

6.7 (a) The position of the SVS voxel and region of homogeneous B_0 field in the second lean subject. (b) HP LDX image in BAT obtained using gradient echo sequence during cold exposure (after the acquisition of the spectrum in Fig.6.6(e). . . . 79

7.1 Indirect detection acquisition scheme. (a) Pulse sequence originally proposed by [8]. (b) Modified sequence developed in this study. . . . 81

7.2 Experimental setup for gas exchange in the NMR tube. . . . 85

7.3 2D spectra acquired on the pure ethanol membrane sample. (a): 2D spectrum using xenon as the sensor without t_1 correction. (b): F1-projection of the 2D spectrum (a), which is normalized to the maximal intensity of spectrum (d). (c): 2D spectrum using xenon as the sensor with t_1 correction. (d): F1-projection of the 2D spectrum (c). (e): 2D spectrum using proton as the sensor without t_1 correction. (f): F1-projection of the 2D spectrum (e), which is normalized to the maximal intensity of spectrum (h). (g): 2D spectrum using xenon as the sensor with t_1 correction. (h): F1-Projection of 2D spectrum (g). . . . 87

7.4 2D spectra acquired on the mixed deuterated/undeuterated methanol sample. (a): 2D spectrum using xenon as the sensor with t_1 correction. (b): Projection of spectrum (a) onto the indirectly detected dimension. (c): 2D spectrum using proton as the sensor with t_1 correction. (d): Projection of spectrum (b) onto the indirectly detected dimension. 89

7.5 Heteronuclear iZQC sequence used in this study. (a) Heteronuclear iZQC sequence. (b) Modified version of the inhomogeneity-free iDQC/iZQC sequence proposed in [9]. 92

7.6 2D spectra acquired on the WAT/Muscle sample at four temperatures showing the LDX-methylene iDQC/iZQC cross peak. 97

7.7 Dependence on correlation distance and temperature of the LDX-methylene iZQC/iDQC frequency. 98

7.8 ^{1}H-^{31}P iZQC and iDQC/iZQC resonance frequencies (a&c) and linewidths (b&d) as measured for phosphoric acid as a function of the correlation distance. 99

LIST OF ABBREVIATIONS

α or FA	Flip Angle
B_0	Main external magnetic field
B_1	Radiofrequency magnetic field
BAT	Brown Adipose Tissue
BIR4	B_1-Insensitive Rotation-4
BW	BandWidth
CPMG	Carr-Purcell-Meiboom-Gill
CRAZED	Correlated 2D spectroscopy Revamped by Asymmetric Z-gradient Echo Detection
CSI	Chemical Shift Imaging
DDF	Distant Dipolar Field
F1	Indirect dimension of 2D spectroscopy
F2	Direct dimension of 2D spectroscopy
FLASH	Fast Low Angle SHot
FFT	Fast Fourier Transform
FID	Free Induction Decay
FOV	Field Of View
FWHM	Full Width at Half Maximum
γ	Gyromagnetic ratio
GRE	Gradient-Recalled Echo
HP	Hyperpolarized
IACUC	Institutional Animal Care and Use Committee
IRB	Internal Review Board
iMQC	intermolecular Multiple-Quantum Coherence

iZQC	intermolecular Zero-Quantum Coherence
LDX	Lipid-dissolved Xenon
MRgFUS	Magnetic Resonance-guided Focused UltraSound
MRI	Magnetic Resonance Imaging
MRT	Magnetic Resonance Thermometry
NMR	Nuclear Magnetic Resonance
ω_0	Lamour frequency
ppm	parts per million
PRF	Proton Resonance Frequency
RF	Radio Frequency
SEOP	Spin-Exchange Optical-Pumping
SNR	Signal-to-Noise Ratio
SVS	Single Voxel Spectroscopy
T_1	Longitudinal relaxation time
T_2	Transverse relaxation time
T_2*	Transverse relaxation time in the presence of field inhomogeneity
TE	Echo Time
TI	Inversion Time
TR	Repetition Time
SW	Spectral Width

CHAPTER 1: DISSERTATION OUTLINE

In this dissertation, I will analyze one of the shortcoming of conventional proton resonance frequency (PRF) based MR thermometry methods when they are applied to tissues that contain fat. I will then propose an alternative method for MR thermometry in fatty tissues that uses the temperature dependence of the chemical shift of lipid-dissolved xenon.

In Chapter 2, I will give a brief review of the concepts that are pivotal to this work, outlining some of the known NMR properties and applications of hyperpolarized xenon gas in magnetic resonance imaging and spectroscopy.

In Chapter 3, I will examine the effect of microscopic susceptibility gradients on PRF-based MR thermometry methods by using both simulations and experimental results, *in vitro* and *in vivo*. I will show that in tissues that contain fat, conventional proton MR thermometry methods can provide very inaccurate temperature measurements.

In Chapter 4, I will assess the effect of microscopic susceptibility gradients on water-fat iZQC MR thermometry methods, proposed as a way to obtain more accurate relative and absolute temperature information in presence of fat. I will show that the water-fat iZQC resonance frequency strongly depends on the distribution of water and fat spins at the microscopic level and therefore cannot be used for absolute temperature measurements.

In Chapter 5, I will fully characterize the temperature dependence of the chemical shift of lipid-dissolved xenon by high resolution NMR spectroscopy.

In Chapter 6, I will use this temperature dependence to directly measure relative and absolute tissue temperature in vivo in both rodents and human subjects.

In Chapter 7, I will investigate the use of distant dipolar field effects between ^{1}H nuclear spins and ^{129}Xe nuclear spins to indirectly detect ^{129}Xe resonance frequencies and to obtain even more accurate temperature measurements *in vivo*.

Finally, I will give a summary of the work I have done.

CHAPTER 2: MAGNETIC RESONANCE WITH ^{129}XE

NMR and MRI are techniques widely used in medical imaging thanks to their high specificity and non-destructive nature. In this chapter, I will provide a brief introduction to several basic concepts of NMR and MRI: namely how the NMR signal is generated, the origin of the chemical shift, some of the relaxation mechanisms such as spin-lattice (T_1) relaxation and spin-spin (T_2) relaxation. I will also provide a brief description of the process used to enhanced the nuclear spin polarization of xenon, as well a description of some of the NMR properties and applications of HP ^{129}Xe in magnetic resonance.

2.1 The Origin of NMR Signal

In the classic picture of NMR, a spin can be thought of as a bar magnet. Therefore, when it is placed in a magnetic field B_0 at a certain temperature T, it will align itself either with (referred to as "spin up" state, or α) or against ("spin down", or β) the magnetic field, as shown in Fig.2.1. For an ensemble of N spins, the difference between the numbers of spin-up and spin-down is dictated by the Boltzmann distribution:

$$M_0 = N \times p = |N_\alpha - N_\beta| \propto N_0 \frac{\Delta E}{k_B T} = N_0 \frac{\gamma \hbar B_0}{k_B T} \tag{2.1}$$

where p is the "nuclear polarization" of the ensemble, k_B is the Boltzmann constant, ΔE is the difference in energy between the two states, $\hbar$ is the Planck's constant and γ is the gyromagnetic ratio of the nucleus.

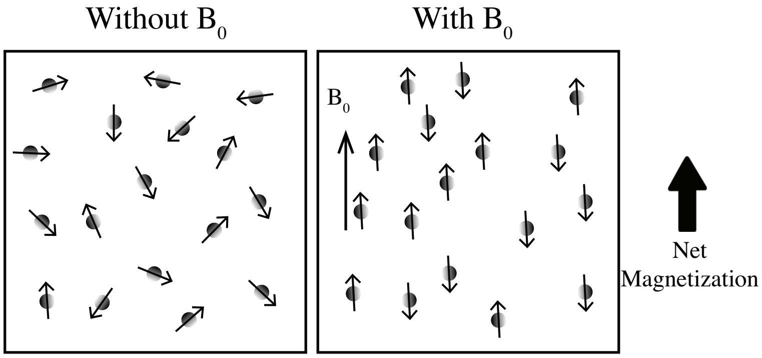

Figure 2.1: Graphics demonstrating the generation of a net magnetization in a spin system placed in an external magnetic field.

The net magnetization M_0 can then be represented as a single vector precessing about the external magnetic field (which we assume to be aligned along the z-axis), with a Hamiltonian of $H = -\gamma B_0 I_z$. The angular frequency $\omega_0 = -\gamma B_0$ is defined as the Larmor Frequency, which is unique to the type of nucleus and proportional to the strength of the magnetic field the spins are in. Table 1.1 shows the gyromagnetic ratios of some of the most commonly detected spin-1/2 nuclei in NMR and MRI [10]. For a nucleus with a positive γ such as ^{1}H, the lower energy state is the one with the nuclear spin aligned along the field B_0, also called the α state. The opposite is true for nuclei with a negative γ.

Nucleus	Natural Abundance (%)	$\frac{\gamma}{2\pi}$ (MHz/T)
^{1}H	~100	42.576
^{3}He	0.000137	-32.434
^{13}C	1.1	10.705
^{15}N	0.37	-4.316
^{19}F	~100	40.052
^{31}P	~100	17.235
^{129}Xe	24.4	-11.777

Table 2.1: List of gyromagnetic ratios of several common spin-1/2 nuclei.

In the fixed frame of reference (or the lab frame of reference), the net magnetization precesses at the Larmor frequency ω_0. However, many of the NMR concepts become easier to understand if we use a rotating frame of reference, rotating around the z-axis at the Larmor frequency ω_0. In this dissertation, unless otherwise specified, we will conduct the analysis of NMR phenomena in the rotating frame of reference, with the coordinates being (x',y',z').

In this rotating frame, at thermal equilibrium, the net magnetization is aligned along the z-axis and cannot be detected. In the simplest NMR experiment, in order to detect M_0, a radiofrequency (RF) pulse is used to rotate the magnetization onto a plane orthogonal to the main field B_0. The RF pulse lasts for a duration of t and consists of a magnetic field B_1 applied either along the x' or y' axis. During the application of RF pulse, the spins will rotate around B_1 at a rate of $\omega_1 = \gamma B_1$. If $\gamma B_1 t = \pi/2$, the magnetization will be rotated from the z'-axis and onto the $x'y'$-plane, which corresponds to the xy-plane in the lab frame of reference. The precession of the magnetization on the xy-plane induces a current in the RF coil and give rise to the observation of the Free Induction Decay (FID) in the time-domain. The Fourier transform of the FID will then yield the NMR spectrum, which contains information about the resonance frequency of the precessing spins. This process is shown in Fig.2.2. The signal-to-noise ratio of such an experiment is proportional to [11]:

$$SNR \propto N \cdot p \cdot \gamma_e \cdot \sqrt{\gamma_d^3 \cdot B_0^3 \cdot t}, \tag{2.2}$$

where γ_e and γ_d are the gyromagnetic ratios of the spins being excited and detected, respectively, and t is the acquisition time of the NMR experiment.

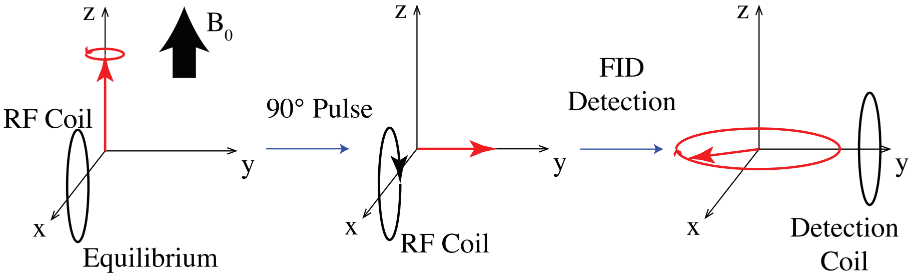

Figure 2.2: Graphics demonstrating the 90°-acquisition NMR experiment.

From Equation 2.2 we can easily conclude that the SNR is directly proportional to the number of spins N in the sample and the nuclear spin polarization p. In the typical field strengths used in NMR and MRI and at room temperature, the nuclear spin polarization level is very small. This is because the thermal energy $k_B T$ is much larger than ΔE in Equation 2.1. For example, for ^{1}H spins in a 3T magnetic field at room temperature of 298K, the energy difference between the two states will be only ΔE=$\hbar\gamma_H B_0$=8.46×$10^{-26}J$, whereas $k_B T$=4.14×$10^{-21}J$. This means that the number of excess spins in the lower energy state will be about 20 spins in every 10^6 spins. Because of the low polarization level even at relatively high magnetic field strength, NMR and MRI is often performed by detecting the nuclear spins of hydrogen atoms, which are highly abundant in living organisms in the form of water. For other, less abundant nuclei such as ^{13}C and ^{15}N, the low polarization density is a major obstacle for the detection of the NMR and MRI signal. Ways to overcome this issue include the use of cryogenic probes in NMR [12–14], of ultra-high magnetic fields [15–19], of hardware with improved sensitivity and proficiency [20–22], and of hyerpolarization techniques [23–28].

2.1.1 Nuclear Spin Hyperpolarization of ^{129}Xe

For atoms with a very low density and low gyromagnetic ratio, like xenon gas, nuclear hyperpolarization techniques are also needed to enhance the nuclear polarization by 4~5 orders of magnitude and boost the strength of the NMR signal. For xenon gas, the hyperpolarization technique most commonly used is spin-exchange optical-pumping (SEOP). In SEOP one first polarizes the electron spin of alkali atoms, in our case rubidium, by using circularly polarized laser light. The electron spins polarization is then transferred to the xenon nuclear spin via the hyperfine interaction. The typical SEOP setup is shown in Fig.2.3.

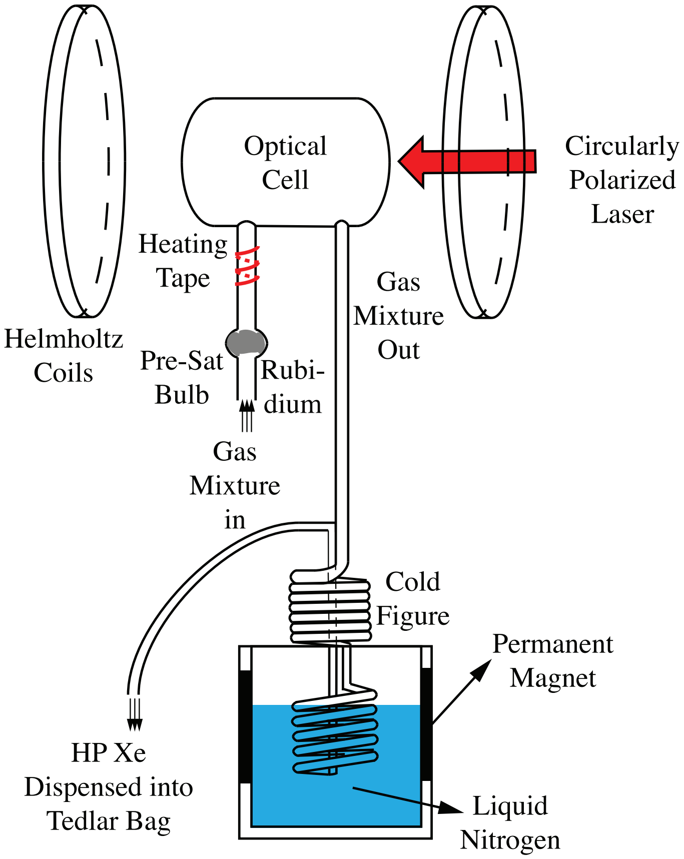
Optical Cell
Circularly Polarized Laser
Heating Tape
Helmholtz Coils
Gas Mixture Out
Pre-Sat Bulb
Rubi-dium
Gas Mixture in
Cold Figure
Permanent Magnet
HP Xe Dispensed into Tedlar Bag
Liquid Nitrogen

Figure 2.3: Setup of the SEOP process. Reproduced from [1].

During the SEOP process, an optical cell containing Rb atoms is typically heated using heated air to up to 80~200°C, well above the melting point of Rb at 39°C. This provides an optically thick Rb vapor, with a density of 10^{12} to $10^{15}/cm^3$ [29]. The pair of Helmholtz coils provides the polarization field necessary to separate the energy levels of rubidium through Zeeman splitting [30]. A lean mixture of xenon (1~5%, either enriched ^{129}Xe or at natural abundance), helium (89%) and nitrogen gases are flowed into the cell at a rate of 1~2 SLM (standard liter per minute). The low concentration of xenon is key to minimizing the spin destruction caused by binary xenon-xenon collisions [31]. To initiate optical pumping, the thick rubidium vapor is illuminated by a circularly-polarized laser tuned to the D1 transition of Rb at λ=794.7nm. This is the energy difference between the highest-occupied $5s_{1/2}$ and the lowest-unoccupied $5p_{1/2}$ orbits. The D1 adsorption line is further pressure-broadened with the added helium to increase the efficiency of optical pumping [32]. The absorption of the photon prompts a selective excitation of rubidium electrons from one of the two ground states. If the laser has a positive helicity of σ_+, the only allowed transition will have a change in its spin quantum number of Δm_s =+1, or from $s_{-1/2}$ to the first excited state of $p_{+1/2}$. However, the other possible transition is prohibited by the selection rule. The electron will then relax back to one of the two ground states. According to the Clebsch-Gordon coefficients, the probability of an electron relaxing back to $5s_{-1/2}$ is 2/3 while the probability of an electron relaxing back to $5s_{+1/2}$ state is 1/3. However, since spins on the $s_{-1/2}$ state are being continuously pumped up, a net accumulation of spins will occur on the $s_{+1/2}$ state. The role of the N_2 and helium gases, especially the latter, is to mix the two excited atomic sub-levels to further enhance the efficiency of optical pumping [33]. They also serve to reduce the lifetime that electrons spend on the excited state [34]. The N_2 gas also quenches the radiative emissions from excited rubidium, which can lead to randomly polarized photons that can be reabsorbed by polarized rubidium and reduce optical pumping efficiency [35, 36]. In summary, the net result of optical pumping will be that, theoretically, on average, 2 photons will be needed to pump one electron to the $5s_{+1/2}$ state. A simplified schematic of this process is shown in Fig.2.4, adapted from [2].

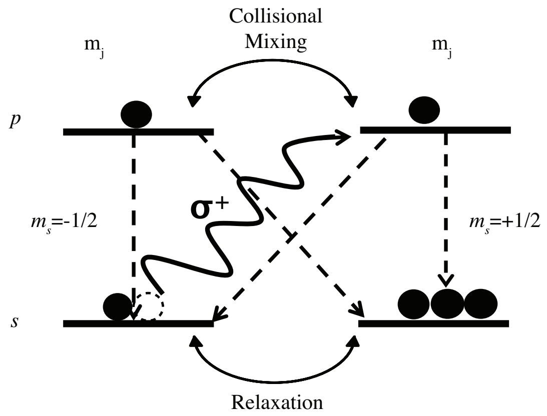

Figure 2.4: Simplified schematic showing the optical pumping of rubidium, adapted from [2].

After optical pumping, polarized rubidium can decay back to the $s_{-1/2}$ state and return to thermal equilibrium. Several factors can cause Rb depolarization: collisions between rubidium atoms, collisions of rubidium atoms with the wall of the optical cell, and collisions between rubidium and xenon atoms. The last factor transfers the polarization state of rubidium to xenon through spin exchange. A simplified schematic of this process is provided in Fig.2.5 [3]. The end result is that the electron polarization of rubidium is transferred to the spin polarization of xenon through one of two mechanisms. The first one, dominant at high pressures, is binary collisions, characterized by a short interaction time and an inefficient spin-exchange rate [37]. The second mechanism, dominant at lower pressures, is through van der Waals interactions, which are facilitated by the presence of a third body gas molecule, such as nitrogen, helium or free xenon. The spin exchange rate for such interactions is usually much larger than that for binary collisions, due to the longer residency time of rubidium spins in the vicinity of xenon atoms. The binding energy of a van der Waals molecule is roughly 20 meV [38], low enough that it can be broken up by a single collision with other molecules, resulting in a short lifetime of about $10ps \sim 100ns$. Once depolarized, the rubidium atom is free to absorb another laser photon, spin exchange with an unpolarized xenon atom, and repeat the entire process. During continuous-flow SEOP, polarized xenon continuously flows out of the optical cell and into a cold trap called cold finger. The cold finger is submerged into a liquid nitrogen dewar, which can solidify xenon while letting other gases escape through an outlet. The pure xenon ice is stored between two permanent magnets to preserve its polarization until enough xenon has been collected, at which point the liquid nitrogen dewar is removed and the cold finger is rapidly warmed up with warm water, and xenon is thawed and collected into a Tedlar bag for later use. Over the years we have made several improvements to the polarization process [1, 39], and the current achievable final xenon polarization level ranges from 10% to 25%, depending on temperature, pressure and flow rate conditions,

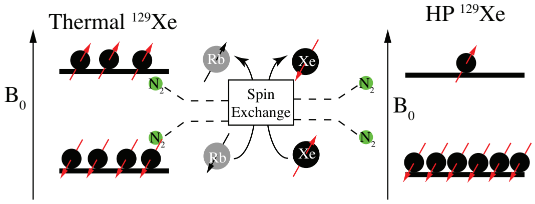

Figure 2.5: Simplified schematic showing the spin exchange process between rubidium and xenon, adapted from [3].

2.2 Relaxation Mechanism

When the magnetization is rotated on the xy-plane, the ensemble of spins is perturbed from thermal equilibrium. As a result, sooner or later the spin system will spontaneously return to thermal equilibrium via a process called “relaxation”. In the classical picture, the Bloch equation is used to describe the evolution of the magnetization [40]:

$$\frac{\mathrm{d}M_x}{\mathrm{d}t} = \gamma(\vec{M} \times \vec{B})_x - \frac{M_x}{T_2}; \tag{2.3a}$$

$$\frac{\mathrm{d}M_y}{\mathrm{d}t} = \gamma(\vec{M} \times \vec{B})_y - \frac{M_y}{T_2}; \tag{2.3b}$$

$$\frac{\mathrm{d}M_z}{\mathrm{d}t} = \gamma(\vec{M} \times \vec{B})_z - \frac{M_z - M_0}{T_1}. \tag{2.3c}$$

Without the loss of generality, after the magnetization has been tipped onto the -y-axis by a 90° excitation pulse applied along the x-axis, its evolution can be described by:

$$M_x = M_0 \sin(\omega t) \exp(-\frac{t}{T_2}); \tag{2.4a}$$

$$M_y = -M_0 \cos(\omega t) \exp(-\frac{t}{T_2}); \tag{2.4b}$$

$$M_z = M_0 - M_0 \exp(-\frac{t}{T_1}), \tag{2.4c}$$

where T_1 and T_2 are relaxation time constants.

The T_1 relaxation time, or longitudinal relaxation time, describes the return of the magnetization to thermal equilibrium. During this process, the energy is transferred from the spins system to the surroundings, or lattice. Consequently, T_1 is also frequently referred to as the spin-lattice relaxation time. As M_z is invisible to the detecting coils, T_1 relaxation causes a gradual reduction of signal intensity in the FID. A pictorial representation of T_1 relaxation is shown in Fig.2.6(a).

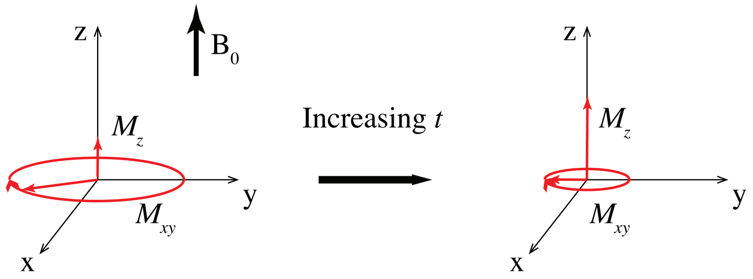

a T_1 Relaxation

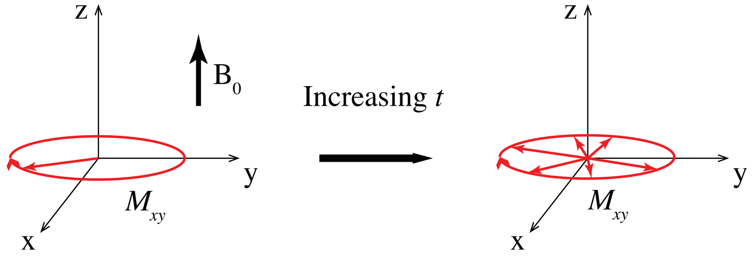

b T_2 Relaxation

Figure 2.6: Graphics describing the T_1 and T_2 relaxation mechanisms.

The T_2 relaxation time, or transverse relaxation time, describes the loss of coherence among spins due to thermal and spatial fluctuations of the z-component of the magnetic field at a microscopic level. It has contributions from two sources. The first are the inhomogeneities in the external magnetic field B_0. Their contribution is called T_2^*. This can be caused by a variety of factors such as distortion in the magnetic field line caused by the presence of the samples or by susceptibility mismatches at the interfaces between different tissues or between tissue and air. This contribution can be only partially eliminated through shimming [41]. In a system of multiple spins, the precession of each individual spin can introduce field disturbances in its vicinity, slightly altering the processing angular frequency of spins residing nearby, which in turn changes the magnetic field the first spin experiences and eventually its processing frequency. Consequently spins at different spatial locations will have slightly different frequencies, leading to a loss of phase coherence and ultimately reducing the net magnetization on the xy-plane to zero even before returning to thermal equilibrium through T_1 relaxation. T_2 relaxation manifests itself as a broadening and/or distortion of the resonance frequency lines in the NMR spectrum. A pictorial representation of T_2 relaxation is shown in Fig.2.6(b).

2.2.1 Characteristic Relaxation Times of ^{129}Xe

While the nuclear spin of the hydrogen atom has a T_1 relaxation time of few seconds, the nuclear spin of ^{129}Xe has a relaxation time that varies between few tens of seconds to up to hours, depending on the environment in which the gas resides. The first intrinsic cause of ^{129}Xe relaxation is the spin-rotation relaxation in short-lived xenon dimers, which are formed by two-body collisions. The T_1 time of xenon as function of its density scales as $\frac{1}{T_1} = 56\times\rho_{Xe}$, with T_1 and ρ_{Xe} having units of hours and amagats, respectively [42]. However, the "stickiness" of xenon gives rise to a second and more detrimental type of dimer, which is bounded via van der Waals interactions and further reduces the T_1 time by $T_1^{vdW} = T_1^{Xe-Xe}(1 + r\frac{[\rho_B]}{[\rho_{Xe}]})$ [43, 44]. As a result, it is common practice to mix xenon with a buffer gas (for example He or N_2) with a certain density of ρ_B and a specific destruction rate r [43, 44] to slow down or break up the formation of van der Waals dimers. Nonetheless this factor typically drives the T_1 time down to ~5 hours. The extrinsic factors include transverse magnetic field gradients $|\Delta B_\perp|$ in which xenon diffuse with a diffusion coefficient of D_{Xe}, which is given by $\frac{1}{T_1^{diff}} = D_{Xe}(\frac{|\Delta B_\perp|}{B_0})^2$ [45]. In a homogeneous field, T_1^{diff} can be on the order of 100 hours and safely ignored. Another extrinsic factor relates to the relaxation caused by collisions of xenon atoms with the inner walls of the container, which can be modeled as $\frac{1}{T_1^{wall}} = \eta\frac{S}{V}$, with S/V being the surface-to-volume ratio of the container and η being a constant describing the interactions between xenon and para- or ferromagnetic impurity centers in its inner surface [46]. A common solution to reduce this contribution is by coating the inner surface of the container with silane/siloxane based coatings [47], which can increase T_1^{wall} to ~3 hours. With a right combination of buffer gas, magnetic field homogeneity and container coating, the overall T_1 time of gaseous xenon can become as high as 11 hours [48, 49].

In vivo, one of the major xenon T_1 relaxation agents is the paramagnetic oxygen, whose two unpaired electrons can reduce the T_1 of gaseous HP ^{129}Xe to just a few seconds. Oxygen relaxation can be described by $\frac{1}{T_1} = \kappa p_{O_2}$, where κ is a constant whose value for ^{129}Xe/oxygen is $3.73\times10^{-6} s^{-1}\mathrm{Pa}^{-1}$ [50], and p_{O_2} is the partial pressure of oxygen. Experimental data from various studies showed good correlation between theoretically predicted and experimentally measured T_1 results, determined to be in the range of 5~30*s* [50–54]. Xenon has a significant solubility in tissues, where its T_1 drops to just few seconds. In blood, for example, the T_1 time ranges from 5~20*s*, with a dependence on the field strengths, blood oxygenation level and temperature [55–57]. Albert *et al.* [58] found that the T_1 of HP ^{129}Xe in deoxygenated blood was much shorter than in oxygenated blood and concluded that the interaction with paramagnetic deoxyhemoglobin was the major contributor to relaxation [59]. Tseng *et al.* [60], on the other hand, studied the T_1 relaxation times of HP ^{129}Xe in blood foams and found the opposite effect due to interaction with dissolved paramagnetic oxygen. However, this conclusion was very likely overestimated by the use of foam, which had an inflated surface-to-volume ratio. Once HP ^{129}Xe reaches the target organ, the T_1 relaxation time depends on the type of tissue it dissolves in. For example, Choquet *et al.* measured the T_1 time in rat brain to be (3.6±2.1)*s* at 2.35T [61]. Even though the relaxation time is short, Wagshul *et al.* demonstrated through MRS experiments in mice that the peak corresponding to HP ^{129}Xe dissolved in lung parenchyma and blood reached its maximal intensity 5~10 seconds after inhalation, while that corresponding to HP ^{129}Xe dissolved in distant, well-vascularized organs (*i.e.* heart) reached its maximal intensity 20~30 seconds after inhalation [62], indicating that xenon could reach distant organs while preserving sufficient polarization. More importantly, over time the intensity of the dissolved phase peaks reached 30%~80% of that of the gaseous peak in the lungs, which means that a large portion of polarized spins did reach distant organs and images with sufficient SNR could be generated as a result.

As for the T_2^* relaxation time of HP ^{129}Xe, one source of rapid relaxation is the bulk magnetic susceptibility gradients present at the interfaces of different tissue types. In pulmonary MRI, where HP ^{129}Xe is widely used as a contrast agent, such effect is prominent, due to the numerous air-tissue interfaces between alveoli and tissue [63]. The T_2^* time as a result becomes much smaller than the intrinsic T_2 time of HP ^{129}Xe. Chen *et al*. measured the T_2^* times of HP ^{129}Xe to be $40.8ms$ in the trachea and $18.5ms$ in the intrapulmonary airspaces [64]. In more homogeneous medium, such as blood, the T_2^* relaxation time of HP ^{129}Xe was determined to be slightly longer at $(135\pm29)ms$ [65].

2.3 Chemical Shift

One of the most attractive properties of a nuclear spin is its chemical shift. Chemical shift reflects the electronic environment the nucleus sits in. Electrons shield the nucleus from the the external magnetic field B_0 by creating an opposite field B_e such that the magnetic field felt by the nucleus is reduced to $B_0 - B_e$. The result is that the nucleus has a resonance frequency that is slightly different from its Larmor frequency. The difference between this frequency and the Larmor frequency is referred to as chemical shift. The chemical shift depends on the strength of the magnetic field. To make it field-independent, chemical shift is usually expressed in units of ppm:

$$\delta = 10^6 \times \frac{\omega - \omega_0}{\omega_0}. \tag{2.5}$$

The chemical shift is often expressed with respect to a reference chemical agent. For ^{1}H and ^{13}C, Tetramethylsilane (TMS) can be used as such an agent.

Chemical shift is an extremely important indicator of the local chemical structure and environment. In this dissertation, we will refer to the chemical shifts of water and methylene spins, which are at approximately 4.7ppm and 1.3ppm from TMS, respectively, at room temperature [66]. We will also refer to the chemical shift of xenon, which samples a wide range of values. With respect to its gaseous phase peak, the dissolved phase have a chemical shift of between 180ppm and 220ppm [67, 68]. The temperature dependences of these chemical shifts is at the core of this work.

2.3.1 Characteristic Chemical Shift of ^{129}Xe

^{3}He and ^{129}Xe are two of the most widely used gaseous contrast agents in MRI. Unlike ^{3}He, ^{129}Xe atoms can freely diffuse across the pulmonary-capillary barrier [69], dissolve into the blood stream [70], and be carried into an array of distal tissues, especially fat-rich tissues [71]. Moreover, xenon also displays a wide range of chemical shift of up to 220ppm from its gaseous peak, larger than any other biophysically relevant nucleus. This is caused primarily by the large electron cloud of xenon that is distorted when interacting with surrounding atoms. A typical xenon spectrum acquired from a human subject is shown in Fig.2.7 [4]. The spectrum shows a strong gas phase peak at 0ppm, which corresponds to xenon gas inside the alveolar spaces of the lungs and accounts for ~98% of all inhaled xenon magnetization [72]. Two dissolved phase peaks appeared upfield from the gas phase peak. The first peak corresponds to xenon dissolved in the parenchymal tissue of the lungs and in blood plasma, and typically has a chemical shift of ∼196ppm. The second peak, typically having a chemical shift of 200~221ppm, is assigned to xenon dissolved in red blood cells (RBCs). However, the determination of the exact chemical shifts of the dissolved phases is extremely difficult. Ideally, the 0ppm should be assigned to the gas peak of xenon at a partial pressure of 0 Pascal, which is practically impossible to detect. Another issue with this referencing system is that the spins that give rise to these peaks reside in different body or tissue compartments where the magnetic field is known to shift by as much as 3ppm downfield from the lungs [62]. As a result, the relative positions of the peaks vary between tissue types and between species (*i.e.* humans and rodents) [73–77]. As a result, the value of the chemical shift of xenon dissolved in a specific tissue is still subject to ongoing investigation and debate [78, 79].

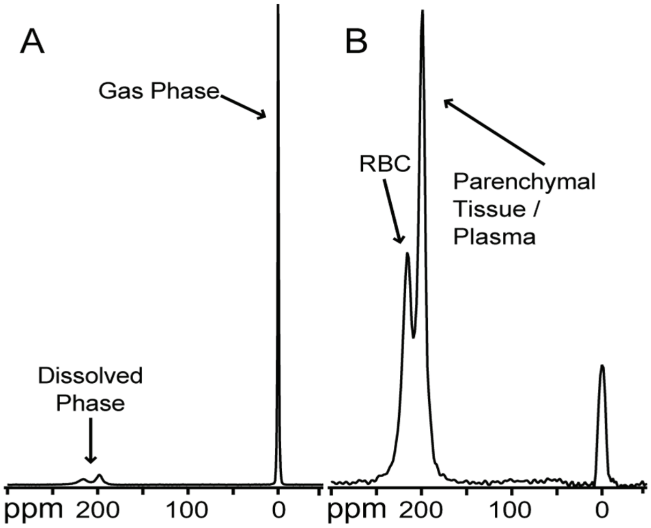

Figure 2.7: Xenon spectrum acquired after inhalation of HP ^{129}Xe from a human subject. (a) NMR spectrum obtained using a hard, 7° RF pulse. The gaseous HP ^{129}Xe signal is used as the 0ppm reference. (b) Spectrum from a selective, 7° pulse centered at 218ppm. Reproduced from [4].

2.4 Applications of HP ^{129}Xe

The major application of HP Xenon gas in the past 15 years has been the detection of lung ventilation function. An early project I worked on after joining the lab involved using HP ^{129}Xe MRI to detect pulmonary mucus plugs in animal models of cystic fibrosis (CF), a disease that plagues hundreds of thousands of individuals each year [80]. CF is characterized by the accumulation of mucus in the airways, which leads to the obstruction of airflow and chronic infection and inflammation in the lungs [81]. Currently, spirometry remains the gold standard for its diagnosis, despite its low sensitivity and non-specificity, which lead to poor correlation between lung function indicator (FEV_1) and symptoms, and to failure to detect the early onset and eventual exacerbation of CF [82, 83]. Chest computed tomography (CT) is the prevailing tool to assess efficacy of treatments due to its superior spatial and temporal resolution. However it exposes patients to high radiation doses, which is a concern for longitudinal studies in CF patients. Recently MRI has been used for lung imaging to visualize pulmonary structures [84] and to assess lung function [85]. However, MRI screening for CF remains challenging mainly due to the lack of water protons in the lungs, respiratory and cardiac motion and, more importantly, the highly heterogeneous structure of the lungs that causes severe field distortions that rapidly dephase the small amount of proton MR signal.

Several gaseous contrast agents have been proposed to better accommodate the need for pulmonary MR imaging, the most popular of which are ^{3}He [86–88], ^{19}F (in the form of inert fluorinated gas) [89–91] and ^{129}Xe [92–94]. The major obstacle to using gases in MRI is their five-order-of-magnitude-lower spin density in the gaseous state as compared to liquid water. The low spin density, coupled with lower gyromagnetic ratios of these nuclei, reduces the achievable SNR significantly. In ^{19}F gas MRI, thanks to its extremely short T_1 relaxation time [95], the magnetization can be repeatedly excited with a very short TR to enable the acquisition of whole lung images within a single breath-hold. The T_1 relaxation times of ^{3}He and ^{129}Xe, on the other hand, are much longer so their magnetization will have to be artificially enhanced through hyperpolarization as outlined in the previous section. By using HP ^{129}Xe, we developed a method that combined ultrashort echo time (UTE) proton images with gradient echo xenon images to locate mucus plugs inside the airways and to detect ventilation function defects that are produced by mucus obstruction [96]. Fig.2.8 shows images acquired in a CF mouse model. In HP ^{129}Xe gradient-echo images, regions with normal ventilation function appeared bright and homogenous in Fig.2.8(a), while in diseased regions where regional ventilation was impaired, the abnormal regions assumed a darker appearance, commonly referred to as “ventilation defects”. Concomitantly, proton UTE lung images in Fig.2.8(b) show the presence of several spots of increased brightness compared with the encompassing parenchyma in the same areas of decreased ventilation. These spots had a glassy appearance, were present only in one or two consecutive slices, and did not seem to be connected to other blood vessels or tissues. These spots were also found mainly in the main stem bronchi, and more in young than in older mice. The location of these spots correlated well with areas of mucus obstruction found histologically, which are highlighted by arrows in Fig.2.8(c). Compared to traditional ^{1}H MRI images, HP ^{129}Xe offers a higher SNR in the lungs. It also provides additional information about ventilation malfunctions, which, when combined with the ability of UTE images to detect mucus accumulations, demonstrated a clear advantage over CT.

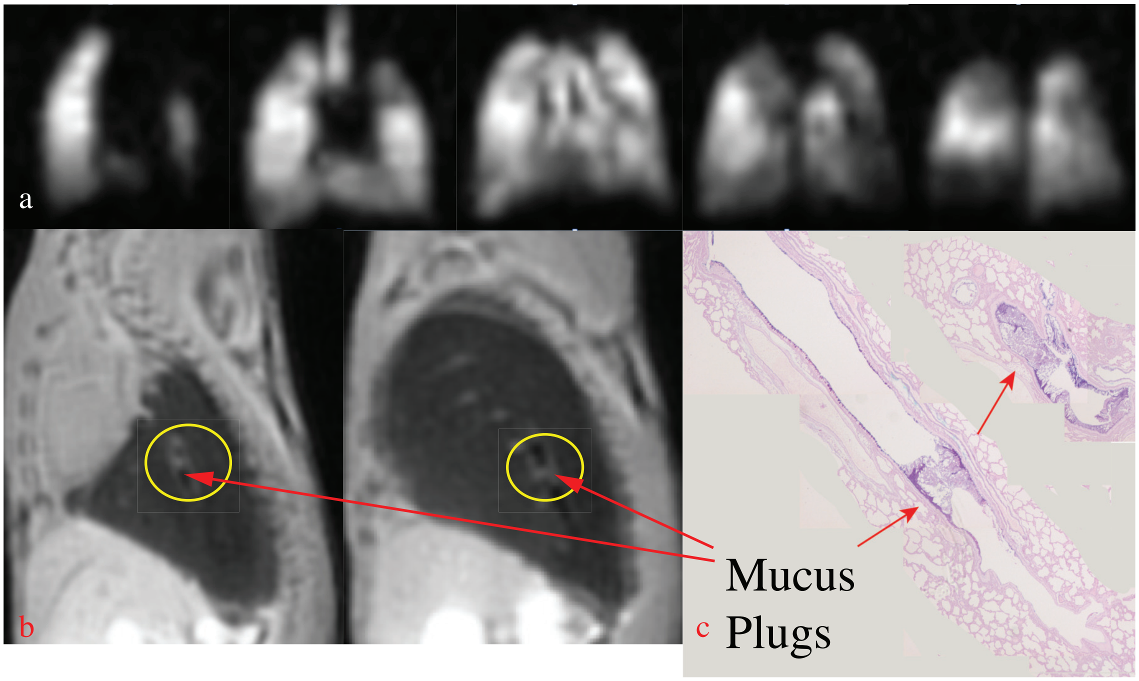

Figure 2.8: (a) Coronal HP ^{129}Xe GRE images of lungs showing various degree of airway obstructions due to mucus accumulation. (b) Sagittal slices of 3D UTE proton images with the yellow circles highlighting the possible sites of mucus in the airways. (c) Post-mortem histology results showing mucus.

Aside from ventilation imaging, which primarily shows ventilation defects as patchy or wedge-shaped regions of reduced signal in patients with lung diseases [97–101], the application of HP ^{129}Xe has expanded to other body regions thanks to the high solubility of the gas in blood and tissues and the wide range of chemical shifts displayed by the nucleus. Novel fast acquisition schemes, such as spiral or radial k-space filling [102] and k-space undersampling [103], have enabled dynamic ventilation imaging to help track gas-flow patterns temporally during an entire breathing cycle. More quantitative methods include measurement of the apparent diffusion coefficient (ADC) to quantify the size and connectivity of the airspace [104, 105]. Moreover, in MR spectroscopy, by saturating the dissolved peaks and observing its recovery, multiple parameters relating to the dynamics of gas perfusion and exchange can be measured [106, 107]. Beyond lungs, the dissolved phase of HP ^{129}Xe in red blood cells and lung tissues can be acquired to identify regions with impaired gas exchange [108, 109]. It has been observed that these parameters may change for certain lung diseases, such as lung cancer, that affect the overall pulmonary blood flow pattern and the resulting HP ^{129}Xe distribution [110]. Some of the features of the dissolved-phase peaks have been further suggested to correlate with the existence of some tumor types [111]. Despite the low concentration of HP ^{129}Xe in distant organs, direct imaging of the dissolved phase has been achieved, with dissolved xenon images having long been acquired in rat brains [112] and heart [71], and more recently in human lungs [4] and brown adipose tissues [113]. Advances have also been made in the realm of molecular imaging with HP ^{129}Xe, where the large range of chemical shift displayed by ^{129}Xe makes it an ideal probe for the investigation of biological systems. A major challenge is to design a carrier within which ^{129}Xe experiences both a long T_1 relaxation time [114] and a distinctively large chemical shift difference from its gaseous counterpart [115]. Cryptophane cages [116] have been widely used as a vehicle for ^{129}Xe atoms to study the binding event between the ligand and a wide range of target proteins, which registers as a change in xenon chemical shift. Studies have shown that this has the potential to detect cancerous cells [117]. HyperCEST techniques have also been demonstrated to improve the detection sensitivity [118].

In this thesis we will try to widen the range of HP ^{129}Xe applications to MR thermometry.

CHAPTER 3: EFFECTS OF MICROSCOPIC SUSCEPTIBILITY GRADIENTS ON PRF THERMOMETRY

Temperature, one of the most fundamental properties of matter, is also one of the most important parameters in the successful implementation of hypothermia [119], thermal ablation, [120], MR-guided high-intensity focused ultrasound (HIFU) [121] and MR-guided focused ultrasound (MRgFUS) [122]. For these treatments to succeed, the temperature of the heated region has to be measured both precisely in order to kill cancer cells while leaving healthy tissues undamaged. Yet temperature of tissues inside the human body is hard to measure non-invasively and non-destructively [123].

In the first half of this chapter, I will provide a brief introduction on temperature measurements by MRI and MRS. Specifically I will focus on the proton resonance frequency (PRF)-based MR thermometry method. In the second half I will analyze, by using both simulations and experiments, the effect of microscopic susceptibility gradients on the accuracy of PRF thermometry methods. The results presented in this chapter as well as in Chapter 5 and the first part of Chapter 6 have been published by our group in [124]. In this and the following chapters, the words lipid, methylene, adipose and fat will be used interchangeably to mean the strongest peak among the nine fat peaks observed in a typical proton NMR spectrum of adipose tissue.

3.1 MR Thermometry Methods

A variety of MR parameters are sensitive to temperature changes. Proton density, which changes with temperature according to Equation 2.1, does so at a virtually linear rate of -0.30±0.01%/°C between 37°and 80°C [125]. As a result, the relative temperature change can be calculated by using proton density (PD)-weighted images. However, this method requires extremely high SNR (~100) to achieve an accuracy of within 3°C and PD-weighted images also need long TR to avoid any T_1 weighting, which makes it less clinically appealing [126]. The spin-lattice (T_1) relaxation time, originating from dipolar interactions between water molecules and macromolecules via translational and rotational motions, also depends on temperature. This dependence can be modeled as $T_1(T) = T_1(T_{\mathrm{ref}}) + m \cdot (T - T_{\mathrm{ref}})$, where T_{ref} is the reference temperature, and $m = \frac{\mathrm{d}T_1}{\mathrm{d}T}$ can be determined empirically for each tissue type [127]. T_1 maps can be obtained by using fast T_1 imaging sequences [128, 129] to improve temporal resolution. The extraction of temperature information, on the other hand, can become difficult as the temperature coefficient of the individual tissues in the heated region may not be known *a priori* [130]. A similar increase in the spin-spin (T_2) relaxation time of proton spins with elevating temperature has also been known and used as a probe for temperature measurements, especially in adipose tissues [131, 132]. However, as T_2 time gets considerably reduced *in vivo*, any changes due to temperature can be easily masked by the impact on T_2 from other factors, such as field inhomogeneities and motion. Consequently this method is often non-linear and typically used only to observe any irreversible tissue damage during thermal ablation, which causes a sudden drop in T_2 [128]. The water diffusion constant D is another parameter that exhibits a temperature dependence. This dependence is about 2%/°C [133]. This high coefficient enables temperature measurement *in vivo* [134], though changes in tissue conditions such as protein coagulation during thermal ablation may compromise its linearity [135].

3.1.1 PRF-Based MR Thermometry

To date the most popular MR thermometry sensor is the proton resonance frequency (PRF) of water, whose temperature dependence was first observed in 1966 [136]. Such a dependency arises from the thermal deformation of hydrogen bonds in water molecules that dictates the degree of magnetic screening the proton nuclei receive from the electron cloud. Compared to a ^{1}H nucleus in a stand-alone water molecule, the same nucleus will have less electron screening if the water molecule is hydrogen bonded to another water molecule, due to the strong electronegativity of oxygen atoms which distorts and pulls the electron cloud away from the ^{1}H nucleus. The bonded state is thermally preferable at lower temperatures as two bounded water molecules have a lower collective energy. Consequently, the PRF will have a higher chemical shift because the proton nuclei are less shielded. As temperature rises, a higher percentage of water molecules will become unbounded as the hydrogen bonds get stretched, bent or even broken up [137]. This induces more current in the electron clouds of the ^{1}H nucleus, strengthening the shielding effect and, as a result, the PRF decreases. However, the real picture is much more complex than the simplified version provided above, as water is known to form not just dimers but trimers or even polymers of various sizes [138]. The hydrogen bonds also have multiple degree of freedoms in terms of angles and lengths, all of which can potentially change the screening factor [138]. Nonetheless, the temperature coefficient of PRF has been determined *in vivo* to be highly linear at -0.01ppm/°C. This temperature coefficient has also been found to be highly independent of tissue type, and relatively constant over a temperature range of more than 100°C [139].

Temperature imaging with PRF can be implemented using two approaches. The first is through phase mapping, where the phase difference between two images acquired pre- (at a reference temperature of T_0) and post-heating (at an unknown temperature of T) with identical echo time (TE) is used to calculate the temperature change according to Equation 3.1:

$$\Delta T = \frac{\phi(T) - \phi(T_0)}{2\pi\gamma\alpha B_0 TE}, \tag{3.1}$$

where γ=42.576MHz/T is the gyromagnetic ratio of proton, α=-0.01ppm/°C is the temperature coefficient of PRF, and B_0 is the strength of the the main field. The phase accumulation can be determined using a voxel-by-voxel phase unwrapping algorithm from the frequency $\nu(x, y)$ across the imaged region according to $\phi(x, y) = \mathrm{mod}\{e^{2\pi i\nu(x,y)TE}\}$.

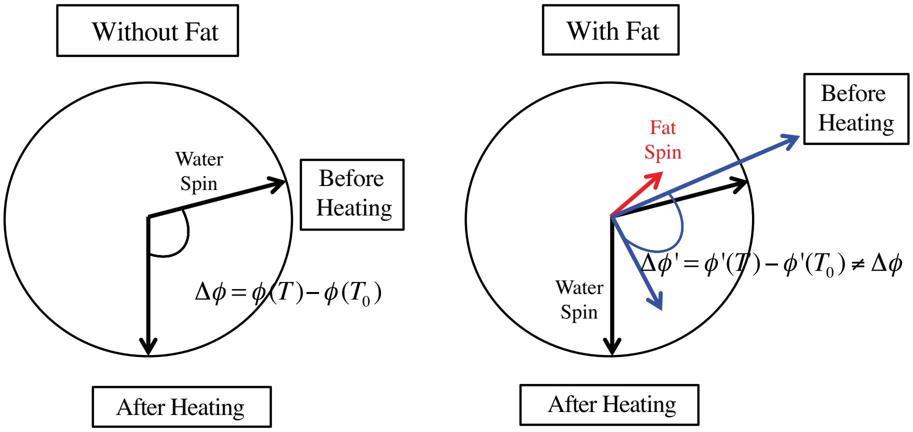

Figure 3.1: Illustration showing the impact of lipid spins to the change of the phase of net magnetization. The blue vector is a sum of the corresponding fat and water vectors.

Although a temperature image can be acquired with commonly used sequences such as gradient-echo (GRE) within a short amount of time, it is still susceptible to technical issues such as motion and field drift, which can easily mask the -0.01ppm/°C temperature coefficient. Motion has been shown to cause temperature errors up to 5°C even when acquisitions were triggered to the breathing cycle [140]. More importantly, since we can only detect the phase of the net magnetization, if the signal consists of two different spin components, such as water and fat, temperature measurements will become inaccurate. For instance, the presence of a temperature-independent fat peak will introduce a non-evolving vector to this sum, as illustrated in Fig.3.1. Fat-suppression method can help alleviate the problem [141], but in thermal therapies the accurate knowledge of the temperature of fatty tissues is often critical to avoiding skin burns.

Another issue with phase mapping method is the field perturbation generated by the spatial variation of the magnetic susceptibility ($\chi(\vec{r})$), which produces field perturbations:

$$\vec{B_d}(\vec{r}) = \frac{B_0}{4\pi}\frac{\partial^2}{\partial z^2}\int \frac{\chi(\vec{r})}{|\vec{r}-\vec{r}'|}\mathrm{d}^3\vec{r}'. \tag{3.2}$$

For example, the susceptibility difference between muscle and adipose tissue is on the order of 1ppm, and the resulting B_d can have a 100 times higher impact on PRF than temperature, making PRF methods unsuitable for absolute temperature measurement. In practice PRF is often used to measure relative temperature changes, where a heated phase image is compared to a baseline image acquired at a known temperature (normally 37°C). This unfortunately will be susceptible to inter-scan motion and, more importantly, will not satisfy the needs for absolute temperature-time history in calculation of the critical parameter of thermal dose during a thermal therapy session. Moreover, though the susceptibility of water spins is virtually temperature independent (+0.0026 ppm/°C [142]), that of fat spins does have a temperature coefficient (+0.00804 ppm/°C [143]) that is comparable to that of PRF. The implications are that even when PRF is used for relative temperature measurements, the shift in PRF caused by changes in magnetic susceptibilities still undermines its accuracy in the presence of fatty tissues (such as in breasts), even when they lie outside of the voxels of interest [144, 145]. Baron *et al*. [146] proposed a model-based correction method to address this issue [147], which estimates the changes in the susceptibility field induced by temperature to correct for its impact on the frequency of water. However, this approach requires accurate mapping of the susceptibility distribution and its temperature dependence, which cannot be known at a scale smaller than the MR spatial resolution. Recent advances have proposed several methods to possibly eliminate the need for a baseline image, including model-based referenceless method [148], multi-baseline correction methods [149], hybrid approach combining referenceless and multi-baseline correction methods [150], and phase gradient method [151]. These methods have been demonstrated to reduce the error to sub degree levels and/or be able to measure absolute temperature. However they all require heavy computational load for procedures such as phase unwrapping or regression fitting and cannot provide real-time thermometry information [152].

The second approach is spectroscopic temperature imaging, where the PRF frequency is calculated from an MR spectrum and compared to its counterpart at a known temperature to determine relative temperature change. One of the pitfalls of this approach is that, same as for the phase imaging method, any change in the local magnetic field caused by motion, field drift and macroscopic field inhomogeneities can easily overshadow the much smaller change in PRF caused by temperature. To correct for this type of error, a temperature-independent peak is often used as a reference. This temperature-independent reference is typically provided by either methylene protons in fat containing tissues [153, 154], or by NAA protons in the brain or the NAA peak in the case of temperature mapping in the brain [155]. Commonly used sequences for spectroscopic temperature imaging include single-voxel spectroscopy (SVS) [156], chemical shift imaging (CSI) [157], magnetic resonance spectroscopic imaging (MRSI) [158], echo planar spectroscopic imaging (EPSI) [159], line scan echo spectroscopic imaging (LSPESI) [160] and water saturation shift referencing [161]. Calculation of temperature from the resulting spectra is done on a voxel-by-voxel basis, where the water and the reference (*i.e.* fat) peaks are fit separately to a Gaussian or Voigt shape to determine their respective chemical shift. Alternatively, the free-induction decay (FID) can be fit in the time domain to determine the frequency. By using the difference between the chemical shifts of water and the reference peak as a temperature probe, the impact all the adverse factors mentioned above should be removed and the result should truly reflect temperature change. Indeed spectroscopic methods have been suggested as being able to measure absolute temperature [162]. The main drawback for spectroscopic imaging is the low temporal and spatial resolution. As a result they do not permit up-to-date measurement of temperature *in vivo*, which is critical in the management of thermal dose during thermal therapy. When applied to highly inhomogeneous regions (such as bone marrow) where peaks have broad linewidths and irregular shapes, accurate measurement of temperature can become prohibitively difficult [163, 164]. More crucially, since water and lipid spins always reside in different tissue or cell compartments, the effect of local susceptibility gradients shown in Equation 3.2 cannot be completely removed by using lipid spins as a reference. To make matters worse, the temperature-dependent magnetic susceptibility of fat can lead to significant temperature-induced changes in the local magnetic field distribution, further reducing the accuracy of PRF-based relative temperature measurements in the presence of fat.

In this chapter, we will study the effect of magnetic susceptibility gradients on the accuracy of PRF thermometry methods. First numerical simulations will be performed on samples with different distributions of fat and water spins to examine the shift in frequency induced by various distributions of water and fat spins within the imaged voxel. *In vitro* studies will then be carried out to measure the apparent temperature coefficient of PRF on various mixtures of fatty and muscle tissues excised from rats, mice and human cadavers. Finally the accuracy of PRF-based MR thermometry will be assessed *in vivo*.

3.2 Effect of Microscopic Susceptibility Gradients on PRF-based MR Thermometry: Numerical Simulations

As mentioned in the previous section, water and fat spins always reside in different tissue and cell compartments and, as such, the effect of microscopic susceptibility field cannot be removed by referencing the water resonance frequency to that of nearby fat. To this end, simulations were carried out to characterize the temperature-induced changes of the magnetic susceptibility field generated by different distribution patterns of water and fat spins and to evaluate their effect on the resonance frequency of water and fat spins and on the accuracy of relative and absolute PRF-based MR thermometry.

3.2.1 Mathematical Modeling of Microscopic Susceptibility Gradients

The field perturbation generated by a given distribution of magnetic susceptibilities was calculated as done in [146], which was in turn built on the method developed in two previous publications [5, 165], by taking advantage of the linear and local relation that exists in k-space between the z-components of the magnetization density, $M_z(\mathbf{k})$, and the susceptibility field, $B_z(\mathbf{k})$.

Briefly, when a sample is placed in a constant external field aligned along the z-axis, $H_0 = B_0/\mu_0$, the induced magnetization will be proportional to H_0 via:

$$\mathbf{M_0} = \chi \cdot \mathbf{H_0} \tag{3.3}$$

For tissues normally encountered *in vivo*, $\chi \ll 1$. It can be proven that the resulting spatial distribution of the induced magnetization will only have its z-term M_z deviating significantly from zero:

$$M_z(\mathbf{r}) = \chi(\mathbf{r})\frac{B_0}{\mu_0\mu_r(\mathbf{r})} = \chi(\mathbf{r})\frac{B_0}{\mu_0(1+\chi(\mathbf{r}))} \approx \chi(\mathbf{r})\frac{B_0}{\mu_0} \tag{3.4}$$

The susceptibility field generated because of the susceptibility mismatch between water and fat compartments can be calculated from:

$$\mathbf{B}_d(\mathbf{r}) = \frac{\mu_0}{4\pi}\int \frac{1}{|\mathbf{r}-\mathbf{r}'|^3} \times (3\frac{\mathbf{M}(\mathbf{r}')\cdot(\mathbf{r}-\mathbf{r}')}{|\mathbf{r}-\mathbf{r}'|^2}(\mathbf{r}-\mathbf{r}') - \mathbf{M}(\mathbf{r}'))\mathrm{d}^3\mathbf{r}', \tag{3.5}$$

with the relationship between vectors illustrated in Fig.3.2.

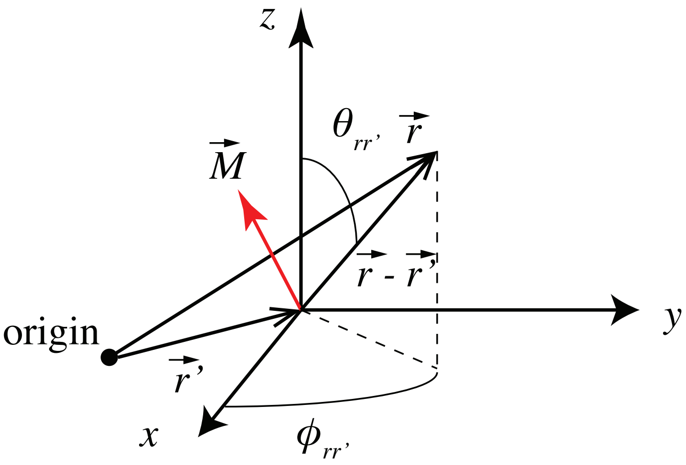

Figure 3.2: Cartoon illustrating the relation between the variables in Equation 3.5.

Equation 3.5 is nearly impossible to solve analytically in the real space as the relation between B_z and **r** is non local. However, this relation localizes in the Fourier space [166]:

$$\tilde{\mathbf{B}}_d(\mathbf{k}) = \frac{\mu_0}{3}\frac{3\cos^2\beta - 1}{2}(\tilde{\mathbf{M}}(\mathbf{k}) - 3\tilde{M}_z(\mathbf{k})\tilde{\mathbf{z}}) \tag{3.6}$$

where $\mathbf{k}$ is the Fourier conjugate variable of $\mathbf{r}$, $\tilde{M(\mathbf{k})}$ and $\tilde{M_z}(\mathbf{k})$ are the 3D Fourier transforms of $\mathbf{M}(\mathbf{r})$ and $M_z(\mathbf{r})$, respectively. β is the angle between the vector $\mathbf{k}$ and direction of the main magnetic field $\mathbf{B}_0$:

$$3\cos^2\beta - 1 = 3\frac{k_z^2}{k_x^2 + k_y^2 + k_z^2} - 1 \tag{3.7}$$

The more detailed derivation of Equation (3.5) can be found in [5] and will not be repeated in this dissertation. It is concluded that in the rotating frame of reference the transverse term of $\tilde{M}(\mathbf{k})$ in Equation 3.6 is of no relevance while only the longitudinal term has a non-negligible contribution to the dipolar field. As a result, it reduces to:

$$\tilde{B_{dz}}(\mathbf{k}) = \tilde{\mathbf{B}_d} \cdot \tilde{z} = M_z(\mathbf{k}) \cdot \frac{\mu_0}{3} \cdot (1 - 3\cos^2\beta) \tag{3.8}$$

where μ_0=1.2566T$\cdot \mu m \cdot A^{-1}$.

Plugging Equation 3.4 into the above equation leads to:

$$\tilde{B_{dz}}(\mathbf{k}) = -\frac{\chi(\mathbf{k})B_0}{3} \cdot (1 - 3\cos^2\beta). \tag{3.9}$$

Finally, the inverse Fourier transformation of $\tilde{B_{dz}}$ will yield $B_z(\mathbf{r})$ generated by the spatial distribution of magnetic susceptibility $\chi(\mathbf{r})$.

3.2.2 Numerical Simulations

3.2.2.1 Method Validation

To test our MATLAB program that implemented the above calculation, several benchmark simulations were carried out and their results were compared with those reported in [5] using the same method. Specifically, two geometries were tested. The first one was a sphere with a radius of 12 pixels inside a matrix of 256^3 pixels. The second was an infinitely long cylinder with a radius of 12 pixels, which had its long axis aligned with the z-axis, inside a similar matrix. For both geometries, the internal volume magnetic susceptibility was set to χ_i=-0.72*ppm* and the external volume magnetic susceptibility was set to χ_e=-0.36*ppm*.

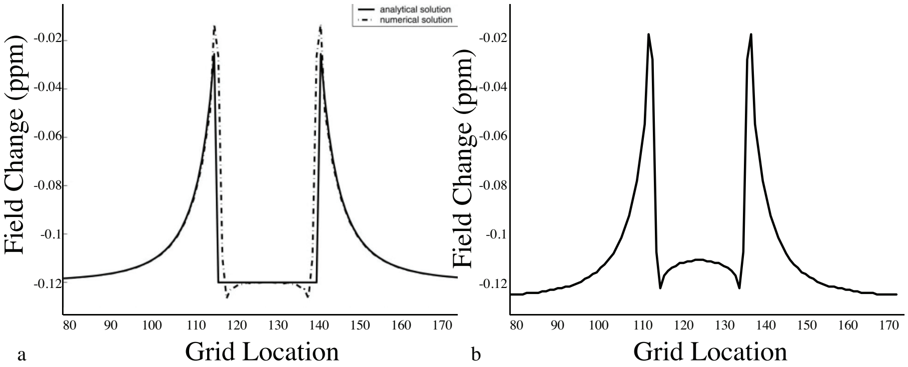

Figure 3.3: Comparison between the numerical simulation results presented in [5] (dashed line in (a)) and our results (b) for a straight line crossing the center of the spherical geometry along the y-direction.

Our simulation results and those presented in the paper are compared in Fig.3.3 for the sphere structure and in Fig.3.4 for the cylinder structure. The figures show the z-components of the field disturbance due to the susceptibility mismatch along a line that was parallel to the y-axis passing through the center of both structures. Good agreement is observed between these two methods.

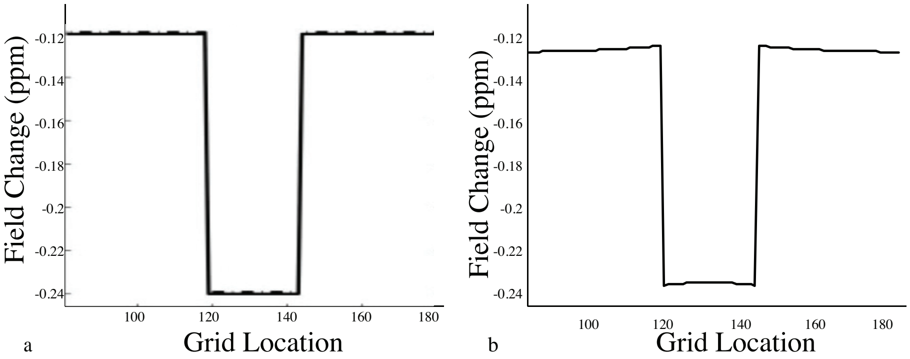

Figure 3.4: Comparison between the numerical simulation results presented in [5] (dashed line in (a)) and our results (b) for the cylindrical geometry.

3.2.2.2 Simulated Geometries

Simulations were then performed on geometries that better resembled the water/fat distribution found in biological system. These geometries are shown in Fig.3.5. All simulated geometries consisted of a

128×128×128 matrix, with an isotropic resolution of 2.056μm/px. The total volume for each geometry was 0.018mm^3, much smaller than the typical voxel size used in MRI. The blue color represented the part of the matrix designated as the water compartment, which was assigned a volume magnetic susceptibility of -9.04ppm [142], while the yellow color represented the part of the matrix designated as the fat compartment, which was assigned a volume magnetic susceptibility of -7.79ppm [167].

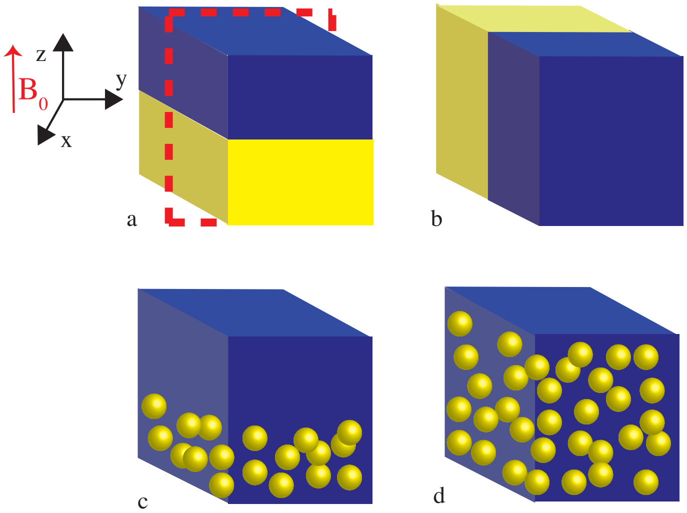

Figure 3.5: Water-fat distribution patterns simulated in this study. The yellow color represents the fat compartment while the blue color represents the water compartment.

A total of 25,000 proton spins were distributed evenly inside the 3D matrix. Simulations were run at two different temperatures. Specifically, the susceptibility ratio of fat spins was changed from -7.79ppm, assumed for a reference temperature of 0°C, to -7.83ppm, 5°C above the reference according to the temperature dependence of $\mathrm{d}\chi_f/\mathrm{d}T$ reported in porcine fat [143]. Simulations were performed assuming an external magnetic field B_0 of 1T aligned along the z-axis (giving a proton Larmor frequency of 42.58MHz). The computed $B_{dz}(\mathbf{r})$ using the steps outlined in the previous section was then superimposed onto the main field to calculate the evolution and apparent frequency shift of water and fat spins diffusing and dephasing in their respective compartments. Specifically, the evolution of the two types of spins was recorded every 0.167ms

before they were allowed to diffuse onto a different position, for a total simulation time of 2s. Diffusion was computed using a random walk Monte Carlo algorithm, with a diffusion length L of 1.5μm calculated from

$$L = \sqrt{6 \cdot D \cdot \tau}, \tag{3.10}$$

with the diffusion coefficient of water in tissues being $2.22 \times 10^{-3} mm^2 \cdot s^{-1}$ [168] and the time step τ=0.167ms as mentioned above. A Fourier transform of the simulated FID was then performed to obtain a spectrum from which water and fat frequency shifts were determined.

3.2.2.3 Simulation Results

Fig.3.6 shows the local magnetic field disturbance induced by the susceptibility mismatch in the four geometries shown in Fig.3.5, while Table 2.1 summarizes the changes in the chemical shift of water and fat spins caused by the susceptibility field. The absolute temperature measurement error in the sixth row was calculated by comparing the chemical shift difference between the water and fat spins shown in the fifth row from every geometry at either temperature against a reference of 0ppm, and dividing the result by the temperature coefficient of PRF of -0.01ppm/°C. The results showed that the magnetic susceptibility difference between water and fat compartments can change the water resonance frequency by as much as 0.2ppm. More importantly, because water and fat spins reside in different tissue compartments, their frequencies are generally shifted in opposite directions and by different amounts. As a result, they will yield absolute temperature measurements that can be off by several tens of degrees Celsius. In addition, because of the strong temperature dependence of the magnetic susceptibility of fat, as temperature changes, the water and fat resonance frequencies will not only be shifted by temperature, but also by the temperature-induced changes in the susceptibility field distribution. This causes the use of fat spins as a reference for the water resonance frequency even less reliable than just using the chemical shift of water spins to calculate relative temperature changes. This is evident when the results in the last two rows are compared, which shows that the fat-referenced PRF temperature measurement increased the error by as much as 11.4°C for the geometry in (d).

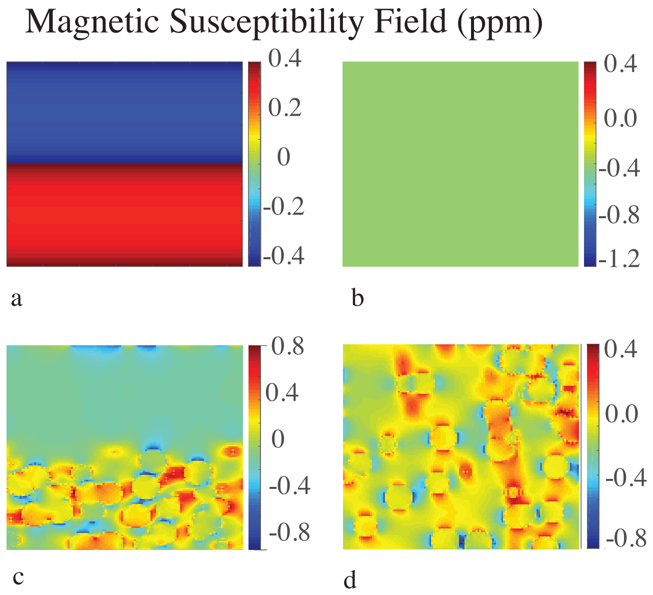

Figure 3.6: The susceptibility field maps reported for the center YZ slice (dotted square in Fig.3.5(a)), which are produced by the magnetic susceptibility mismatch between water and fat compartments.

Geometry	A		B		C		D	
Temperature (°C)	0	5	0	5	0	5	0	5
$\Delta\omega_{water}$ (ppm)	-0.04	-0.04	0.082	0.089	0.209	0.216	0.125	0.127
$\Delta\omega_{fat}$ (ppm)	0.163	0.066	0.016	0.012	0.082	0.085	0.056	-0.058
$\Delta\omega_{water} - \Delta\omega_{fat}$ (ppm)	-0.103	-0.106	0.066	0.077	0.127	0.131	0.069	0.185
Abs temp error using $\omega_{water} - \omega_{fat}$ (°C)	10.3	10.6	-6.6	-7.7	-12.7	-13.1	-6.9	-18.5
Rel temp error using $\Delta(\omega_{water} - \omega_{fat})$ (°C)	4.7		6.1		5.4		16.6	
Rel temp error using ω_{water} (°C)	0		5.7		5.7		5.2	

Table 3.1: Computed resonance frequency shifts of water and fat spins caused by magnetic susceptibility field for different water-fat distributions at two different temperatures. The table also shows the temperature error made when the water-fat resonance frequency difference is used to calculate absolute temperature (abs temp) and relative temperature (rel temp) changes.

3.3 Effect of Microscopic Susceptibility Gradients on PRF-based MR Thermometry: Experimental Work

In this section I will show *in vitro* and *in vivo* experimental results to assess the effect of microscopic susceptibility gradients on the accuracy of PRF-based MR thermometry methods.

3.3.1 *In Vitro* NMR Methods

Muscle and white adipose tissue (WAT) were excised from the legs and abdomen of mice and rats right after euthanasia, while human WAT was harvested from the subcutaneous adipose layer of human cadavers. Tissues were not homogenized but minced and placed into a 5mm O.D. medium-walled NMR tubes to create 3 different samples, one containing human WAT (hWAT), one containing rodent WAT (rWAT) and one containing a mixture of rWAT and muscle (rWAT/Muscle), which were then placed inside the magnet. Samples were scanned under different xenon pressures above the tissue in order to acquire xenon spectra, shown in Chapter 5, from these same samples. All spectroscopic studies were conducted on a Varian Inova 500MHz NMR Spectrometer (Varian NMR Systems of Palo Alto, California) with a ^{1}H-^{19}F/^{15}N-^{31}P PFG switchable broadband probe. First and second order shim gradients were used to clearly resolve the water and CH_2 (fat) peaks in the ^{1}H spectrum. A temperature controller (L900, Highland Technology, San Francisco, CA) was used to set and maintain sample temperature at a given value. Temperature was calibrated with an accuracy of 0.1°C at the beginning of each spectroscopy experiment by using the chemical shift separation between the methyl and hydroxyl peaks in a 100%-purity methanol sample. A 90°-acquisition sequence was used to acquire proton spectra at each temperature.

3.3.2 *In Vitro* NMR Results

Fig.3.7 shows representative ^{1}H spectra acquired on the rWAT sample on the high-resolution NMR spectrometer, as well as the temperature-induced shift on the water and methylene resonance frequencies. Water and methylene peaks are highlighted by the blue and red dashed boxes respectively. The ^{1}H center frequency was arbitrarily set such that the methylene peak appeared around -3.1ppm and the water peak appeared around 0.4ppm at 26°C. A small shift toward higher frequencies (+0.0032ppm/°C) was observed in the methylene resonance frequency (b), while water drifted toward lower frequencies with a larger temperature coefficient of -0.0089ppm (c). The linewidth of water peak was slightly higher (140Hz) than in other samples scanned, but still well separated from the nearby methylene peaks (~1700Hz downfield) such that we could determine the water resonance frequency with an accuracy of about 0.04ppm.

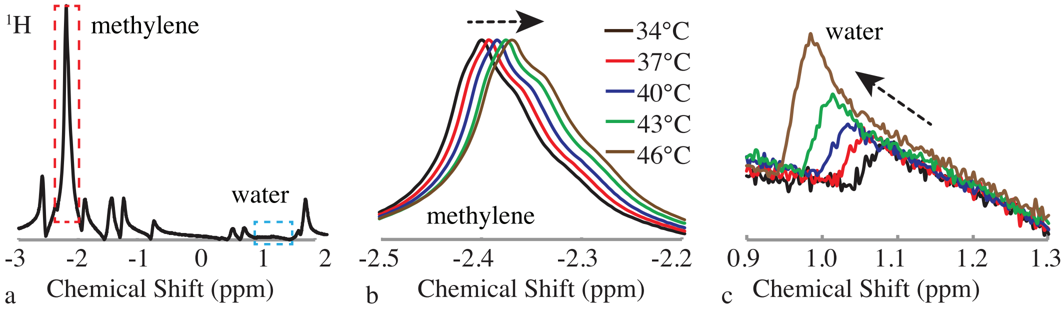

Figure 3.7: ^{1}H spectra acquired on the rWAT sample. (a) ^{1}H spectrum at 34°C. (b) Shift of the methylene resonance frequency line with temperature. (c) Shift of the water resonance frequency line with temperature.

Fig.3.8 shows the temperature dependence of the water and methylene resonance frequencies for rWAT, rWAT/Muscle and hWAT samples. When temperature was increased, the methylene frequency (a) increased slightly at a rate of about +0.003ppm/°C in the rWAT and hWAT samples. In these samples, the water resonance frequency showed a temperature dependence similar to the predicted -0.01ppm/°C. As a result, when the water resonance frequency was referenced to the methylene resonance frequency (c), the temperature coefficient of water increased for both samples (-0.011ppm/°C in rWAT and -0.013ppm/°C in hWAT). For the rWAT/muscle sample, on the other hand, the behavior was quite different. In this sample, the temperature dependence of the magnetic susceptibility of the fatty tissue caused a variation of the local field distribution, which affected both water and methylene frequencies. Specifically, the methylene resonance frequency decreased instead of increasing with temperature, while the water resonance frequency showed a much smaller temperature dependence of -0.0064ppm/°C in (b). In this sample, the distribution of water and fat spins drastically changed between the first set of measurements under 1 atm of xenon gas and the second set of measurements under 3 atm of xenon gas, probably due to a redistribution of water and fat compartments in the sample.

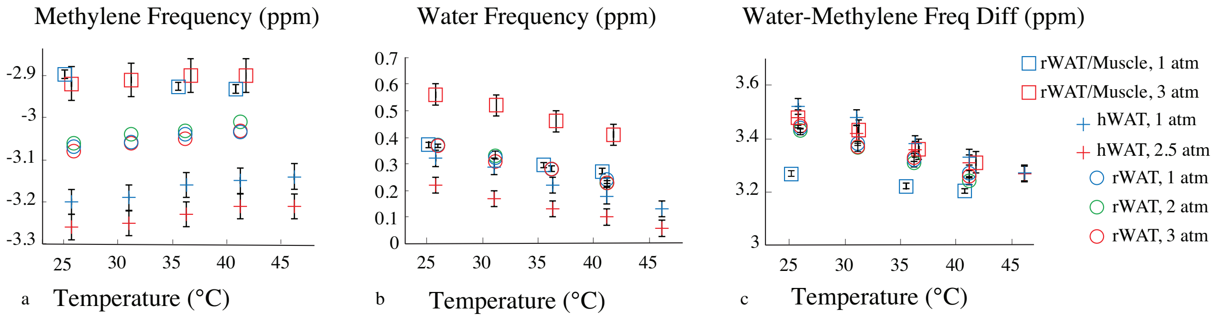

Figure 3.8: Temperature dependence of water and methylene resonance frequencies for five different adipose tissue samples under different xenon gas pressures. (a) Temperature dependence of the methylene resonance frequency. (b) Temperature dependence of the water resonance frequency. (c) Temperature dependence of the water-methylene resonance frequency difference.

It is worth mentioning that, in all samples, after the first set of measurements we observed a liquid phase floating on top of a more solid-like phase. Most likely, the breakdown of the adipocyte membranes led to the release of the lipid content of the cells. This separation did not affect the resonance frequencies of the water and methylene spins in the two fat samples (hWAT and rWAT), but drastically affected that in the rWAT/Muscle sample. In this case, the redistribution of the two compartments pushed water and fat frequencies in different directions, substantially changing the water-methylene resonance frequency difference by 0.37ppm, and its temperature dependence from -0.0105ppm/°C (measurement at 3atm) to -0.0041ppm/°C (measurement at 1atm). As predicted by our simulations, because water and fat spins reside in different tissue compartments, such redistribution led to a drastic change in the PRF results.

3.3.3 *In Vivo* MRI Methods

All *in vivo* studies were perfomed on 8 female obese (**ob/ob**) on a 9.4T Bruker BioSpec 94/30 USR (Bruker BioSpin, Billerica, MA) small animal scanner controlled by a console running ParaVision software.

Mice were placed either supine (2 mice) or prone (6 mice) inside a ^{1}H volume coil (72-mm inner diameter, transmit and receive, resonant at 400MHz). ^{1}H frequency maps were collected using a chemical shift imaging (CSI) protocol and analyzed pixel-by-pixel to determine the chemical shift of both water and fat protons. For these experiments the body temperature of anesthetized mice, who were unable to regulate their body temperature under anesthesia, was allowed to equilibrate with bore temperature of the scanner for at least 30 minutes before each measurement. Rectal and bore temperatures were monitored and maintained to within 0.2°C from the target temperature.

3.3.4 *In Vivo* MRI Results

Fig.3.9 shows the temperature maps acquired with PRF method in one of the mice imaged whose body temperature was equilibrated at three different temperatures at 29.4°C, 31.2°C and 33.2°C, using the resonance frequency of the methylene peak as an internal reference. The pink box in Fig.3.9(a) in the coronal mouse image shows the position and thickness of the axial slice across the abdominal region from where spectra and CSI images were acquired. A typical CSI spectrum from one of the voxels is shown in Fig.3.9(b), where the field inhomogeneity had clearly a huge impact on the line shapes of both water and fat peaks. The methylene frequency in this mouse exhibited a variation of as high as 0.3ppm across the FOV, mainly due to its irregular line shape. Double or even triple methylene peaks were also seen in several pixels, suggesting that fat spins resided in different magnetic environments. Figs.3.9(c∼e) show the temperature variation across the FOV at three temperatures calculated from fat-referenced water resonance frequencies from pixels where the fitting of both water and fat peaks yielded an error of less than 10%. In these maps the chemical shift difference between water and fat peaks $\Delta\omega^{ref} = \omega_W^{ref} - \omega_F^{ref}$ in one of the voxels was chosen as a reference and the temperature of other voxels was determined from their $\Delta\omega = \omega_W - \omega_F$ by $T_{rel} = (\Delta\omega - \Delta\omega^{ref})/(-0.01)$. A high temperature inhomogeneity is evident in these maps, which ranged from 8°C at 31.2°C to 35°C at 29.4°C. Figs.3.9(f∼h) show the relative temperature change maps between any two of the three temperatures by using fat-referenced PRF method. The results are similarly unreliable. While the actual temperature change was ~2°C in both of the first two figures, several pixels in Fig.3.9(f) suggested a temperature increase of higher than 30°C, while Fig.3.9(g) measured almost no temperature change. Fig.3.9(g) also severely overestimated the temperature increase than the actual 4°C measured by the rectal probe.

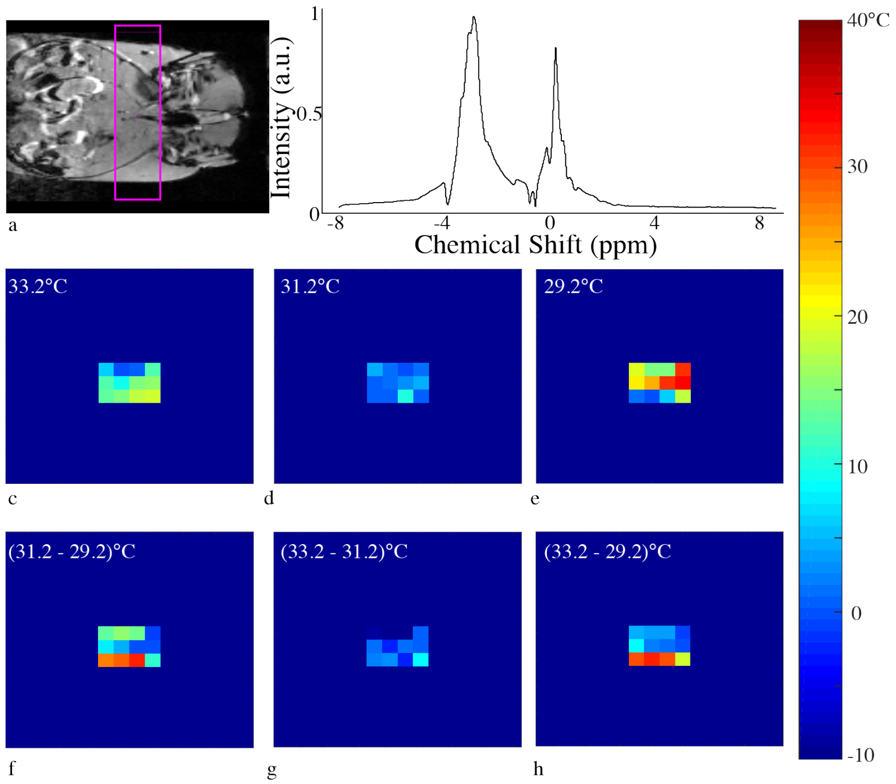

Figure 3.9: Frequency and temperature maps acquired *in vivo* from an obese mouse. (a) Anatomical image showing the slice selection. (b) Representative CSI spectral from a voxel in the abdomen. (c~e) Relative temperature maps calculated from fat-referenced PRF frequency. (f~h) Relative temperature change maps calculated from fat-referenced PRF frequency.

Fig.3.10 shows temperature maps for another mouse whose body temperature was equilibrated at two different temperatures at 31.2°C and 34.2°C, again by using the methylene frequency as an internal reference. The frequency maps of water spins across the mouse abdomen presented a resonance frequency variation of

~0.05ppm, which corresponded to a temperature variation of 5°C. The methylene frequency variation in this case was much larger at ~0.35ppm. Because of these large variations in the methylene resonance frequency, the fat-referenced PRF temperature maps displayed a variation of 40°C for both temperatures. Some pixels show an apparent temperature increase of 15°C, even though the actual temperature increase was only 3°C.

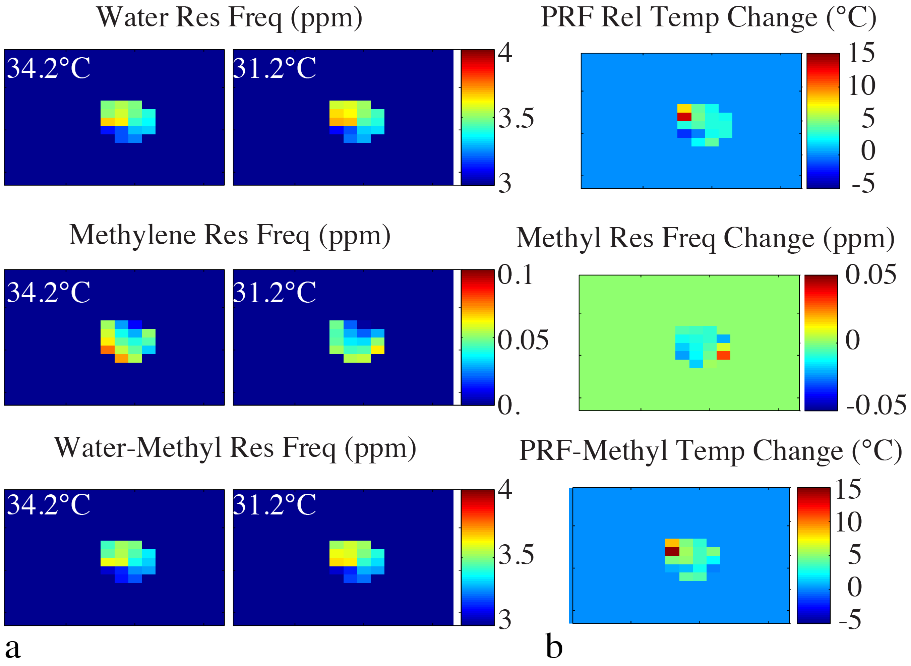
Water Res Freq (ppm)
34.2°C
31.2°C
4
3.5
3
PRF Rel Temp Change (°C)
15
10
5
0
-5
Methylene Res Freq (ppm)
34.2°C
31.2°C
0.1
0.05
0.
Methyl Res Freq Change (ppm)
0.05
0
-0.05
Water-Methyl Res Freq (ppm)
34.2°C
31.2°C
4
3.5
3
PRF-Methyl Temp Change (°C)
15
10
5
0
-5
a
b

Figure 3.10: Frequency and temperature maps acquired *in vivo* from another obese mouse. (a) Water, methylene and water-methylene resonance frequency maps. (b) Temperature maps showing the relative temperature change between the two measurements.

3.4 Discussion

The aim of this work was to assess how magnetic susceptibility gradients affect the accuracy of the PRF thermometry methods at the microscopic level. Specifically, the chemical shift temperature dependence of water and fat spins was measured *in vitro* for 3 different types of samples containing adipose tissue. Despite the strong similarity in composition between these samples, we observed a large variation in the chemical shift and in the temperature coefficient of the PRF, which means that, in the presence of fat, the use of the nominal -0.01ppm/°C PRF temperature coefficient can lead to very inaccurate relative and absolute temperature measurements. Computer simulations, which analyzed the effect of these microscopic susceptibility gradients on water and fat resonance frequencies, also confirmed that the relative distributions of water and fat at the microscopic level could undermine the accuracy of PRF-based MR thermometry. Specifically, the water-fat resonance frequency difference strongly depends on the microscopic distribution of water and fat spins such that absolute temperature measurements cannot be made.

In the rWAT and hWAT samples, we measured a slightly lower temperature coefficient for PRF than the -0.01ppm/°C nominally used for PRF thermometry. It then became slightly higher than -0.01ppm/°C when the fat frequency was used as reference. However, in the rWAT/muscle mixture we measured a significantly lower PRF temperature coefficient than that nominal value. In this case, the use of fat spins as reference led to a completely different temperature coefficient of -0.006ppm/°C. Such a difference could lead to a more than 45% temperature inaccuracy if a coefficient of -0.01ppm/°C were to be used. For example, for a temperature change of 5°C, a typical value for thermal therapy in clinical settings, the error that one would commit would be more than 2°C. As a result, relative temperature measurements *in vivo*, in the presence of fat, proved to be also very inaccurate.

Computer simulations showed that temperature-induced changes in the magnetic susceptibility of fat pushed water and fat frequencies sometimes in opposite directions, thus increasing their difference by as much as 0.02ppm over a temperature range of 5°C, and sometimes in the same direction, thus decreasing their difference by as much as 0.01ppm over the same temperature range. For example, in one of the geometries, for an increase of only 5°C, temperature would be overestimated by more than 2°C. However, when the same geometry is rotated by 90° with respect to B_0, temperature would be underestimated by more than 1°C. In short, water diffusion cannot average out the effect of susceptibility gradients at the microscopic level (i.e. within the imaged voxel), at which point these gradients become as important as the macroscopic susceptibility gradients studied by Baron *et al.* [146, 169].

Moreover, the magnitude of the water-fat chemical shift difference is also strongly affected by the relative distribution of water and fat spins at the microscopic level and therefore lipid protons cannot be used as a reference for water protons to obtain absolute temperature information. This is because the two spins do not mix but rather reside in different compartments and, unless the exact distribution of water and fat spins is known at the sub-voxel level, the accuracy of relative PRF-based temperature measurements is basically guaranteed only for voxels with a low fat content.

3.5 Conclusions

In conclusion, magnetic susceptibility gradients that exist at water fat interfaces have been shown to degrade the accuracy of PRF thermometry methods. Although the use of fat protons as temperature insensitive internal reference can help removing the effect of macroscopic field in homogeneities, field drift and motion, it cannot be used to remove the effect of microscopic susceptibility gradients that is not average out by diffusion at the microscopic level.

CHAPTER 4: EFFECTS OF MICROSCOPIC SUSCEPTIBILITY GRADIENTS ON WATER-FAT IZQC THERMOMETRY

In Chapter 3 we showed that microscopic susceptibility gradients undermine the accuracy of PRF based MR thermometry. In order to remove magnetic field inhomogeneities at a scale much smaller than the resolution achievable with common MRI techniques, people sought to use the signal generated from intermolecular multiple-quantum coherences (iMQCs) [170]. The removal of macroscopic field inhomogeneities via iMQCs is typically accomplished by the selection of a specific order of coherences, the intermolecular zero quantum coherences (iZQCs). Since the resonance frequency of water-fat iZQC reflects of the water-fat frequency separation at the microscopic scale, these frequencies have been proposed and used as a mean of obtaining more accurate temperature information, with some studies even suggesting the possibility of absolute thermometry.

The purpose of this work was to investigate how microscopic susceptibility gradients affect the water-fat iZQC resonance frequency. Specifically, we will first describe how iZQC signals are generated. We will then provide a theoretical description of how distant dipolar field interactions can lead to the observation of iZQCs. Finally, we will characterize the dependence of the water-fat iZQC resonance frequency on sample microstructure and on the specific choice of the correlation distance in the sequence. The results presented in this chapter and in part of Chapter 7 have been published by our group in [171].

4.1 Distance Dipolar Field and Its Applications in Magnetic Resonance

Thus far we have only considered one perturbation to a homogeneously applied magnetic field B_0: that generated by bulk susceptibility mismatch between different types of tissues. As I have explained in Chapter

2, each spin can be thought of as a tiny bar magnet that produces a small dipolar field that will affect all of its neighboring spins. The quantum treatment of this field, as well as how this field gives rise to iZQCs, will be provided in this section.

4.1.1 Density Matrix of an Ensemble

In order to understand the origin of iZQCs, we use a quantum description of NMR. Instead of following the classical evolution of the bulk magnetization vector using the Bloch equation, as done in Chapter 2, we will use the density matrix to describe the evolution of a spin system during an NMR experiment. The density matrix of an ensemble of N identical spins at thermal equilibrium is given by [172]:

$$\rho_{eq} = \frac{e^{-H_z/kT}}{Tr\{e^{-H_z/kT}\}}, \tag{4.1}$$

where H_z is the Zeeman Hamiltonian, formally defined as:

$$H_z = \sum_{i=1}^{N} \hbar\omega_0 I_{zi}, \tag{4.2}$$

where ω_0 is the Larmor frequency of the spins and I_{zi} is the operator for the z-component of spin i [173] (similar operators I_x and I_y represent the x- and y-component, respectively). Equation 4.1 is difficult to calculate directly. However, at room temperature, the term $\frac{\hbar\omega_0}{kT} \approx 10^{-4}$. As a result the density matrix at thermal equilibrium in Equation 4.1 can be expanded as a sum of hyperbolic functions:

$$\begin{aligned}\rho_{eq} =& \frac{\exp[\sum_i(-\frac{\hbar\omega_0}{kT})I_{zi}]}{Tr\{\exp(\sum_{i=1}^N(-\frac{\hbar\omega_0}{kT})I_{zi})\}} = \frac{\prod_{i=1}^N \exp(-\frac{\hbar\omega_0}{kT})I_{zi}}{Tr\{\prod_{i=1}^N \exp(-\frac{\hbar\omega_0}{kT}I_{zi})\}} \\ =& \frac{\prod_{i=1}^N\{\cosh(-\frac{\hbar\omega_0}{kT})\overline{E} - 2\sinh(-\frac{\hbar\omega_0}{kT})I_{zi}\}}{Tr\{\prod_{i=1}^N\{\cosh(-\frac{\hbar\omega_0}{kT})\overline{E} - 2\sinh(-\frac{\hbar\omega_0}{kT})I_{zi}\}\}} \\ =& 2^{-N}\prod_{i=1}^{N}[\overline{E} - 2\tanh(-\frac{\hbar\omega_0}{kT})I_{zi}].\end{aligned} \tag{4.3}$$

At room temperatures, $\tanh(\frac{\hbar\omega_0}{kT}) \approx \frac{\hbar\omega_0}{kT}$, and Equation 4.3 can be simplified as:

$$\rho_{eq} = 2^{-N}\{\overline{E} + (-\frac{\hbar\omega_0}{2kT})\sum_{i=1}^{N} I_{zi} + (-\frac{\hbar\omega_0}{2kT})^2 \sum_{i,j=1}^{N} I_{zi}I_{zj} + (-\frac{\hbar\omega_0}{kT})^3 \sum_{i,j,k=1}^{N} I_{zi}I_{zj}I_{zk} + \ldots\}. \tag{4.4}$$

4.1.2 How to Observe Multiple Quantum Coherences

In Equation 4.4, the first order terms I_{zi} are the ones that give rise to the conventional MR signal. These terms can be transformed into observable magnetization, I_{xi} or I_{yi}, by an RF pulse. The second order terms, $I_{zi}I_{zj}$, are the ones that give rise to iMQC. These terms are indeed transformed by an RF pulse into $I_{xi}I_{xj}$, $I_{yi}I_{yj}$, *etc.*, which are combinations of zero and double quantum coherences. However, under the "high temperature approximation", these higher-order terms are typically ignored because $\frac{\hbar\omega_0}{kT} \approx 10^{-4}$, greatly simplifying the density matrix calculation.

However, even though the contribution of these higher order terms is small, their collective effect could still be significant. The reason is that a typical sample contains N=10^{20} spins, and the total number of i-quantum coherence terms in Equation 4.4 is i^N. When these higher order terms cannot be ignored, a "spectacular breakdown of the high temperature approximation" occurs, leading to the observation of signals that would be impossible to observe if we were to retain only the single-operator terms in Equation 4.4. This is the case when the CRAZED sequence is used to acquire the signal from a sample of water [174]. It is clear that, in this sequence, the single-operator terms are completely dephased and cannot give rise to an observable signal. Yet, a relatively strong signal can still be observed when this sequence is applied to a spin system in solution.

However, in order to observe the signal originating from these higher-order terms, two conditions need to be satisfied. The first is that the second order terms have to be transformed into two-spin single-quantum operators, such as $I_{zi}I_{xj}$. This can be easily accomplished by an RF pulse. However, since $I_{zi}I_{xj}$ represents anti-phase magnetization, a two-spin interaction with spin operators of the form $I_{zi}I_{zj}$ must also exist to transform the anti-phase $I_{zi}I_{xj}$ into observable in-phase magnetization. In the CRAZED sequence, this comes from the long-range dipolar field interactions.

4.1.3 Distant Dipolar Field Interactions

The Hamiltonian governing the interactions between a pair of spins, or magnetic dipoles, I_i and I_j that are separated by a distance of r_{ij} is:

$$H_d = \hbar D_{ij}(3I_{zi}I_{zj} - \vec{I_i}\vec{I_j}), \tag{4.5}$$

where D_{ij} denotes the nuclear-nuclear dipolar coupling constant and has a unit of rad/s. It is defined as:

$$D_{ij} = -\frac{\mu_0}{4\pi}\frac{\gamma^2\hbar}{4}(\frac{3\cos^2\theta_{ij} - 1}{r_{ij}^3}), \tag{4.6}$$

with θ_{ij} being the angle between the internuclear vector and the main magnetic field B_0. The sign of D_{ij} depends on the relative orientation of the magnetic moments of the two spins.

Under the dipolar field interaction, the evolution of the anti-phase magnetization, for example, $\rho_{eq} = I_{zi}I_{yj}$ after an RF pulse can be calculated through the use of commutation of spin operators:

$$\frac{\partial\rho}{\partial t} = -i[H_d, \rho_{eq}] = -i[D_{ij}I_{zi}I_{zj}, I_{zi}I_{yj}] = \frac{D_{ij}}{4}I_{xj}, \tag{4.7}$$

which means that the anti-phase magnetization originating from higher-order terms in the density matrix shown in Equation 4.4 can be converted to an observable single-operator term after M-1 commutations with the dipolar field Hamiltonian. These commutations need long time to take place, and this process also competes with the relaxation of the transverse magnetization. As a result, typically only two spin operator terms in Equation 4.4 are retained when analyzing iMQC sequences, since they are the ones that are most likely to be refocused by dipolar field before relaxing back to the z-axis.

Equation 4.7 also demonstrates that the intensity of the iMQC signals is direct proportional to the magnitude of D_{ij} term defined in Equation 4.6. However, in a typical NMR experiment in solution, the D_{ij} between nearby spins is average away by diffusion, due to its dependence on the angle θ_{ij}. For example, in a NMR experiment with a test tube of water, which has a diffusion coefficient of $2.57{\times}10^{-5} cm^2{\cdot}s^{-1}$ [175], this coefficient is averaged out in less than $10ms$ between spins that are few micrometers away. On the other hand, for pairs of spins that are farther apart, D_{ij} is not averaged out by diffusion over the NMR time scale. One could think that between spins that are farther apart, since D_{ij} is proportional to r_{ij}^{-3}, this interaction will be minuscule and could be discarded. However, while this is true, because the number of pairs of spins that are r_{ij} apart also increases as r_{ij}^2, the dipolar interaction of a given spin with all surrounding spins at a distance r_{ij} away decays as r_{ij}^{-1}. For this reason, long-range dipolar interaction is not negligible and can transform the anti-phase magnetization terms such as $I_{zi}I_{xj}$, originating from multiple-quantum coherences, into observable single-quantum magnetization as demonstrated in Equation 4.7.

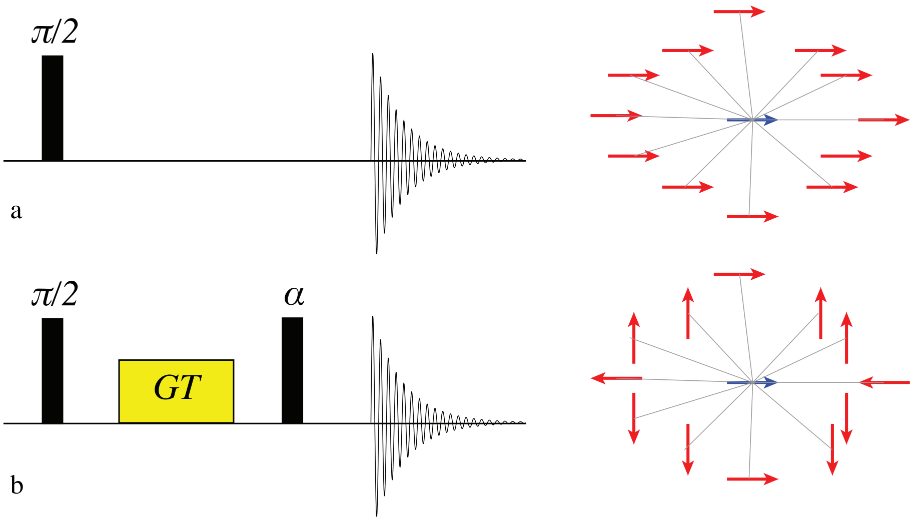

Figure 4.1: (a) Uniform distribution of magnetization in the sample. (b) Symmetry is broken up by the application of pulsed gradient in the CRAZED sequence. Adapted from [6].

However, if the magnetization is isotropically distributed, such as the case in Fig.4.1(a), D_{ij} can still be spatially averaged out. This is the reason why, to detect the signal originating from iMQC, the symmetry of the magnetization must be broken up to reintroduce the effect of long range dipolar field interaction. This is typically accomplished with a combination of RF pulses and magnetic field gradients as shown in Fig.4.1(b), or with carefully designed RF trains without the need for gradient pulses [176].

4.1.4 Applications of IMQCs

Since its discovery, iMQCs have been used in a number of MRI and NMR applications. They can give rise to a completely different contrast in MRI, which does not come from variations in spin density or relaxation times, as in traditional MRI, but from the changes in susceptibility over a subvoxel distance [177–179]. These signals have also been employed to achieve high resolution NMR spectroscopy [180] and MRI images [181] *in vivo*, as an improvement over BOLD contrast in functional MRI (fMRI) [182–184], as a means of specifically detecting brown adipose tissue *in vivo* [185–187], and to suppress solvent signal in liquid state NMR [188]. Another interesting application of iMQCs has been the suppression of both spatial [189–193] and temporal [194] inhomogeneities. iMQC signals have also been observed from different nuclei, such as between ^{13}C and ^{1}H [9, 17, 195], between ^{31}P and ^{1}H [196], and between ^{19}F and ^{1}H [197]. Distant dipolar field effects have also been employed for indirect detection [198], a subject discussed in Chapter 7.

4.2 MR Thermometry Using iZQC

As it has been described in Chapter 3, MR thermometry methods require the measurement of the chemical shift difference between a temperature probe (water) and a reference (fat). Among all iMQC varieties, water-fat iZQC signals can potentially be used to measure temperature, as iZQC signal arises from multiple quantum operators in the equilibrium density matrix and corresponds to simultaneous “flipping” of correlated spins in opposite directions. As a result, the signal naturally evolves at the resonance frequency difference between the two correlated spins. This property alone would not reduce the effect of magnetic field inhomogeneities that exists within a voxel, if it were not for the fact that the bulk of the iZQC signal actually originates from spins that are a “correlation distance” apart. The correlation distance is a “user-controlled” parameter that can be changed by altering the strength of the magnetic field gradient pulses used to break the symmetry of the magnetization and reintroduce the effect of the dipolar field interaction [173], as described before. This parameter also defines the average distance between the correlated spins from which most of the iZQC signal comes from, and it can be selected to remove macroscopic field inhomogeneities at the microscopic scale, a scale much smaller than the resolution achievable with common MRI techniques. For this reason, the water-fat iZQC signal has been used to enhance the accuracy of PRF thermometry [199, 200], and to measure absolute temperature in fatty tissues [201–203].

However, water and fat spins do not mix and typically reside in different tissue/cell compartments. In addition, water and fat have different magnetic susceptibilities. This means that microscopic susceptibility gradients that are always present at water-fat interfaces on a scale comparable to the correlation distance cannot be completely removed. This will be demonstrated in this section via both numerical simulations and *in vitro* experiments.

4.2.1 Effects of Microscopic Susceptibility Gradients on Water-Fat iZQC Thermometry: Simulations

The goal of the simulations was to study how the distribution of water and fat spins within the image voxel affected the water-fat iZQC frequency and the accuracy of water-fat iZQC thermometry methods. To understand the origin of the iZQC signal intensity and frequency as well as their dependence on sample microstructure and correlation distance, we can resort to the quantum picture of iMQCs. Briefly, following a similar derivation described in literatures [174, 204], the magnitude of the iZQC signal from two spins *i* and *j* produced by the modified CRAZED iZQC sequence sketched in Fig.4.2(a) [205] for a spherical sample can be written as:

$$S_{ij} = \frac{3\beta\hbar\omega_0}{8}\tau D_{ij}\cos\left(\gamma G T r_{ij}\cos\theta_{ij}\right) \tag{4.8}$$

where β=$1/k_BT$, γ is the gyromagnetic ratio of the spins, ω_0 is the Larmor frequency, G and T are the strength and duration of the gradient which modulates the magnetization and determines the length of the correlation distance d_c=$\pi/\gamma GT$, θ_{ij} is the angle between the internuclear vector $\vec{r_{ij}}$ and external field $\vec{B_0}$ (assumed to be along the z axis).

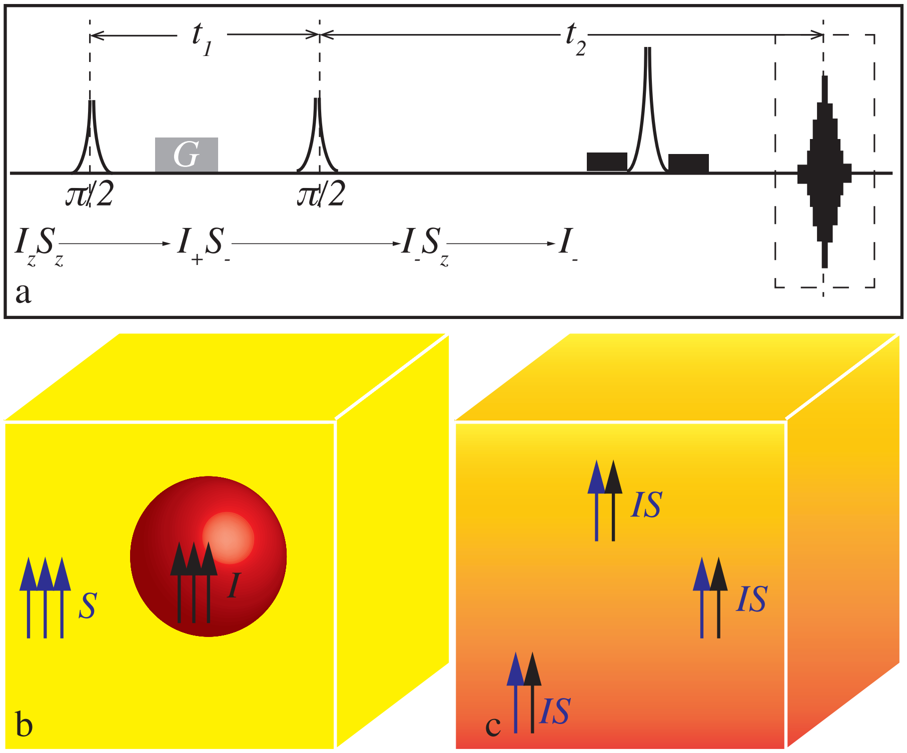
t_1
t_2
G
π/2
π/2
$I_zS_z \rightarrow I_+S_- \rightarrow I_-S_z \rightarrow I_-$
a
S
I
b
IS
IS
IS
c

Figure 4.2: (a) Modified CRAZED sequence diagram. (b) Sketch showing two spin species residing in different compartments. (c) Sketch showing two spin species residing in the same compartments in an inhomogeneous field.

Without a loss of generality, if we consider that the j spin is at the center of the spherical sample, the signal generated from its interaction with all other i spins in the sample can be written as an integral over the entire volume:

$$S(r) = |\frac{3}{32\pi}M_0 t_2\gamma\mu_0 \times \int_V r^{-3}(3\cos^2\theta - 1)\cos(\pi\cos\theta\frac{r}{d_c})(r^2\sin\theta)\mathrm{d}r\mathrm{d}\theta\mathrm{d}\phi|, \tag{4.9}$$

where M_0 is the magnetization per unit volume at equilibrium, t_2 is the duration of the acquisition window, θ and ϕ are the polar and azimuthal angles in a spherical coordinate, respectively, and s is the z-coordinate of the spin that is at a distance of r from the center of the dipole, which can in turn be written as s=$r\sin\theta$.

Equation 4.9 shows that the strength of the iZQC signal originating from spin j from its dipolar field interaction with all other spins in the sample depends on r, the internuclear distance between the interacting spins. The dependence of the signal S from r can be factorized as

$$S = |\frac{3}{32\pi}M_0 t_2 \gamma \mu_0 \times \Sigma_r \frac{\pi}{d_c} F(\frac{r}{d_c})|, \tag{4.10}$$

where F is defined as

$$F(\frac{r}{d_c}) = \frac{d_c}{\pi}\int_{\theta=0}^{\pi}\int_{\phi=0}^{2\pi} r^{-3}(3\cos^2\theta - 1)\cos(\frac{r}{d_c}\pi\cos\theta)(r^2\sin\theta)\mathrm{d}\theta\mathrm{d}\phi, \tag{4.11}$$

which can be readily solved analytically for a spherical sample as

$$F(\frac{r}{d_c}) = 8\pi \times \frac{3\pi\frac{r}{d_c}\cos(\pi\frac{r}{d_c}) + [(\pi\frac{r}{d_c})^2 - 3]\sin(\pi\frac{r}{d_c})}{(\pi\frac{r}{d_c})^4} \tag{4.12}$$

The function F, plotted against r/d_c, is shown in Fig.4.3 with r/d_c ranging from 0 to 5. This function can be essentially regarded as a weighting function for all possible dipolar interactions that exist in the sample. This weighting function shows that the bulk of the iZQC signal intensity and frequency comes primarily from coherences between spins that are about one correlation distance away. Therefore, in presence of susceptibility gradients, like those created by water-fat interfaces, the iZQC frequency is expected to vary both as a function of sample microstructure and as a function of the selected correlation distance.

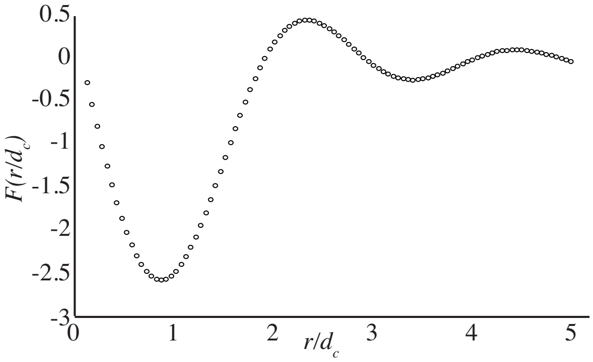

Figure 4.3: Plot of the $F(r/d_c)$ function calculated using Equation 4.12, which shows that most of the iZQC signal originates from spins that are about 1 correlation distance away.

To understand how the selection of the correlation distance could affect the water-fat iZQC frequency, we can consider a simple phantom consisting of a fat sphere immersed in water. Specifically, we used a fat sphere with a diameter of $50\mu m$ and a fat sphere with a diameter of $100\mu m$. We then computed the resonance frequency offset generated by the water-fat susceptibility mismatch between the two compartments by using COMSOL Multiphysics (COMSOL, Stockholm, Sweden), assuming an external magnetic field B_0 of 11T, and a volume susceptibility of -9.04ppm [142] for the water compartment and -7.79ppm [167] for the fat compartment. The field offset generated by the susceptibility mismatch between fat and water for the two phantoms is shown in Fig.4.4.

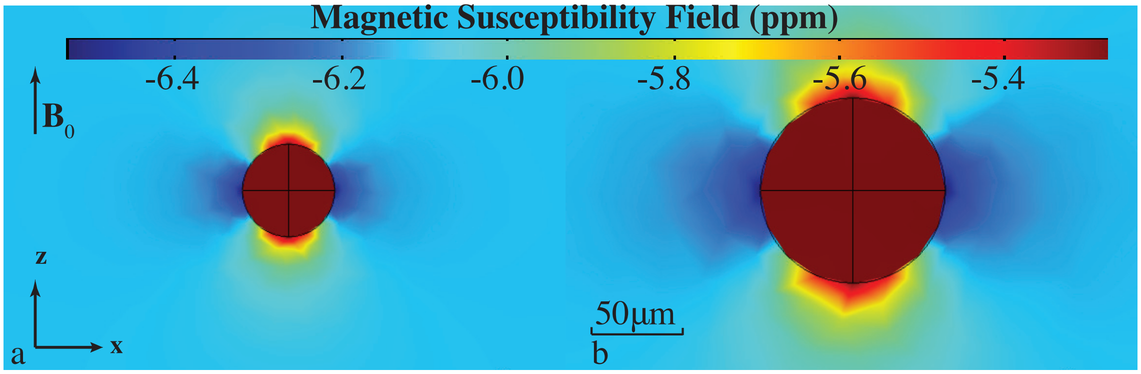

Figure 4.4: Frequency offset generated by water/fat susceptibility mismatch for (a) a $50\mu m$-diameter fatty droplet and (b) a $100\mu m$-diameter fatty droplet.

To compute the resonance frequency of the iZQC signal generated from the interaction of a lipid spin, located at the center of the sphere with frequency ω_f, with all other water spins located outside the sphere, we used the following relation:

$$\omega_{iZQC} = \frac{\omega_f - [\Sigma_{N_j} F(\vec{r_j})\omega_w(\vec{r_j})]}{\Sigma_{N_j} F(\vec{r_j})}, \tag{4.13}$$

where $\omega_w(\vec{r_j})$ is the effective water resonance frequency at position $\vec{r_j}$, and $F(\vec{r_j})$ is the iZQC weighing function defined in Equation 4.12. The water-fat iZQC frequency is computed and plotted in Fig.4.5 for four correlation distances: $25\mu m$, $50\mu m$, $100\mu m$ and $200\mu m$. As expected, for a given correlation distance, the iZQC frequency depends on the sample microstructure. More importantly, for a given microstructure, a change of the correlation distance causes a change of the water-fat iZQC frequency. These dependences are not surprising for non-mixing spins, like water and fat, which reside in different tissue compartments with different magnetic susceptibilities.

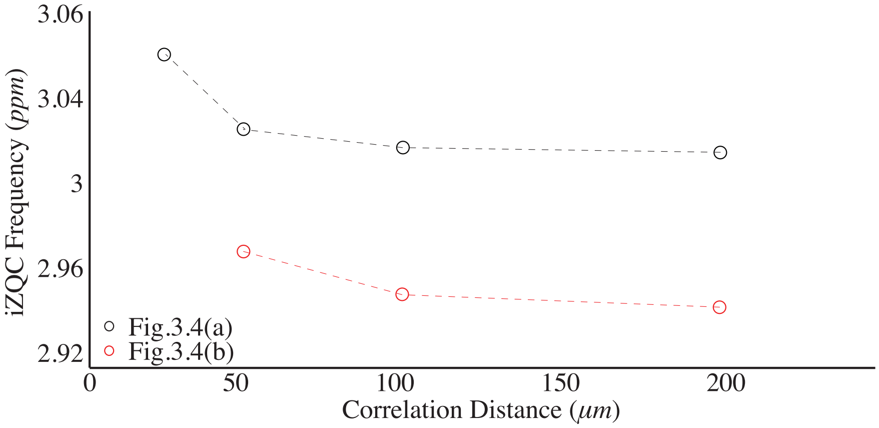

Figure 4.5: Computed water-fat iZQC frequencies for the geometries shown in Fig.4.4 as a function of correlation distance d_c.

4.2.2 Effects of Microscopic Susceptibility Gradients on Water-Fat iZQC Thermometry: *In Vitro* Experiment

4.2.2.1 Water-fat iZQC Sequence

To facilitate the analysis of a pulse sequence using the product operator formalism, we first need to introduce the raising (I_+) and the lowering (I_-) operators, defined as:

$$I_+ = I_x + iI_y; \tag{4.14a}$$

$$I_- = I_x - iI_y, \tag{4.14b}$$

with I_+ having a coherence order of +1 and I_- having a coherence order of -1. By using these operators, iZQCs can be easily expressed as I_+S_- or I_-S_+, whereas iDQCs can be expressed as I_+S_+ or I_-S_-. Other advantages of using the raising and lowering to describe how the transverse magnetization evolve with time are two folds. First, they rotate about the z-axis with a frequency of $+\omega_0$ and $-\omega_0$, respectively. Second, unlike I_x and I_y, the evolution of $I_\pm$ under chemical shift or a magnetic field pulsed gradient can be expressed as a phase shift of $\mathrm{e}^{\mp i\omega t}$ or $\mathrm{e}^{\mp i\gamma GT}$.

Sequence used to acquire the water-fat iZQC signal is developed based on the CRAZED sequence [205] and it is shown in Fig.4.6. The coherence pathway selected in this study is shown at the bottom of the figure using the raising and lowering operators. Specifically, the iDQC signal that evolves during delay t_1' is transferred into the iZQC by the first 180° pulse. The iZQC signal evolves during delay t_1'' and is then transformed into iSQC by the second 90° pulse. The iSQC signal is then transformed by the dipolar field interaction from anti-phase magnetization I_-I_z into an in-phase, detectable magnetization I_- during delay t_2. The use of a double quantum filter effectively suppresses all spurious signals that are first excited by the second 90°RF pulse. A series of FIDs is acquired using different values for delay t_1'', the indirect (F1) dimension. The resulting 2D spectrum has the resonance frequency of I spin ω_I on F2 (direct dimension) axis and the resonance frequency difference between I and S spins $\omega_S - \omega_I$ on F1 axis. A more detailed description of the working mechanism of the iZQC sequence can be found in Chapter 7.

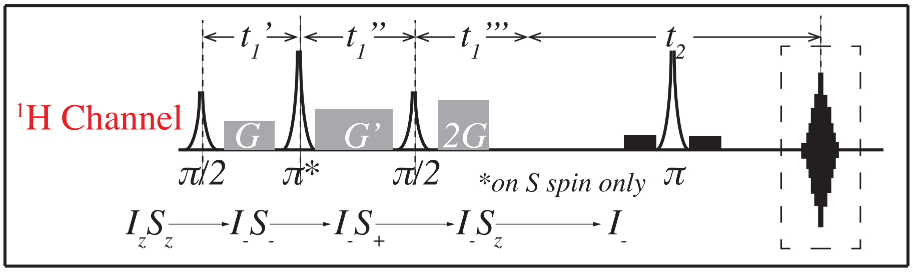

Figure 4.6: Water-fat iZQC sequence used in this study as a modification to the original CRAZED sequence.

4.2.2.2 Experimental Methods

Water-fat iZQC spectroscopic studies were performed on a Varian Inova 500MHz NMR spectrometer (Varian NMR Systems, Palo Alto, CA). To evaluate the effect of microscopic susceptibility gradients on the water-methylene iZQC signal, we performed experiments as function of temperature on various samples containing mixtures of water and lipid spins. Two samples consisted of stable homogenous emulsions of corn oil and distilled water with a fat fraction (FF) of 40% and 80%, prepared by following the same procedure described in [206]. Another sample was prepared by mixing ovine fat and muscle to achieve, roughly, a 1:1 fat/muscle ratio (WAT/Muscle sample). All scans were performed within two days to minimize chances of any separation or degradation of the samples. Temperature dependence of water-fat iZQC frequency was studied by controlling the sample temperature with a temperature controller (L900, Highland Technology, San Francisco, CA). To control the temperature with high precisions, the on-board Biopack mode was activated to achieve an accuracy of 0.1°C. Temperature was also calibrated by using the chemical shift separation between the methyl and hydroxyl protons in a 100% methanol sample. Temperature was set nominally at 25°C, 32°C, 39°C and 45°C and the samples were allowed to reach equilibrium for one hour before iZQC spectra were acquired. First and second-order shimming gradients were used to reduce the line widths of both water and fat peaks to acceptable levels. All water-fat iZQC spectra were acquired with the methylene peak placed at approximately $400Hz$ off resonance. The iZQC resonance frequency was calculated by phase fitting the FID.

4.2.2.3 Experimental Results

Fig.4.7 shows examples of 2D water-fat iZQC spectra acquired by selecting a correlation distance of $100\mu m$. The prominent peak appeared at $(F1, F2)$=$(\Omega_f - \Omega_w, \Omega_f)$, which is the water-fat iZQC. A small contamination generated by the methylene-olefinic iZQC signal is also observed but is several-fold weaker in intensity and does not affect the phase fitting. Because of the coarse resolution used along the F1 dimension (156Hz/px), the temperature shift of the water-fat peak is barely visible. The water-fat iZQC frequency, calculated from the signal phase evolution, was (3.462±0.023)ppm, (3.363±0.009)ppm, (3.311±0.010)ppm and (3.251±0.009)ppm at 25.7°C, 32.8°C, 40.0°C and 46.0°C, respectively.

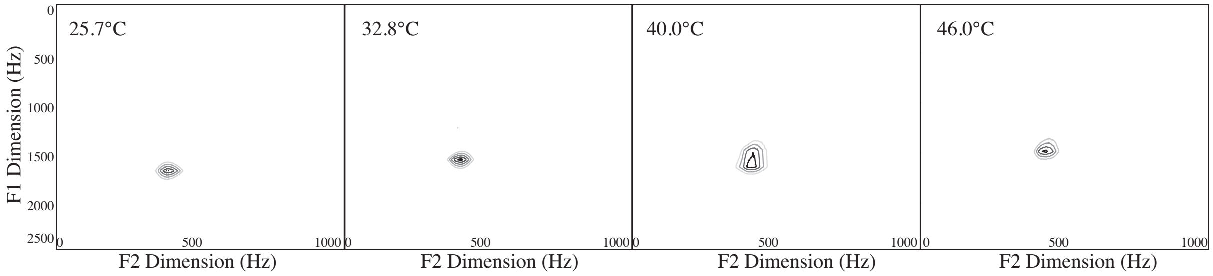

Figure 4.7: 2D spectra acquired from the WAT/Muscle sample at four temperatures showing the water-methylene iZQC peak between water and fat spins.

The temperature dependence of water-fat iZQC frequency is plotted in Fig.4.8 for all samples. Water-fat resonance frequency difference as measured by 1D spectroscopic experiment in the same samples is also reported in the figure. As can be clearly observed in Fig.4.8, the water-fat iZQC resonance frequency differed substantially from the water-fat frequency separation obtained by 1D spectroscopy, especially for the emulsion samples. Also, the difference between these two frequencies was consistently higher when small correlation distances were selected. More interestingly, despite the water-fat resonance frequency difference as measured using 1D spectra not varying substantially among the 3 samples (the largest variation is of

0.02ppm between the WAT/muscle and the emulsion samples), the water-fat iZQC frequency varied as much as 0.34ppm, even when the same correlation distance was selected. Even between the 40% emulsion sample and the 80% emulsion sample, the water-fat iZQC frequency varied by as much as 0.02ppm, whereas the water-fat separation in the 1D spectra varied by less than 0.008ppm. Not surprisingly, the water-fat iZQC frequency difference across all samples was higher at smaller correlation distances, where the difference between the two microstructures differed the most. Expected was also the variation of the water-fat iZQC temperature coefficient, which varied between -0.0101ppm/°C and -0.0092ppm/°C between the WAT/muscle and the emulsion samples. The temperature coefficient of the water-fat iZQC frequency displayed a variation also as function of the correlation distance of about 2% and 10%, in the 40% and 80% emulsion samples, respectively, whereas the variation was 20% in the WAT/muscle sample.

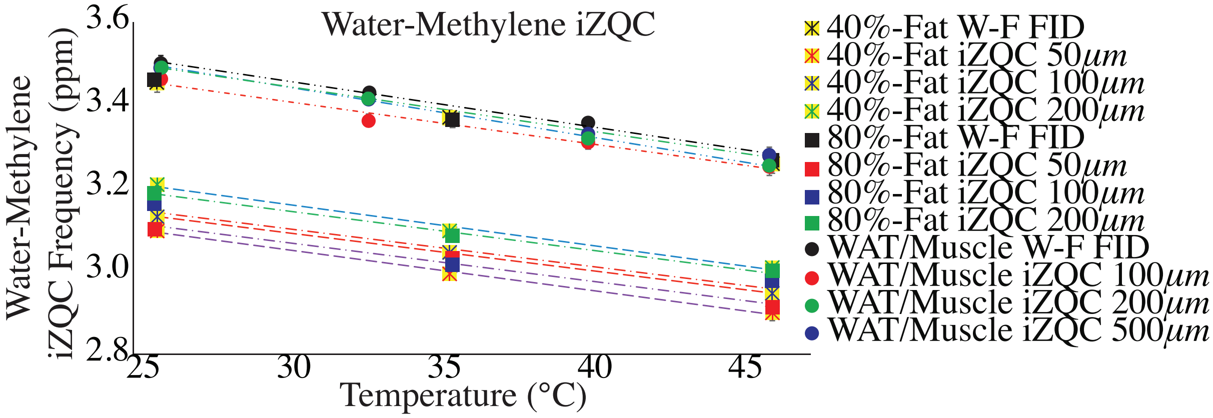

Figure 4.8: Dependence on correlation distance and temperature displayed by water-fat iZQC frequency.

Quantitatively, the water-fat curves showed an R^2 value of ≥0.995 except for the ones acquired with a correlation distance of 100μm, which had an R^2 of around 0.990. For the water-fat iZQC, the temperature coefficients and the y-intercepts averaged to (-0.0099±0.0003)ppm/°C and (3.510±0.064)ppm, respectively. For comparison, peaks acquired by single-pulse proton spectra (which can be considered as using an infinitely large correlation distance) were fit to a mixed Lorentzian-Gaussian function to read the chemical shifts of water and fat peaks. The temperature coefficient of the chemical shift difference between the water and fat peaks among all the samples averaged to (-0.0099±0.0005)ppm/°C while the *y*-intercept averaged to (3.725±0.031)ppm.

4.2.3 Discussion and Conclusions

Recently it was proposed that the water-fat iZQC resonance frequency could give rise to more accurate temperature measurements as the iZQC signal provides a measurement of the water-fat resonance frequency difference at a much smaller scale than typically probed by MRI [200, 203]. However, water and fat spins are never found in the same tissue or cell compartment and susceptibility gradients, always present at water-fat interfaces, are expected to shift the frequencies of water and methylene spins not necessarily in the same direction. Since the effect of these susceptibility gradients is higher in regions close to tissue interfaces, and since the bulk of the water-fat iZQC signal originates from water and fat spins that are only a few tens of micrometers away when small correlation distances are selected, a strong dependence of the water-fat iZQC frequency on sample macrostructure should be expected. Yet, despite many reports indicating that this is indeed the case for samples with very similar structure and composition [200], this dependence has never been investigated. In this section, we have clearly showed that susceptibility gradients not only produce shifts of the water-fat iZQC frequency as large as 0.4ppm between different samples, but are also responsible for a dependence of the iZQC resonance frequency on the correlation distance. The water-fat iZQC resonance frequency variation is considerably higher than what is observed from 1D spectroscopic measurements between water and fat protons, underlining the stronger effect that susceptibility gradients have at the smaller scale probed by the iZQC signal. Not surprisingly, the difference between the water-fat frequency separation and the water-fat iZQC frequency was higher when short correlation distances were used, and it became smaller at longer correlation distances. This dependence of the water-fat iZQC frequency on sample microstructure clearly precludes the possibility of performing absolute MR thermometry, as the specific water-fat iZQC frequency depends not only on temperature, but also on sample microstructure and on the specific choice of the correlation distance. In addition, this dependence also precludes the possibility for accurate relative temperature measurements in tissues where the water-fat content may change. This is the case in brown adipose tissue, a fatty tissue specialized in non-shivering thermogenesis [207], a process during which the in-tissue lipid content is expected to vary [208, 209].

In this study, we also observed a small variation of the water-fat iZQC temperature coefficient as a function of the sample used, which was also observed in a previous study [200]. The dependence of the water-fat iZQC temperature coefficient with sample structure and correlation distance is not surprising since the magnetic susceptibility of fat has a large temperature dependence. This inevitably affects the field offset distribution at the microscopic level probed by the water-fat iZQC resonance frequency. In this study, the water-fat iZQC temperature coefficient varied by more than 20% between the two emulsions, and by as much as 30% between the emulsions and the WAT/muscle sample. These variations in the temperature coefficient can make even relative temperature measurements inaccurate, if the temperature dependence of the water-fat iZQC resonance frequency is not known for the specific tissue, as is often the case.

In summary, we have shown that microscopic susceptibility gradients affect the accuracy of water-fat iZQC thermometry methods. The choice of the correlation distance in this sequence and the specific distribution of water and fat spins at the microscopic level have a profound effect on the water-fat iZQC frequency and its temperature coefficient, undermining the accuracy of MR thermometry methods that use this signal to measure absolute or relative temperature changes. In order to completely remove the effect of macro and microscopic susceptibility gradients, we need to identify a temperature sensitive resonance frequency (the probe) that completely mixes with the temperature-insensitive resonance frequency (the reference) at the microscopic level. This concept will be further investigated in the second half of Chapter 7.

CHAPTER 5: TEMPERATURE DEPENDENCE OF LIPID-DISSOLVED ^{129}XE RESONANCE FREQUENCY

Apart from ^{1}H, ^{129}Xe has attracted some interest as a potential temperature probe for MR thermometry. By virtue of having a large electron cloud, the chemical shift of xenon is very sensitive to changes in its physical and chemical environment. Schilling *et al.* leveraged on this property to develop a ^{129}Xe-based temperature sensor [210]. Specifically, the large chemical shift difference between cryptophane-bound [211] xenon and unbound xenon and its strong temperature dependence (-0.29ppm/°C) was used to measure absolute temperature *in vitro* in an aqueous suspension at a concentration of 150M with an accuracy of 0.1°C.

^{129}Xe also has a high affinity for lipids, where its solubility is 20 times higher than that in water [212]. In addition, the temperature coefficient of the resonance frequency of ^{129}Xe was measured to be -0.21ppm/°C when it was dissolved into olive oil and -0.25ppm/°C when it was dissolved into corn oil [213]. Later our group found a temperature dependence of the chemical shift of ^{129}Xe dissolved in adipose tissue *in vivo* [73]. The scope of this work was to completely characterize this temperature dependence *in vitro* by using high resolution NMR. In addition, as LDX and fat spins reside in the same tissue and cell compartment, we sought to evaluate whether lipid protons could be used as an internal temperature-insensitive reference to compensate for the effects of magnetic field drift, motion, and susceptibility gradients on LDX frequency at both the macro and microscopic level.

5.1 Temperature Dependence of ^{129}Xe Resonance Frequency

The initial discovery of the temperature dependence of xenon resonance frequency in 1969 [214] led to further investigations in xenon gas [215], xenon trapped inside inorganic or cryptophane cages [216] and xenon dissolved in different solvents [217]. As stated in Chapter 2, the xenon chemical shift stems from the electron shielding of the nucleus. Whereas an isolated xenon atom has an entirely diamagnetic shielding, any deviation from spherical symmetry brought about by interactions with another atom or molecule creates paramagnetic shielding contributions that deshield xenon nucleus from the external magnetic field [218]. This deshielding results in a slight change in the local magnetic field: B_{loc}=(1-σ)B_0. The resulting Larmor frequency is then changed to ω=γB_0(1-σ) [219]. The deshielding factor is known to depend on the distance between the xenon atom in question and its neighbors, as well as on the angle between the interatomic vector and the B_0 field [215]. The deshielding factor of xenon nucleus has been suggested to come from several sources, and can be described as:

$$\sigma = \sigma_a + \sigma_{\mathrm{E2}} + \sigma_e + \sigma_w + \sigma_{\mathrm{rep}} \tag{5.1}$$

where σ_a is the shielding originating from the magnetic anisotropy of the solvent molecules, σ_{E2} is the shielding caused by the permanent electric dipole moment of the solvent, σ_e arises from the reaction field induced in the solvent by the permanent electric dipole of the solute, σ_w is the shielding due to the dispersive part of the van der Waals force, and σ_{rep} arises from the repulsive part of the van der Waals force [220]. Of these terms, σ_{E2}, σ_a and σ_e are known to be in the ppm range, and thus can be omitted when compared to the larger than 100ppm chemical shift displayed by xenon when dissolved in solvents. The remaining van der Waals terms come from intermolecular interactions between xenon and neighboring atoms. The contribution to the chemical shift of xenon due to these interactions was often studied empirically in early literatures, with models based on the reaction field theory of Onsager, which describes the solvent as a continuum. A function of the refractive index of the pure solvent, $f(n) = [\frac{n^2-1}{2n^2+1}]^2$, was found to have a linear correlation with xenon resonance frequency, based on the assumption that σ_w was the dominant contributing factor in Equation 5.1 [221]. A later model used the assumption that the chemical shift of xenon is directly proportional to the dispersion energy between the xenon-solvent pair, which could be calculated using the PISA (Pair Interaction Structureless Approximation) model [222, 223]. Other empirical models that have been proposed hypothesized that the xenon chemical shift increased linearly with the length of the backbone of the triglyceride chain [224, 225]. Further analysis that took into account the difference in the mass densities among chains of different lengths suggested a decrease of the chemical shift with the increasing number of -CH_2- units [226].

To model and quantify the temperature dependence of the chemical shift of xenon dissolved in porous solids, Cheung [7] proposed a theoretical framework that can be applied to xenon dissolved in lipids. The structure of the porous solid is shown in Fig.5.1.

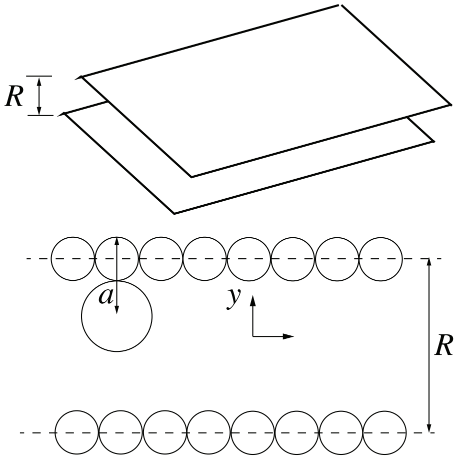

Figure 5.1: Schematic showing a xenon atom diffusing through a polymer matrix. Reproduced from [7].

In this model, the dissolved xenon atom, represented by the large circle, is confined between two infinitely large parallel layers. The small circles depict the surface atoms. The sum of their van der Waals radii is a, and the separation of the layers, measured from center to center of opposite surface atoms, is R. The y coordinate, perpendicular to the layers, extends from -R/2 to R/2. Using this model, the author argued that the interactions between xenon and surface atoms would give rise to a potential energy $U(\mathbf{r})$, which would determine the chemical shift of xenon. In a confined volume such as this model, the chemical shift of xenon δ is proportional to the van der Waals polarization level and is given by the canonical ensemble average:

$$\delta(T) = \frac{\int^{V} \mathrm{d}\mathbf{r}\delta(\mathbf{r}) \exp\left[-U(\mathbf{r})/kT\right]}{\int^{V} \mathrm{d}\mathbf{r} \exp\left[-U(\mathbf{r})/kT\right]} \tag{5.2}$$

where V is the volume of the pore and T is the temperature. To model the potential energy, the author used the sum of the Lennard-Jones 6-12 potentials between each pair of xenon and surface atoms as $U(\mathbf{r}) = -4\epsilon[(a/r)^6 - (a/r)^{12}]$, with ϵ being the depth of the potential well [227]. By integrating over both layers, $U(\mathbf{r})$ can be rewritten as follows:

$$U(y) = -\frac{2\pi\epsilon n}{5}\{\frac{5(R/2a - y/a)^6 - 2}{(R/2a - y/a)^{10}} + \frac{5(R/2a + y/a)^6 - 2}{(R/2a + y/a)^{10}}\}, \tag{5.3}$$

with $-R/2<y<R/2$. The shape of $U(y)$ is plotted in Fig.5.2 for various ratios between R and a. From this figure it is clear that when the separation between two layers is comparable to the size of xenon atom ($R/a<2.4$), the repulsion part of the Lennard-Jones potential becomes the determining factor of the shape of U. In this scenario, through calculations which will not be shown here, the author concluded that the chemical shift would increase with temperature.

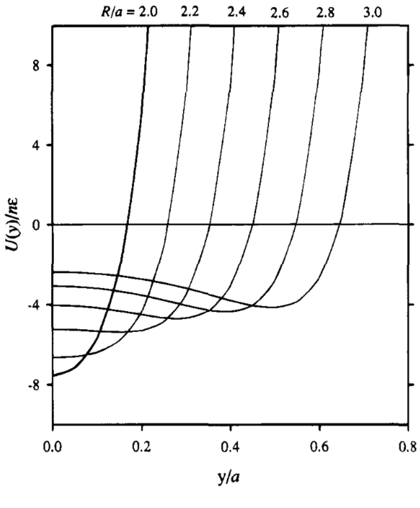

Figure 5.2: Potential $U(y)$ described in Equation 5.3 for a xenon atom in a layerlike pore as a function of the position of the xenon atom and layer separation. Reproduced from [7].

On the other hand, when $R/a>2.4$, the attractive part $W(\mathbf{r})$ of the potential energy $U(\mathbf{r})$ will dominate and the xenon chemical shift will decrease as temperature is raised. Since the temperature coefficient of xenon dissolved in lipids has a negative temperature dependence, this second scenario shall apply. In this case, using perturbation theory, Kromhout *et al.* [228] suggested that the chemical shift of xenon is directly proportional to $W(\mathbf{r})$ as $\delta(\mathbf{r})$=-$cW(\mathbf{r})$, where c is a positive constant. It is therefore valid to limit the integration in Equation 5.2 to a volume V-v in which xenon atom experiences an attractive potential:

$$\delta(T) = -\frac{\int^{V-v} \mathrm{d}\mathbf{r} c W(\mathbf{r}) \exp\left[-W(\mathbf{r})/kT\right]}{\int^{V-v} \mathrm{d}\mathbf{r} \exp\left[-W(\mathbf{r})/kT\right]} \tag{5.4}$$

Equation 5.4 is prohibitively difficult to evaluate directly using the Lennard-Jones potential shown in Fig.5.2. To simplify the calculations, Cheung used the paired square-well potential model in Fig.5.3. The well has a depth of ϵ' and a width of l. Using the fact that the chemical shift of xenon atom is $\delta(\mathbf{r})$=$c\epsilon'$ inside the well and zero elsewhere, the author integrated Equation 5.4 over a volume of V^*=V-aS, with S being the surface area of the pore. The temperature dependence of the chemical shift of xenon atom is then shown as noticing that the layer separation R is given by $2V/S$:

$$\delta(T) = c\epsilon'\left[1 - \frac{1}{\frac{2l\exp(\epsilon'/kT)}{R-2a-2l} + 1}\right]. \tag{5.5}$$

The temperature dependent term in Equation 5.5 is $\frac{2l\exp(\epsilon'/kT)}{R-2a-2l}$. From Fig.5.2 it can be easily concluded that $R \geq 2(a+l)$. Consequently this term is positive. As bilayers expand when temperature elevates, their separation R increases, which makes the denominator greater. This coupled with the diminishing numerator as temperature increases leads to an overall negative temperature coefficient of that the chemical shift δ, which is consistent with experimental observation.

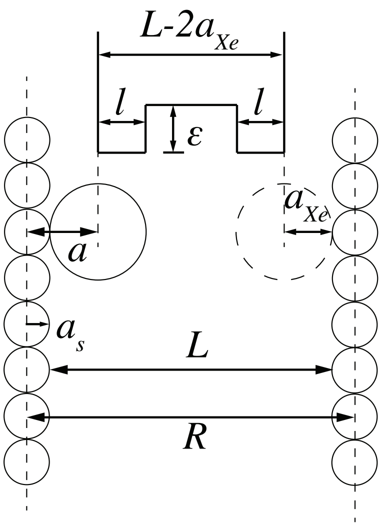

Figure 5.3: Schematic showing the simplification of the potential energy as paired double quantum-well. Reproduced from [7].

Alternatively, Saunavaara *et al*. [229] simplified the calculation of the temperature dependence of the chemical shift of xenon dissolved in isotropic solvents by using the pairwise additivity for xenon shielding perturbations proposed in [230]:

$$\delta_{Xe} = \delta_0[1 - (\alpha + \sigma)(T - T_0)], \tag{5.6}$$

where α is the thermal expansion coefficient of the solvent, δ_0 is the chemical shift of the gaseous phase and σ is the temperature dependence of the shielding factor.

5.2 Effects of ^{129}Xe-^{129}Xe Interaction on ^{129}Xe Resonance Frequency

Though it was originally thought that the resonance frequency of xenon had a linear temperature dependence, Adrian *et al*. extended the theory to describe the additional dependence on ^{129}Xe density with good experimental agreement [231]. Later, Jameson *et al*. determined that the higher order virial coefficients in the expansion of the shielding factor with respect to density, such as the second virial coefficient σ_1, are also temperature dependent, in the form of [232]

$$\sigma(\rho, T) = \sigma_0(T) + \sigma_1(T)\rho + \sigma_2(T)\rho^2 + \sigma_3(T)\rho^3 + ..., \tag{5.7}$$

where σ_1 is contribution to the shielding effect from two-body collisions between xenon atoms, and σ_2 and higher order terms represent contribution from the three-body and many-body collisions, respectively. This results in a density dependence of xenon chemical shift. For spherical nuclei such as rare gas, σ_1 can be described by adopting the potential functions for binary interactions, and the chemical shift of xenon in the limit of zero mole fraction can be calculated as [233]:

$$\sigma_1(T) = \iiint \sigma(R, \theta, \phi) \exp\left[-V(R, \theta, \phi)/k_B T\right] \times R^2 \mathrm{d}R \sin\theta \mathrm{d}\theta \mathrm{d}\phi \tag{5.8}$$

with the term $\exp\left[-V(R, \theta, \phi)/k_B T\right]$ giving rise to the temperature dependence of σ_1.

Although Equation 5.8 is difficult to solve analytically, Jameson *et al.* conducted experiments to empirically measure the temperature dependence of σ_1, as shown in Equation 5.9 [234, 235].

$$\begin{aligned}\sigma_1(T) =&0.553 + 0.1114 \times 10^{-2}\tau - 0.765 \times 10^{-5}\tau^2 + 0.436 \times 10^{-7}\tau^3 \\ &- 0.132 \times 10^{-9}\tau^4 - 0.545 \times 10^{-12}\tau^5 \text{ppm} \cdot \text{agamat}^{-1}\end{aligned} \tag{5.9}$$

with τ=T-300K. Equation 5.9 is extremely important in calibrating the density of xenon based on its chemical shift in both the gaseous and absorbed phases. The presence of another gas species A, such as oxygen, also contributes to the first virial coefficient, as Equation 5.7 becomes:

$$\sigma \approx \sigma_0 + \sigma_1(Xe - Xe)\rho_{Xe} + \sigma_1(Xe - A)\rho_A + ... \tag{5.10}$$

Jameson *et al.* have measured these coefficients extensively between xenon and various gas agents and determined that $\sigma_1(Xe - A)$ ranged from 3120 to 12280ppm/($mol{\cdot}cm^{-3}$) [236].

5.3 Characterization of LDX Chemical Shift

5.3.1 Methods

To characterize the temperature dependence of LDX chemical shift and facilitate its comparison with fat-referenced PRF thermometry method, the same types of tissues in Chapter 3 were used. After filling the NMR tube with tissue, the tube was connected to a vacuum/charge system equipped with a rotary pump, a precision pressure gauge (precision up to 0.01psi) and a xenon cylinder using a long plastic tubing with a dead volume of about $317cm^3$. The vacuum system was carefully placed outside of the 5 Gauss line of the fringe field of the spectrometer. After evacuating the entire system (NMR tube + connecting tubing) while the NMR tube was kept frozen in liquid nitrogen with the rotary vacuum pump, ^{129}Xe ($>86\%$ isotopic enrichment) gas was introduced into the closed system until a specific pressure was reached. All 90°-acquisition NMR spectra were fit with a custom-written MATLAB program using a Voigt function to calculate the frequency of LDX peak.

5.3.2 Results

Fig.5.4 shows the representative ^{129}Xe spectra acquired on the rWAT sample on the high-resolution NMR spectrometer, which can be compared to the proton spectra acquired on the same sample shown in Fig.3.7. The LDX resonance frequency could be detected with high SNR even at relatively low concentration (~1 amagat) thanks to the high solubility of xenon in fat [237] as evidenced in Fig.5.4(a). The drifting of LDX peak towards lower frequency as temperature increased can be clearly observed in Fig.5.4(b). Given the high SNR of both spectra and the relatively narrow line widths, we were able to determine xenon resonance frequency with high accuracy in all samples by using custom-written MATLAB code for peak fitting with an example shown in Fig.5.4(c). Specifically, the LDX resonance frequency was determined with an error of less than 0.01ppm, except for the rWAT/Muscle sample. In this sample, the error in the determination of the

LDX resonance frequency was slightly higher as the field inhomogeneity was not completely removed by shimming gradients. Interestingly, despite the presence of muscle in the rWAT/Muscle sample, due to the very low solubility of xenon in non-fatty tissues we were able to detect only the resonance frequency of LDX.

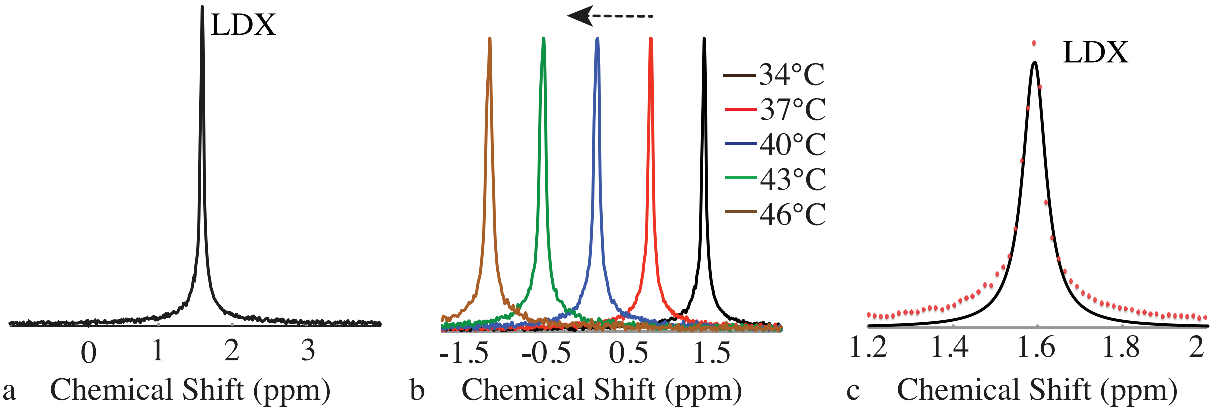

Figure 5.4: (a) Example of an LDX spectrum at 26°C for the rWAT sample. (b) Drifting of the LDX peak with temperature. (c) MATLAB fitting of the peak shown in (a) using a Voigt peak shape.

Fig.5.5 shows the temperature and pressure dependence of the LDX chemical shift in various samples, which can be compared to Fig.3.8. By increasing xenon gas pressure in the system, an increasing amount of xenon dissolved in the sample, leading to an increase in LDX signal intensity in Fig.5.5(a) and in its frequency, caused by the ^{129}Xe-^{129}Xe interactions described previously. As Fig.5.5(b) shows, the LDX resonance frequency presented a very similar temperature coefficient across all samples, averaging to -0.208ppm/°C with a standard deviation of only 0.002ppm/°C. In addition, when the methylene frequency in Fig.3.8(a) were used as internal reference (Fig.5.5(c)), the difference in the chemical shift of the referenced LDX (rLDX) chemical shift between the 3 samples reduced from 0.4ppm to 0.3ppm between the hWAT and rWAT sample, and from 0.2ppm to less than 0.02ppm between the rWAT and the rWAT/muscle sample. The larger difference in the rLDX frequency between the rWAT/Muscle and the hWAT sample suggests a small dependence of the LDX frequency on fat composition, which is expected between humans and rodents due to their very different diets. An increase in rLDX frequency was also observed for pressure greater than 2.5 atm. Specifically, at 3 atm (red peak in Fig.5.5(a)) the rLDX chemical shifts increased slightly by about

0.33ppm. The chemical shift temperature dependence of LDX also increased slightly between 2 atm and 3 atm, jumping from -0.2089ppm/°C to -0.2138ppm/°C.

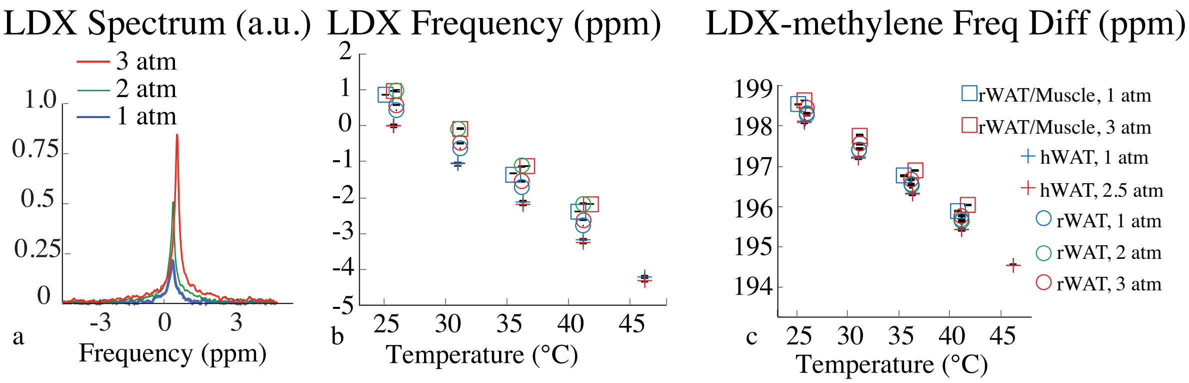

Figure 5.5: (a) LDX spectra at 26°C for the rWAT sample at different xenon gas pressures. (b) Temperature and pressure dependence of LDX resonance frequency. (c) Temperature and pressure dependence of LDX-methylene resonance frequency difference.

We should also point out that in all temperature studies we noticed a small increase in xenon pressure as temperature was raised, most likely due to the temperature dependence of xenon solubility in fat. However, since this increase was smaller than 0.3psi, it was not considered to have had an impact on the validity of the results. Interestingly, in the rWAT/muscle sample, despite the accidental redistribution of water and fat tissues between the 1atm and 3 atm measurements, which drastically altered the water-fat chemical shift difference as evident in Fig.3.8(c), the temperature coefficient of LDX was modified by less than 0.013ppm/°C. When fat was used as a reference, the temperature coefficient of the rLDX chemical shift was modified by an even less amount of -0.011ppm/°C. In summary, all temperature curves shown in Fig.5.5 averaged to have a temperature coefficient of -0.2104ppm/°C and a y-intercept of 203.55ppm, which means an absolute temperature T can be deduced from the LDX-methylene chemical shift difference ω by

$$T(^{\circ}C) = (203.55(\mathrm{ppm}) - \omega(\mathrm{ppm}))/0.2104(\mathrm{ppm}/^{\circ}C), \tag{5.11}$$

which will be used in the later chapters for *in vivo* temperature mapping.

5.4 Discussion and Conclusions

One of the aims of this chapter was to measure the temperature coefficient of LDX in adipose tissues under well-controlled pressure and temperature conditions. The temperature coefficient of LDX measured in this study was -(0.2104±0.0018)ppm/°C, similar to what we previously found *in vivo* [73] and what has been reported for ^{129}Xe dissolved in olive oil [213]. We also showed that the use of methylene protons as an internal reference for the LDX chemical shift is able to completely remove the effect of macroscopic and microscopic magnetic field inhomogeneities. This is not surprising as LDX and methylene protons reside in the same tissue compartment and, as such, they experience the same field perturbation. We also measured a small difference in chemical shift of less than 0.3ppm between the LDX signal originating from hWAT and rWAT samples. This difference is more likely due to a different fatty acid profile between human and rodent adipose tissues, to which xenon is also expected to be sensitive.

A pressure dependence of the LDX frequency was also observed in samples equilibrated at pressures above 2.5 atm. This pressure dependence likely arises from ^{129}Xe-^{129}Xe interaction, which is expected to have an impact only at very high LDX concentrations. Considering the high solubility of xenon in adipose tissue, this pressure dependence seems to appear only when an in-tissue xenon concentration exceeded 100*m*M, *i.e.* orders of magnitude higher than the concentration achievable *in vivo* in tissues upon inhalation of xenon gas. As such, this pressure dependence is not expected to affect the accuracy of *in vivo* LDX MR thermometry.

In summary, in this chapter the chemical shift temperature dependence of lipid-dissolved xenon was measured *in vitro* on 3 samples containing different types of adipose tissues. Unlike fat-referenced PRF results presented in Chapter 3, LDX and fat spins reside in the same tissue compartment and, when the LDX is referenced to the methylene protons, both macro and microscopic magnetic field inhomogeneities can be completely removed, allowing for more accurate MR temperature measurements.

CHAPTER 6: APPLICATION OF LDX-BASED MR THERMOMETRY

In Chapter 5 we characterized the temperature dependence of the LDX chemical shift *in vitro*. Both the chemical shift itself and its temperature coefficient have been demonstrated to stay relatively constant across a number of tissue types. In this chapter we will use this temperature coefficient to measure temperature *in vivo* using hyperpolarized ^{129}Xe. The use of HP ^{129}Xe is necessary to compensate for the low concentration achievable *in vivo* in tissues after the inhalation of HP ^{129}Xe gas. The LDX-based MR thermometry method will first be validated *in vivo* in rodents, whose body temperature can be easily manipulated and controlled under anesthesia. Temperature maps in rodents are acquired in the abdominal fatty layers, where the high concentration of ^{129}Xe can generate sufficient SNR. We also assess the feasibility of referencing the chemical shift of LDX to that of methylene protons to obtain absolute temperature information by using the LDX-methylene chemical shift temperature calibration found *in vitro* in Chapter 5. Temperature measurements are finally performed in human subjects. Specifically, we measured the absolute temperature of brown adipose tissue, a type of fatty tissue in which xenon accumulates at high concentrations during cold exposure.

6.1 *In Vivo* Validation in Rodents

For all *in vivo* studies mice were ventilated with a home made HP gas-compatible constant volume ventilator [238] at a rate of 100 breaths per minute with a gas mixture consisting of 75-vol% N_2 and 25-vol% O_2 for a total tidal volume of 0.2mL. During ^{129}Xe imaging, the 75-vol% of N_2 was switched to 75-vol% of HP Xe. Under the same experimental setup as described in Chapter 3, an additional xenon surface coil (1-cm diameter, transmit and receive, resonant at 110.76MHz, without ^{1}H decoupling) was placed underneath the abdominal fatty layer of the mouse. The mouse was then placed inside a volume ^{1}H coil. The temperature of the bore of the magnet was heated by an electric heater, which blew heated air until the rectal temperature of the mouse was equal to a set temperature. The abdominal temperature was assumed to be the same as the rectal temperature. ^{129}Xe frequency maps were collected using a CSI protocol without slice selection and with a 90° flip angle adiabatic BIR4 (B_1-insensitive rotation-4) pulse to compensate for the B_1 inhomogeneities of the surface xenon coil.

The CSI spectra were analyzed and fit with custom MATLAB codes using a Voigt function to calculate the frequency of lipid-dissolved xenon. To calculate the absolute temperature, the chemical shift of LDX was referenced to the chemical shift of nearby methylene protons (rLDX) using the following procedure. The methylene frequency was first placed at 1.3ppm from a fictitious ^{1}H center frequency (*fHCF*). The LDX chemical shift was then calculated with respect to a fictitious ^{129}Xe center frequency (*fXeCF*), which is linked to the *fHCF* by: $fXeCF = fHCF \cdot \frac{\gamma_{Xe}}{\gamma_H}$. This way, the chemical shift/temperature calibration found at 11T *in vitro* could be easily scaled down to 9.4T for *in vivo* temperature measurements.

6.1.1 *In Vivo* Temperature Measurement Results in Rodents

Fig.6.1 shows representative LDX relative temperature maps acquired *in vivo* from the abdomen of one of the anesthetized obese mice acclimated at 3 different bore temperatures. This can be compared to the relative temperature maps obtained using PRF method on the same mouse shown in Fig.3.9. The yellow arc in Fig.6.1(b) indicates the positioning of the xenon surface coil. Figs.6.1(c∼e) were all acquired with an axial slice orientation. Temperature maps were calculated from ^{1}H and ^{129}Xe CSI spectra using an LDX temperature coefficient of -0.21ppm/°C in pixels where the fitting of both LDX and methylene peaks yielded a fitting error of smaller than 10%. The resulting temperature distribution maps under all three temperatures displayed a variation of less than 1°C across the sensitive region of the coil. When two temperature maps were subtracted to calculate relative temperature changes in Figs.6.1(f∼h), the apparent temperature variation across the abdomen of the mouse dropped to less than 0.5°C.

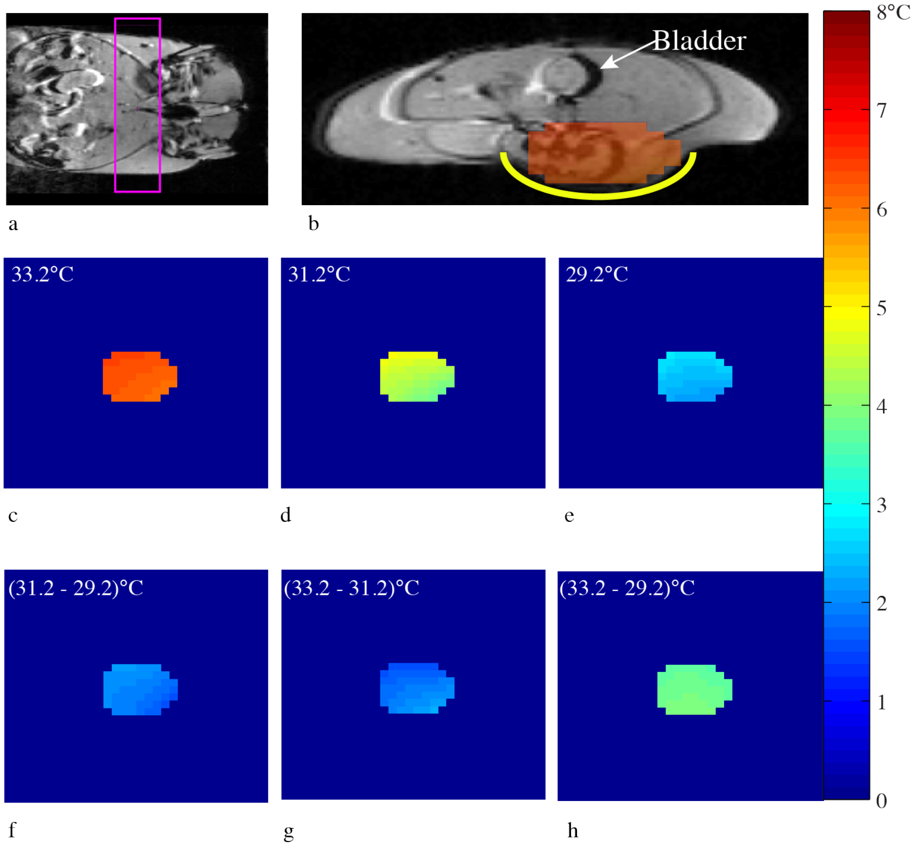

Figure 6.1: *In vivo* temperature maps obtained from an obese mouse using the LDX frequency as temperature sensor. (a) Coronal view showing the selected axial slice. (b) LDX temperature map overlaid on the axial ^{1}H reference image. (c)~(e) LDX temperature maps acquired with the mouse body temperature equilibrated at 3 different temperatures. (f)~(h) Relative temperature change maps showing the correct average temperature change (2°C for f and g, and 4°C for h).

Fig.6.2 shows LDX temperature maps obtained using the methylene frequency as an internal reference on another mouse, the same one as in Fig.3.10, whose body temperature was equilibrated at 31.2°C and 34.2°C. Similar to in the first mouse, the frequency maps of LDX spins across the abdomen presented a frequency variation of about 0.1ppm.

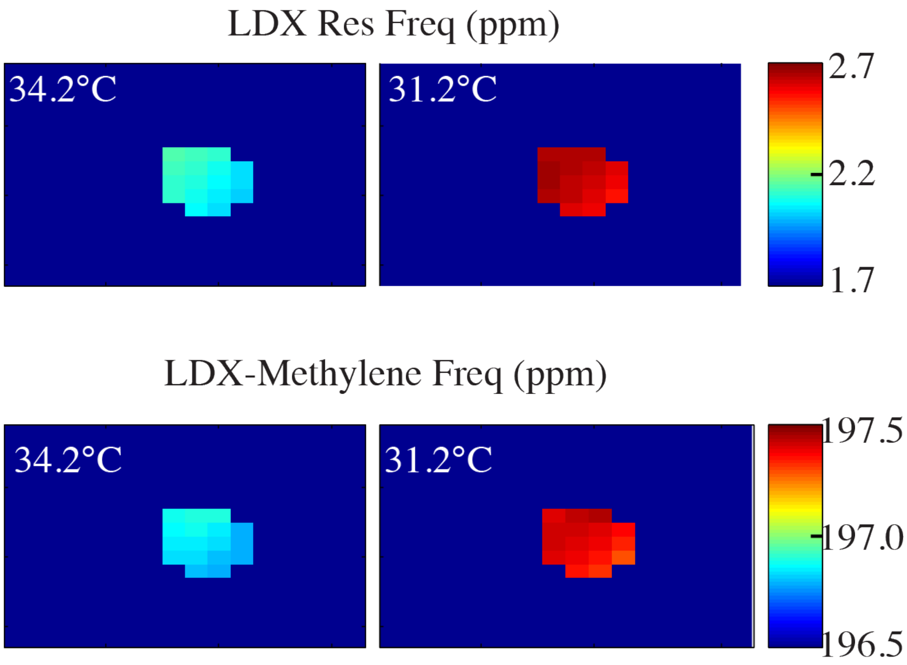

Figure 6.2: LDX and LDX-methylene resonance frequency maps acquired *in vivo* from an obese mouse.

Fig.6.3(a) and (b) show the absolute temperature map calculated at both temperatures, with no pixels deviating from the rectal temperature readings from the mouse of 31.2°C and 34.2°C by more than 0.5°C. Fig.6.3(c) plots the methylene-referenced LDX resonance frequency as a function of rectal temperature as obtained from all *in vivo* studies, along with the values obtained *in vitro* from the rWAT and hWAT samples on the high-resolution spectrometer. Interestingly, the LDX-methylene values obtained *in vivo* match very well with those obtained *in vitro* on rWAT. In all 8 mice analyzed, the big uncertainty in the absolute chemical shift difference between methylene and LDX was rooted in the large uncertainty in the apparent methylene resonance frequency, which was caused by poor methylene line shapes across the mouse abdomen. This was the case whenever the mouse was placed supine on the xenon surface coil such that the sensitive region contained mainly a large water peak and a much weaker and distorted methylene peak.

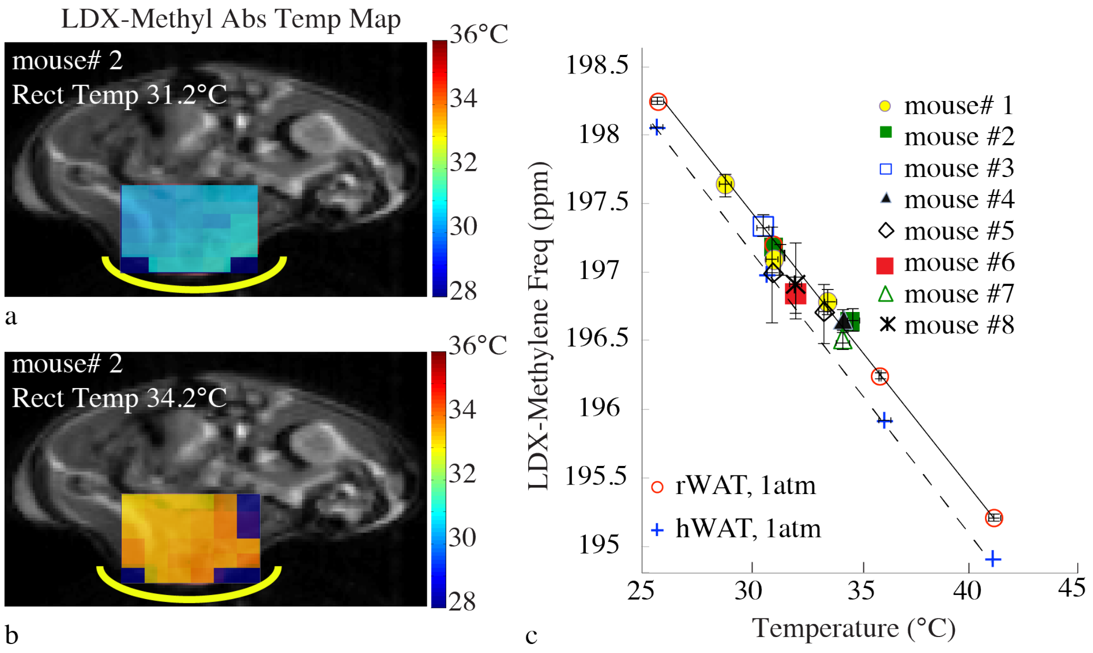

Figure 6.3: (a) and (b) Absolute temperature maps calculated *in vivo* for the same mouse shown in Fig.6.2. (c) Temperature dependence of LDX-methylene resonance frequency obtained from both *in vitro* and *in vivo*.

6.2 *In Vivo* Application of LDX-based Thermometry in Human BAT

While absolute temperature mapping in rodents showed promising results, temperature imaging in distal organs in humans with HP ^{129}Xe is challenging due to the long transfer time of xenon gas from the lung airspaces into tissues. As it has been mentioned before, the relaxation time of HP ^{129}Xe in blood is particularly short, less than 10s. Nevertheless, HP ^{129}Xe has been successfully detected with good SNR in the brain [239] and kidney [240] of humans, where it was demonstrated that dissolved ^{129}Xe signal reached its maximal intensity 10~20s after inhalation. Recently our group has attempted using HP ^{129}Xe to detect brown adipose tissue (BAT) in humans. Characterized by adipocytes that express the mitochondrial uncoupling protein 1 (UCP1) [241], BAT is a functionally distinct type of adipose tissue that is uniquely adapted to transform fat into heat through a process called non-shivering thermogenesis (NST) [207]. NST is the sole mechanism by which mammals regulate their body temperature when exposed to cold environments [242]. Structurally, BAT is highly vascularized and innervated by the sympathetic nervous system. It can be metabolically activated by cold exposure or by a high fat diet. Functionally, BAT has been known to regulate weight gain [243], triglyceride clearance [244] and glucose homeostasis [245]. As such, the pharmacologic expansion and/or activation of BAT can potentially prevent or counteract obesity and type-2 diabetes [246, 247]. In our study, we leverage on both the high fat content of BAT and the increase in blood flow to BAT that occurs during stimulation of thermogenesis [248] to collect high resolution ^{129}Xe images and spectra to measure the temperature of this tissue. The results presented in this section will be submitted for publication [249].

6.2.1 *In Vivo* Temperature Imaging Methods in Humans

This study was approved by the institutional review board of the University of North Carolina at Chapel Hill and was conducted in compliance with the Helsinki Declaration. A total number of six healthy human subjects were recruited and made six visits in total to the facility. All subjects were instructed to fast for 6 hours and refrain from exercise or strenuous activities for 24 hours prior to the imaging sessions. Written consent was obtained from all subjects upon their arrival. After screening, the subject changed into scrub clothes and was brought inside the MRI scanner room, where all scans were conducted on a Siemens Prisma 3T scanner (Siemens AG Medical Solutions, Erlangen, Germany).

The experimental setup is shown in Fig.6.4. The subject lied down on the bed in a supine position. A xenon surface coil was placed on their left shoulder to capture signal from the supraclavicular fat depot, in which BAT is most commonly found in adult humans [250]. To stimulate NST, water-perfused cooling pads (Arctic Sun 2000 Temperature Management System, Medivance, Louisville, CO) were wrapped around the thighs and torso of the subjects. Water temperature was initially set at 30°C, but was later brought down to the point where the subjects started to shiver (typically 10~15°C water temperature). The temperature was subsequently raised by 1°C until shivering subsided. Single voxel ^{1}H spectroscopy (SVS), chemical shift encoded ^{1}H images (CSI) and HP ^{129}Xe single pulse spectroscopy were acquired from the same region of interest, after local optimization of the magnetic field via shimming gradients. Temperature map were generated only for regions that displayed a ^{129}Xe signal with an SNR of greater than 4, and by using the LDX frequency measured from HP ^{129}Xe spectra and the methylene resonance frequency obtained, voxel by voxel, from the CSI map acquired in the same region.

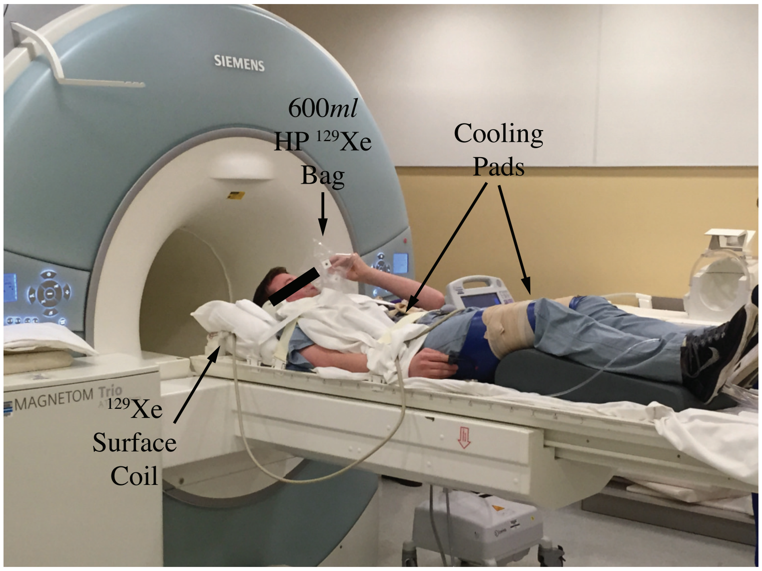

Figure 6.4: Setup of *in vivo* human scans with HP ^{129}Xe.

6.2.2 Results of LDX Thermometry in Human BAT

Fig.6.5 shows example of the LDX spectra and images obtained in one of the subjects after inhalation of HP ^{129}Xe gas. Under warm conditions, only the gaseous peak at 0ppm was observed, suggesting low perfusion and low xenon uptake in BAT at thermoneutrality. However, when the water temperature in the cooling pads was lowered to 1°C above the shivering point, in addition to the gas phase peak, two strong dissolved phase peaks of HP ^{129}Xe were detected: the LDX peak at 195ppm upfield from the gaseous peak, and another peak at 210ppm, assigned to xenon dissolved in plasma. The strong and specific uptake of xenon in BAT located in the supraclavicular fat depot was also observed in gradient-recalled echo image, which shows enhanced xenon signal from the supraclavicular fat region that is known to contain BAT.

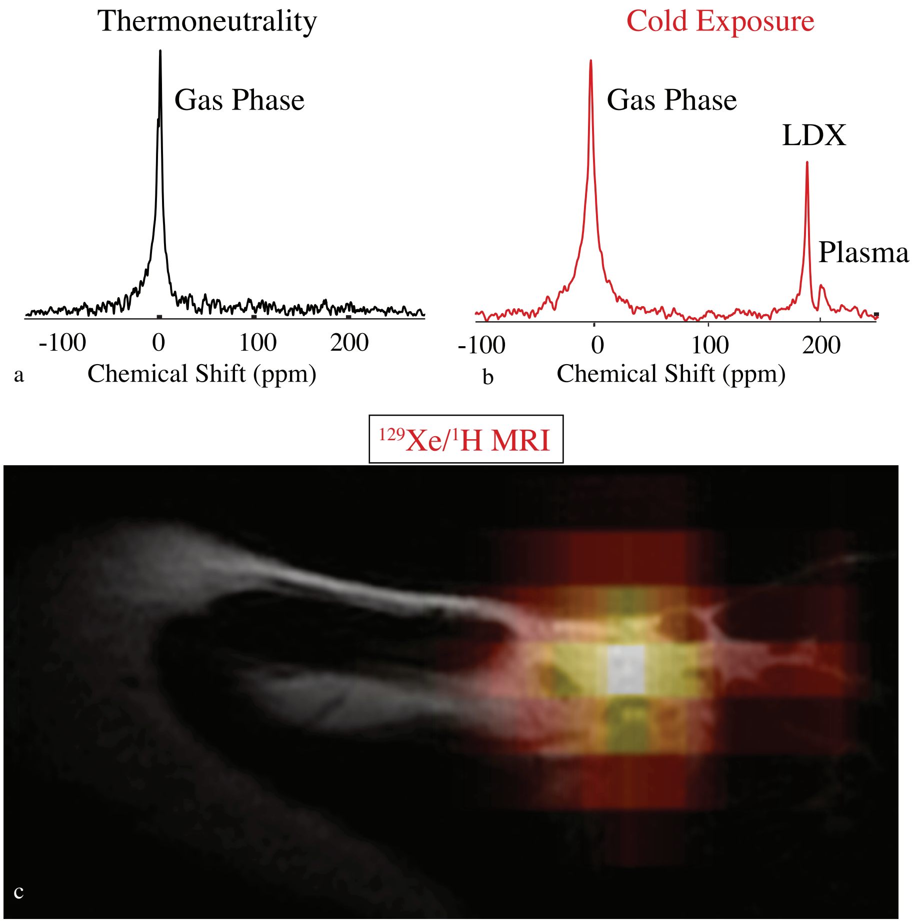
Thermoneutrality
Gas Phase
-100
0
100
200
a
Chemical Shift (ppm)
Cold Exposure
Gas Phase
LDX
Plasma
-100
0
100
200
b
Chemical Shift (ppm)
^{129}Xe/^{1}H MRI
c

Figure 6.5: HP ^{129}Xe spectra obtained in one of the subjects analyzed at thermoneutrality (a) and cold exposure (b). (c) HP LDX image in BAT obtained in the same subject showing intense xenon uptake in the supraclavicular fat region.

Fig.6.6 shows temperature maps obtained from another subject. In this case, temperature maps were acquired at thermoneutrality, during cold exposure, and again at thermoneutrality. By using Equation 5.11 obtained from *in vitro* human fat studies, absolute temperature maps of BAT were calculated. A temperature increase of 2°C was found during cold exposure, while the two temperatures at thermoneutrality were in good agreement with the expected human core body temperature. The slightly elevated temperature measured initially at thermoneutrality could be due to partial activation of BAT induced by stress, which is typical in subject during the first xenon inhalation. However further studies are needed to confirm the 2°C temperature increase in BAT during cold exposure.

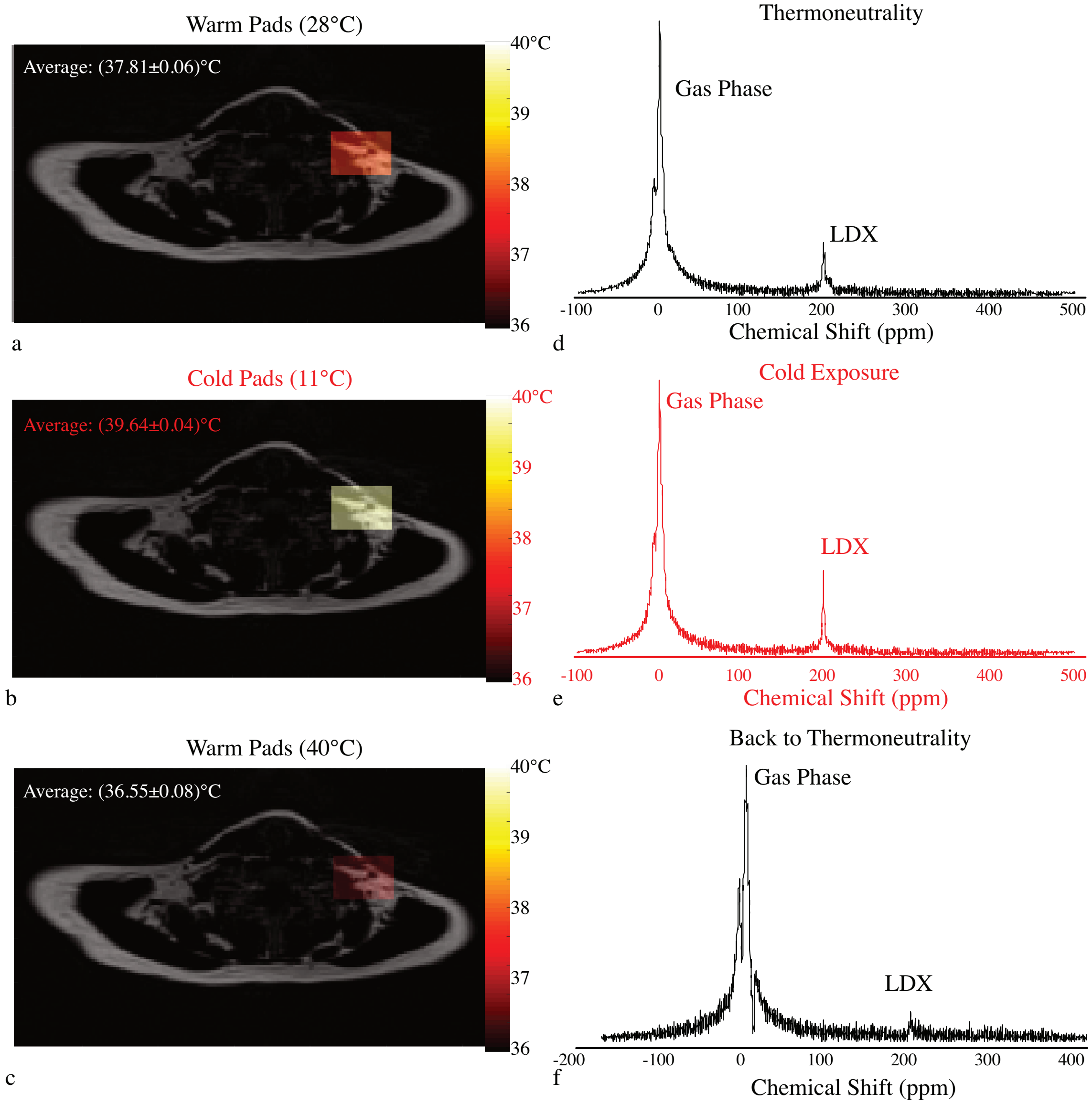

Figure 6.6: Temperature maps calculated using fat-referenced LDX resonance frequency and *in vitro* calibrations at three stages of the study in the second lean subject.

The ^{129}Xe single pulse spectra, though acquired without any spatial selection, also came from the SVS voxel because of the combination of the limited penetration depth characteristic of a surface coil and the aforementioned shimming condition. Spectra in Fig.6.6(d)~(f) differ from those in Fig.6.5 in two ways. The first is that a small dissolved peak was observed at thermoneutrality, which is likely due to the improved localized shimming which was not used in the first subject. The second difference is the existence of only one dissolved peak at ~195ppm upfield from the gaseous peak, even when BAT was activated. The LDX peak also shifted by ~0.5ppm downfield between (d) and (e). A smaller shift downfield was also registered in most pixels of their associated proton CSI spectra. This could be caused by the inadvertent movement by the subject during scans and when they breathed in the gas. Fig.6.7(b) shows the region in which the magnetic field was optimized before the acquisition of ^{1}H and ^{129}Xe spectra, along with the low resolution (12.5*mm*/pixel) HP ^{129}Xe image showing xenon uptake in BAT during cold exposure with an SNR of ~6.

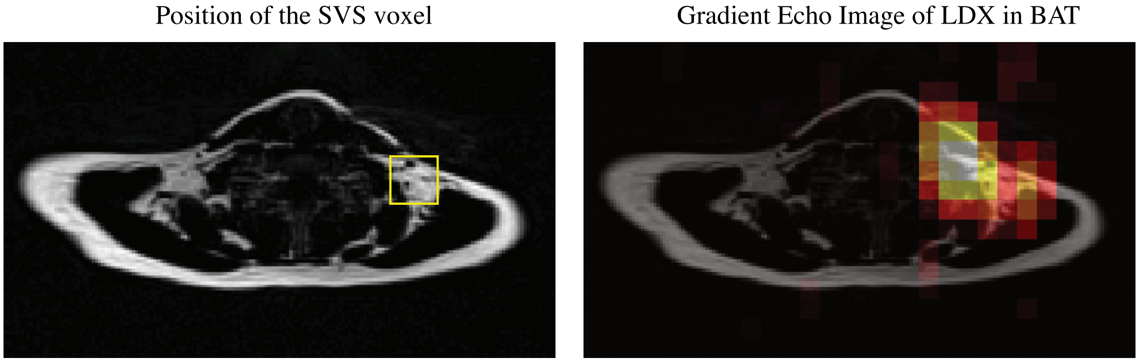

Figure 6.7: (a) The position of the SVS voxel and region of homogeneous B_0 field in the second lean subject. (b) HP LDX image in BAT obtained using gradient echo sequence during cold exposure (after the acquisition of the spectrum in Fig.6.6(e).

6.2.3 Discussion and Conclusions

In this section we have demonstrated the feasibility of *in vivo* absolute LDX-methylene thermometry of BAT in humans. The high solubility of xenon in fat, coupled with the high increase in BAT perfusion during stimulation of BAT thermogenesis, leads to a specific uptake of HP ^{129}Xe in BAT. By combining ^{1}H and HP ^{129}Xe spectroscopic measurements in this tissue, absolute temperature information were obtained. Although future studies are needed to confirm these findings, this represents the first observation of active BAT thermogenesis in humans.

CHAPTER 7: DISTANT DIPOLAR FIELD EFFECT AND ITS APPLICATIONS IN LDX THERMOMETRY

In Chapters 5 and 6 we presented a novel MR thermometry method by using the resonance frequency of lipid-dissolved xenon. We also demonstrated that by referencing the LDX frequency to that of nearby lipid protons, absolute temperature information could be obtained. Nonetheless, this is under the assumption that, for a given imaged voxel or FOV, xenon homogeneously accumulates in the fat compartment from which the methylene resonance frequency is derived. Unfortunately this cannot always be guaranteed *in vivo*, especially if highly vascularized fatty tissues like BAT are mixed with less-vascularized white adipose tissues (WAT). To improve the accuracy of LDX-methylene absolute MR thermometry, we could use the LDX-methylene iMQC signal to detect the resonance frequency difference between LDX and nearby methylene protons.

In this chapter we explore the use of distant dipolar field interactions for xenon spectroscopy and imaging. Specifically we first show how to indirectly detect the resonance frequency of xenon by using that of nearby protons. We then assess the feasibility of LDX-methylene iMQC signal for MR thermometry.

7.1 Remote Detection of ^{129}Xe Using ^{1}H via DDF

In this section I will describe a scheme that utilizes the distant dipolar field effect to indirectly acquire dissolved-phase ^{129}Xe spectrum via direct detection of ^{1}H spectrum. Specifically, a revised sequence was developed based on that proposed in [8], which is designed to detect ^{1}H resonances via ^{129}Xe resonances. In this new sequence, ^{129}Xe spins were detected indirectly via their dipolar field interaction with ^{1}H spins, which served as the sensing spins. Specifically, this new scheme takes advantage of the longer T_1 relaxation time of xenon to create a long-lasting dipolar field with which the fast relaxing ^{1}H spins are allowed to interact many times during a single acquisition. As it will be described below, this new acquisition scheme improves detection sensitivity, but it also presents some challenges. The results presented in this section have been published by our group in [251].

7.1.1 Theory

The sequence originally proposed in [8] and the modified sequence proposed in this dissertation are schematically shown in Fig.7.1(a) and (b), respectively.

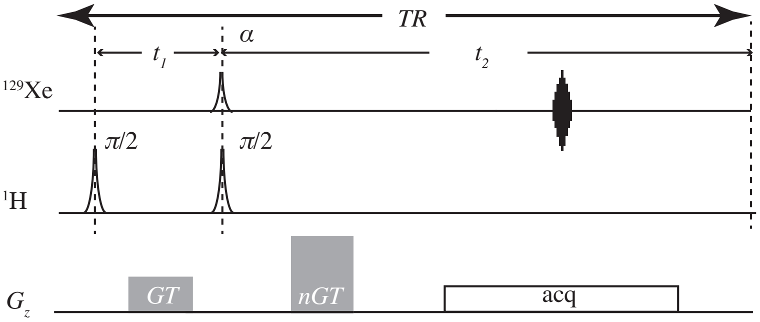

a. Xenon as a sensor

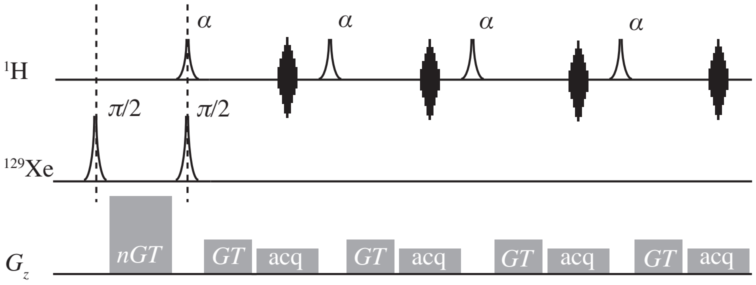

b. Proton as a sensor, multiple acquisitions per TR

Figure 7.1: Indirect detection acquisition scheme. (a) Pulse sequence originally proposed by [8]. (b) Modified sequence developed in this study.

With respect to the original acquisition scheme, the directly and indirectly detected spin species are swapped and a series of ^{1}H excitation pulses and acquisitions follows a single modulation of the longitudinal xenon magnetization. In the new sequence, the first 90° excitation pulse is applied only to the xenon spins, while the second excitation pulse is applied to both proton and xenon spins, with a less than 90° flip angle for the former and a 90° flip angle for the latter. The second RF pulse is placed between two magnetic field gradient pulses, which are used to modulate the longitudinal and transverse magnetization, as well as to select a specific coherence pathway and eliminate any spurious proton signal excited by the second RF pulse.

A very thorough theoretical derivation of the signal originating from DDF interactions has been presented in a number of publications [8, 252, 253]. In this section we will provide only a short description of the spin evolution under the new sequence by using the product operator formalism [254, 255]. For simplicity, the effects of diffusion, T_1 and T_2 relaxation and radiation damping are all ignored. Without the loss of generality, a homogeneous mixture of proton (H) and xenon (S) spins is considered, with ω_H and ω_S being their respective frequency offsets in the rotating frame in absence of field inhomogeneities. For simplicity, all magnetic field gradient pulses are assumed to be applied along the z direction.

Before the first RF pulse, proton spins (H) are considered to be at thermal equilibrium with a magnetization value of H_0, while xenon spins (S) are typically hyperpolarized with a net magnetization of S_0. The first RF pulse $(\pi/2)_y$ rotates the initial xenon magnetization S_0 into the transverse plane. At the end of the first evolution delay t_1 between the two RF pulses, the S_0 magnetization will have evolved under chemical shift and will be dephased by the first correlation gradient $G'T$ such that it will have the following expression:

$$S_{xy} = S_0 \xrightarrow{\omega_S t_1 S_z + G'Tz} S_0 \cos(\omega_S t_1 + \gamma_S G'Tz) + iS_0 \sin(\omega_S t_1 + \gamma_S G'Tz) \tag{7.1}$$

where γ_S is the gyromagnetic ratio of the xenon nucleus.

The second RF pulse $(\pi/2)_y$ will then rotate the x component of the S magnetization in Equation 7.1 to the z axis, while leaving the y component unaffected. As the y component of the magnetization will be subsequently dephased by the second correlation gradient GT, only the z component is retained:

$$S_z = S_0 \cos(\omega_S t_1 + \gamma_S G'Tz) \tag{7.2}$$

At the same time, the H magnetization will be excited and rotated to the transverse plane, for the first time, by the second RF pulse with a flip angle of α: H_X=$H_0 \sin \alpha$. During the second evolution delay t_2, the transverse magnetization of H spins will evolve under the effect of its chemical shift, while being dephased by the second gradient pulse. During this time, the dipolar field generated by the spatially modulated z-magnetization of S spins, $B_d = \mu_0 \frac{2}{3} S_z$, will interact with the transverse H magnetization according to the following equation:

$$\frac{\mathrm{d}H_{XY}}{\mathrm{d}t} = \gamma_H H_{XY} \times (B_0 + G'Tz + \mu_0 \frac{2}{3} S_z) \tag{7.3}$$

where γ_H is the gyromagnetic ratio of the proton nucleus and H_{XY} is the transverse magnetization of H spins.

A solution to Equation 7.3 can be derived by plugging Equation 7.2 in and using a Jacobi-Anger expansion. The condition under which an observable signal can survive is $\gamma_S G' = \gamma_H G$, a condition under which the magnetizations of both S and H spins have the same modulation frequency. When this condition is satisfied, the resulting transverse H magnetization will have the following form:

$$H_{xy} = iH_0 \times \sin(\alpha) \times \mathrm{e}^{i(\Delta\omega_H t_2 - \Delta\omega_s t_1)} J_1(-\frac{2}{3} \gamma_H \mu_0 S_0 t_2) \tag{7.4}$$

where J_1 is the Bessel function of the first kind. Equation 7.4 predicts that the evolution of xenon spins is imprinted in the evolution of the proton signal, which can therefore act as an indirect sensor for xenon spins. Since the longitudinal relaxation time of ^{1}H spins is on the order of few seconds, while the longitudinal relaxation time of xenon is on the order of tens of seconds, multiple ^{1}H excitations and acquisitions can follow a single modulation of the longitudinal xenon magnetization to improve signal to noise ratio.

Following the derivation outlined in [8], while the original detection scheme is expected to give rise to a maximum xenon signal intensity of

$$|S_{\max}| = \frac{\mu_0}{3}\gamma_S^2 B_0 S_0 H_0 T_2^S \sin\alpha \cdot \mathrm{e}^{(-\frac{t_1}{T_2^H}-1)} \tag{7.5a}$$

the new detection scheme is expected to give a maximum proton signal intensity of

$$|H_{\max}| = \frac{\mu_0}{3}\gamma_H^2 B_0 S_0 H_0 T_2^H \sin\alpha \cdot \mathrm{e}^{(-\frac{t_1}{T_2^S}-1)} \tag{7.5b}$$

which gives an increase in sensitivity of:

$$\frac{H_{\max}}{S_{\max}} \approx (\frac{\gamma_H}{\gamma_S})^2 \frac{(\sin\alpha_H)}{(\sin\alpha_{Xe})} \frac{T_2^H}{T_2^S} \tag{7.6}$$

Considering the proportionality of the coil noise to $\gamma_H^{1/4}$ [256], the improvement in SNR ratio between the two sequences is expected to be:

$$\frac{|\mathrm{SNR}_H|}{|\mathrm{SNR}_S|} \propto (\frac{\gamma_H}{\gamma_S})^{7/4} \frac{\sin\alpha_H}{\sin\alpha_{Xe}} \frac{T_2^H}{T_2^S} \tag{7.7}$$

7.1.2 Methods

7.1.2.1 Remote Detection Experimental Setup

Remote detection experiments were carried out on two different samples, one containing pure ethanol and one containing a mixture of 95%-vol. deuterated methanol with 5%-vol. undeuterated methanol. Samples were prepared as shown in Fig.7.2. After solvents were placed in a 5mm medium-walled NMR tube, two strands of polypropylene micro-porous hollow fiber membranes (Celgard, 150μm I.D., Membrana, Charlotte, NC) were connected together at the bottom of the NMR tube by capped polyethylene tubings, which allowed for efficient exchange of gas between the two strands. The other end of one of the strands was left to open air by a polyethylene tubing, while that of the other strand was connected by a polyetheretherketone (PEEK) tubing to the outlet of a homemade ventilator, which pumped polarized xenon into the line once every 30 seconds.

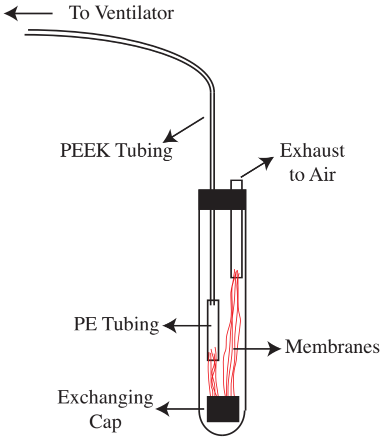

Figure 7.2: Experimental setup for gas exchange in the NMR tube.

Both sequences were implemented on a Varian Inova 500MHz NMR Spectrometer (McKinley Scientific, Sparta, NJ). A direct comparison of the SNR between the HP ^{129}Xe spectrum acquired on the methanol and ethanol samples and a thermally polarized ^{129}Xe spectrum acquired on an oil sample with predetermined dissolved-^{129}Xe concentration allowed us to estimate the HP ^{129}Xe concentration in the two samples to be on the order of a few mmol·L^{-1}.

7.1.2.2 Measurements of T_1 and T_2 Relaxation Times

The T_1 relaxation times of both proton and xenon spins were measured for the two samples using an inversion recovery sequence on thermally polarized samples prepared by dissolving enriched xenon into the solvent. Additionally, the T_2 times of ethanol and methanol protons as well as ethanol-dissolved and methanol-dissolved xenon were measured using a spin echo sequence on the same samples.

7.1.3 Results

7.1.3.1 T_1 and T_2 Results

At 11T, the T_1 time of xenon dissolved in methanol and ethanol was measured to be (18.4±2.5)s and (36.1±3.2)s, respectively. A much shorter longitudinal relaxation time was measured, as expected, for methanol protons (4.9±1.3)s and ethanol protons (3.6±0.8)s. The T_2 time of ethanol protons and of xenon dissolved in ethanol was measured to be (0.581±0.055)s and (1.98±0.08)s, respectively. The T_2 relaxation times of methanol protons and of xenon dissolved in methanol was measured to be (0.119±0.008)s and (1.05±0.09)s, respectively.

According to Equation 7.7 and based on the values measured above, an increase in sensitivity of 2.78 was expected in ethanol by using the new sequence with respect to the original acquisition scheme. A smaller enhancement of 1.85 was expected for methanol. Moreover, considering that with the new sequence four averages are acquired in a single TR, the theoretical improvement given by the new sequence can be estimated to be 5.56 and 3.7 for ethanol and methanol, respectively.

7.1.3.2 Remote Detection in Pure Ethanol

Fig.7.3 shows the 2D spectra acquired using the two sequences in the pure ethanol sample. When xenon is used as a sensor (Fig.7.1(a)), the intensity of the final signal is linearly proportional to the polarization level of the xenon spins. Since each HP xenon gas reservoir was depleted in 16 minutes, the magnetization of xenon varied significantly between different indirect steps. As a result, a T_1 correction was needed to limit t_1 noise in the indirect dimension. This was achieved by multiplying the nth FID by a factor of $\frac{1}{\exp(\frac{30\times n}{T_1\times 60})}$, using a T_1 relaxation time of 38 minutes for xenon gas outside of the magnetic field [257]. Figs.7.3(a), (b), (c) and (d) show, respectively, 2D spectra without t_1 correction, the indirectly detected spectrum derived from Fig.7.3(a), 2D spectra with t_1 correction, and the indirectly detected spectrum derived from Fig.7.3(c). All the figures are normalized to the strongest peak in Fig.7.3(c). By comparing spectra (b) and (d) it became clear that by applying t_1 correction when xenon is used as the sensor the intensity of all three ethanol peaks increased by 10~15%.

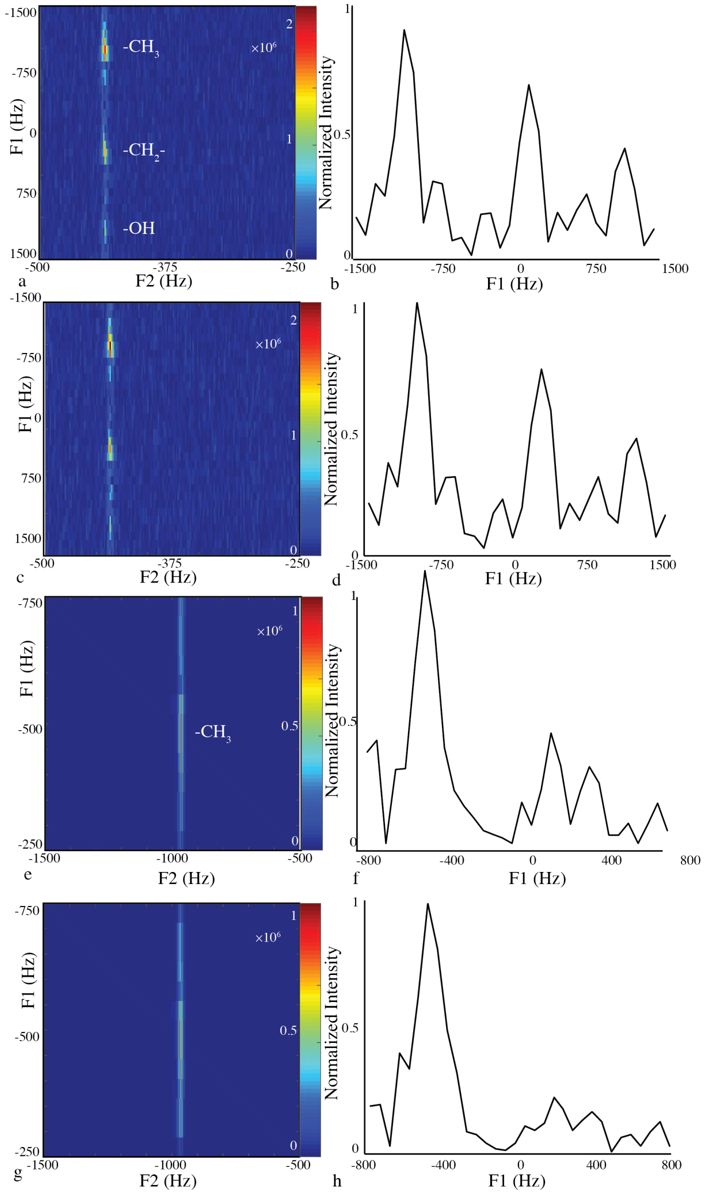

Figure 7.3: 2D spectra acquired on the pure ethanol membrane sample. (a): 2D spectrum using xenon as the sensor without t_1 correction. (b): F1-projection of the 2D spectrum (a), which is normalized to the maximal intensity of spectrum (d). (c): 2D spectrum using xenon as the sensor with t_1 correction. (d): F1-projection of the 2D spectrum (c). (e): 2D spectrum using proton as the sensor without t_1 correction. (f): F1-projection of the 2D spectrum (e), which is normalized to the maximal intensity of spectrum (h). (g): 2D spectrum using xenon as the sensor with t_1 correction. (h): F1-Projection of 2D spectrum (g).

However, when ^{1}H spins are used as sensor (Fig.7.1(b)), the correction for gas depolarization cannot be easily applied. As shown in Eqn. 7.4, for the second acquisition scheme in which ^{1}H is the sensor, the magnetization of xenon spins is not simply related to the signal intensity, but it is related to the dipolar demagnetization time $\tau_d = \frac{1}{\gamma_H \mu_0 S_0}$, which directly affects the signal refocusing time. Indeed, by comparing the indirectly detected spectrum before t_1 correction shown in Fig.7.3(f) to that after t_1 correction shown in Fig.7.3(h), one can conclude that the correction has actually decreased the intensity of the dissolved xenon peak by about 9%. Figs.7.3(d) and (h) also show, respectively, the indirectly detected ethanol spectrum, with all three main peaks visible and the indirectly detected xenon spectrum, where the prominent ethanol-dissolved xenon peak dominates. Fig.7.3 clearly indicates that radiation damping in a highly protonated sample is the main issue when ^{1}H is used as a sensor, leading to turbulent spin dynamics [258]. As a result, sequence shown in Fig.7.1(b) in this case did not lead to an improvement in SNR compared to sequence shown in Fig.7.1(a). However, in spite of the presence of radiation damping, which considerably broadened the resonance frequency lines, the indirectly detected ^{129}Xe frequency was still observable.

7.1.3.3 Remote Detection in Mixed Deuterated/undeuterated Methanol

2D spectra acquired using sequences shown in 7.1 and their associated indirectly detected spectra are shown in Fig.7.4, which are all normalized to the intensity of the strongest peak in (c). Fig.7.4(a) has been corrected for the T_1 relaxation of xenon gas as described above, which again improved the dissolved xenon-methyl group cross peak intensity by 18%. In Fig.7.4(b), the indirect spectrum of methanol is shown, with both methyl and hydroxyl groups clearly visible. In Fig.7.4(d), the F1 projection shows the dissolved-phase xenon peak. By comparing Figs.7.4(b) and (d), a clear improvement in the intensity of the signal between dissolved xenon and the methyl group is seen when sequence in Fig.7.1(a) is replaced by sequence (b), which amounts to about 18%. Additionally, the indirectly detected dissolved xenon peak also showed a reduced peak width (~200Hz compared to ~300Hz in (d)).

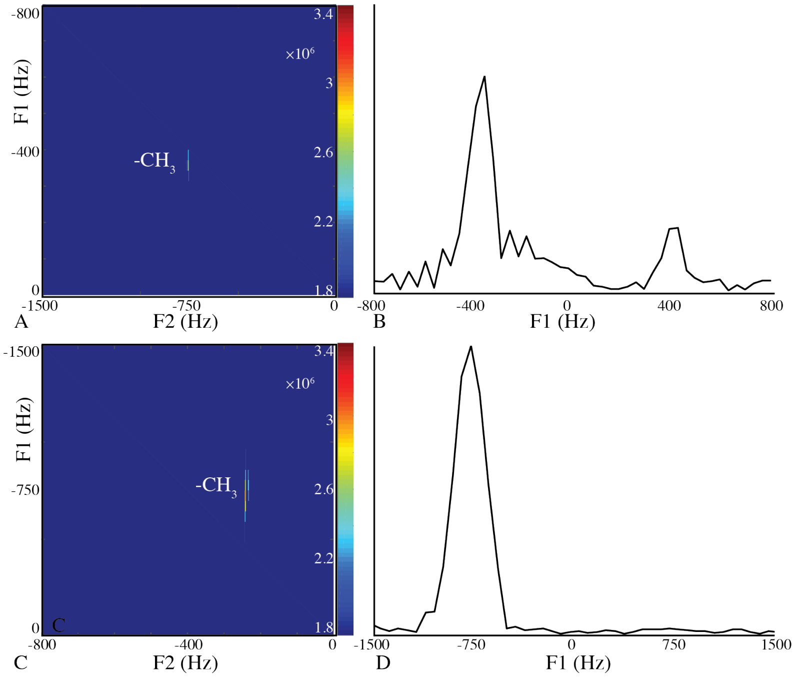

Figure 7.4: 2D spectra acquired on the mixed deuterated/undeuterated methanol sample. (a): 2D spectrum using xenon as the sensor with t_1 correction. (b): Projection of spectrum (a) onto the indirectly detected dimension. (c): 2D spectrum using proton as the sensor with t_1 correction. (d): Projection of spectrum (b) onto the indirectly detected dimension.

7.1.4 Discussions

In this section, we presented a new acquisition scheme for the indirect detection of ^{129}Xe resonances via the direct detection of ^{1}H resonances. The new acquisition scheme leverages on the much longer longitudinal relaxation time of dissolved ^{129}Xe spins to create a long-lasting dipolar field with which the fast relaxing ^{1}H spins are allowed to interact many times.

The new acquisition scheme, when compared to the original one proposed in [8], gives an experimental improvement of maximal signal intensity to noise ratio in the 2D spectrum of 3.2, for the methanol sample, only slightly smaller than the predicted enhancement of 3.7. This discrepancy is most likely due to the assumption of the absence of magnetic field inhomogeneities, which would lead to a $(\frac{\gamma_H}{\gamma_S})^{7/4}\frac{T_2^{*H}}{T_2^{*S}}$ dependence rather than a $(\frac{\gamma_H}{\gamma_S})^{7/4}\frac{T_2^{H}}{T_2^{S}}$ of the signal enhancement. Moreover, the assumption that the modulated longitudinal ^{129}Xe polarization remain identical during the acquisition train and that the maximal signal to noise ratio is boosted by a factor of 2 when the result of the 4 acquisition windows is added together is not accurate either. For the ethanol sample, the apparent enhancement is even higher, of 100 fold. However, in this case, the presence of radiation damping in the spectrum makes this measurement unreliable.

Despite the increased sensitivity when ^{1}H is used as a sensor, this approach presents several new challenges with respect to the original sequence that uses ^{129}Xe as sensor. The most important issue is the low spin density of dissolved xenon, which we estimated to be on the order of few *m*M or less, creating a substantially weaker dipolar field and, ultimately, leading to a long dipolar demagnetization time during which the proton magnetization rapidly dephases under the effect of magnetic field inhomogeneities. This means that in solutions where xenon does not dissolve in a relatively high amount to generate a strong magnetization density or in solutions in which the longitudinal relaxation time of xenon is too short, there may not be any sensitivity improvement. Moreover, since the diffusion coefficient of dissolved xenon atoms is larger than that of water molecules, long correlation distances need to be used in order to prevent serious "scrambling" of the modulation of the ^{129}Xe magnetization by diffusion. This means that this approach is not really feasible when ^{1}H spins are used to sense the xenon gaseous phase. However, it is hard to imagine a situation in which one would want to do that.

It is also worth noting that the improvement in maximal SNR in the 2D spectrum provided by the new approach comes with a penalty of a longer acquisition time. Because of the very long T_1 of dissolved ^{129}Xe, sequence in Fig.7.1(b) requires the use of a very long TR to avoid unwanted excitation of the already modulated longitudinal xenon magnetization. Another issue with this approach may arise from the high magnetization density of ^{1}H at high field, which leads to the observation of radiation damping effects. In these cases, radiation damping will have to be suppressed by using partially deuterated samples as well as by de-tuning the proton channel. Nonetheless this study demonstrates that, although radiation damping can produce considerable noise in the 2D spectrum and broaden the resonance frequency lines, it will not hamper the observation of the indirectly detected xenon spins.

In summary, in this section we have proposed a modification of the previously proposed scheme for indirect detection of ^{129}Xe frequencies via dipolar field interaction with ^{1}H spins. This method takes advantage of the long spin-lattice relaxation time of dissolved xenon and the high gyromagnetic ratio of protons to generate a long-lasting dipolar field with which ^{1}H spins are allowed to interact many times. The results showed a 3.2 times improvement in maximal SNR in the 2D spectrum when compared to the original sequence.

7.2 LDX-methylene iZQC MR Thermometry

As it has been demonstrated in Chapter 4, iZQC sequence could provide a direct measurement of the resonance frequency difference between the correlated spins at the microscopic scale. However it was also pointed out that, in order for this frequency to be insensitive to the effect of microscopic susceptibility gradients, the correlated spins had to mix at the microscopic level. Lipid dissolved xenon spins and methylene protons do mix at the microscopic level. More importantly, as we have shown in the previous chapters, the chemical shift of LDX has a very strong temperature dependence. However, because ^{129}Xe and ^{1}H spins have different levels of sensitivities to the field inhomogeneities due to their different gyromagnetic ratios, the use of LDX-methylene iZQC frequency ω_{LDX}-ω_{Fat} will not allow for a complete removal of magnetic field inhomogeneities. In order to completely remove the effect of magnetic field inhomogeneities at the microscopic level, a sequence has to be devised in which the iMQC signal evolves with a frequency of ω_{LDX}-$\frac{\gamma_{Xe}}{\gamma_H}\omega_{Fat}$. In the next sections we will describe such sequence and its implementation for MR thermometry.

7.2.1 Heteronuclear iZQC Sequence

Experiments on heteronuclear mixed spin systems were performed by using the sequences in Fig.7.5. Sequence in Fig.7.5(a) is the classic heteronuclear CRAZED sequence, in which the iZQC signal evolves during t_1 with a frequency of $\omega_I - \omega_S$. Since the two spins have different gyromagnetic ratios, this sequence is not expected to completely remove the effect of magnetic field inhomogeneities and therefore, a dependence of the iZQC frequency on the correlation distance is expected in presence of magnetic field inhomogeneities.

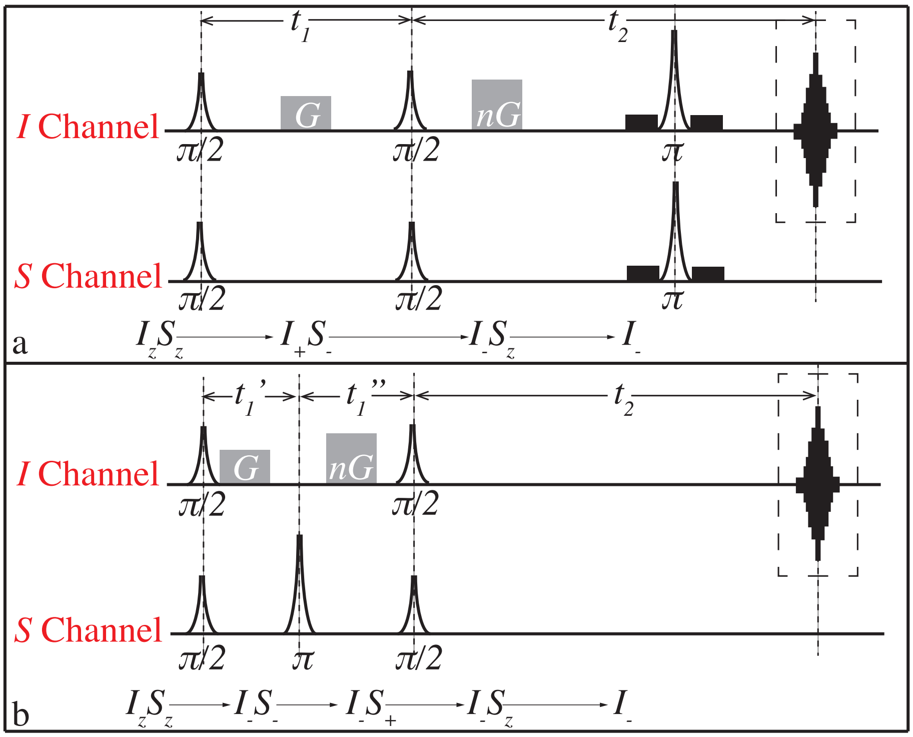

t_1
t_2
I Channel
G
nG
π/2
π/2
π
S Channel
π/2
π/2
π
a
$I_z S_z \rightarrow I_+ S_- \rightarrow I_- S_z \rightarrow I_-$
t_1'
t_1''
t_2
I Channel
G
nG
π/2
π/2
S Channel
π/2
π
π/2
b
$I_z S_z \rightarrow I_- S_- \rightarrow I_- S_+ \rightarrow I_- S_z \rightarrow I_-$

Figure 7.5: Heteronuclear iZQC sequence used in this study. (a) Heteronuclear iZQC sequence. (b) Modified version of the inhomogeneity-free iDQC/iZQC sequence proposed in [9].

Sequence in Fig.7.5(b) is a modified version of the inhomogeneity-free heteronuclear sequence originally proposed in [9] to account for the high diffusivity of xenon spins in oil and fatty tissues [259] and short T_1 relaxation time of fat spins. Specifically, the refocusing module in the original sequence is removed, as is one of the 180° inversion pulses, to minimize signal loss. One of the gradients is also moved to an earlier time point in the sequence to sandwich the remaining 180° inversion pulse to further curb the impact of diffusion. The selected coherence pathway is listed in the bottom of Fig.7.5(b). In the sequence, iDQCs are excited by the first 90° pulse. These coherences are then transferred into iZQCs, which evolve during t_1''. iZQCs are finally converted into iSQCs by the last 90° pulse, which are lastly refocused by the distant dipolar field. The indirect evolution delays t_1' and t_1'' are simultaneously incremented such that the signal effectively evolves in the indirect dimension at a frequency of $\omega_I - \frac{\gamma_I}{\gamma_S}\omega_S$, thus removing the effect of microscopic susceptibility gradients.

To provide a brief analysis of Sequence (b) which selects both double quantum (iDQC) and zero quantum coherences (iZQC), we can again adopt the formalism of product operators. The first set of 90° RF pulses acts on both channels and excites both spin species onto the transverse plane, creating zero as well as double quantum coherences:

$$I_z S_z \xrightarrow{90^\circ_x} \{I_+ S_- + I_- S_+\}_{ZQC} + \{I_+ S_+ + I_- S_-\}_{DQC}. \tag{7.8}$$

During the delay t_1', these operators will evolve under the effect of chemical shift and will also be dephased by the z-gradients such as, at the end of this delay, they will have individually acquired a phase of:

$$\begin{aligned}
&\{I_+ S_- + I_- S_+\}_{ZQC} + \{I_+ S_+ + I_- S_-\}_{DQC} \xrightarrow{t_1'} \\
&\{I_+ S_- \mathrm{e}^{i[-(\omega_I - \omega_S)t_1' - \gamma_I G T z_I + \gamma_S G T z_S]} + I_- S_+ \mathrm{e}^{i[(\omega_I - \omega_S)t_1' + \gamma_I G T z_I - \gamma_S G T z_S]}\}_{ZQC} \\
&\{I_+ S_+ \mathrm{e}^{i[-(\omega_I + \omega_S)t_1' - \gamma_I G T z_I - \gamma_S G T z_S]} + I_- S_- \mathrm{e}^{i[(\omega_I + \omega_S)t_1' + \gamma_I G T z_I + \gamma_S G T z_S]}\}_{DQC},
\end{aligned} \tag{7.9}$$

with z_I and z_S being the z-coordinate of the I and S spins, respectively. The second 180° pulse will invert only the S spins, and the double quantum coherences will be transformed into zero quantum coherences and *vice versa*:

$$\begin{gathered}
\{I_+S_-\mathrm{e}^{i[-(\omega_I-\omega_S)t_1'-\gamma_I GTz_I+\gamma_S GTz_S]}+I_-S_+\mathrm{e}^{i[(\omega_I-\omega_S)t_1'+\gamma_I GTz_I-\gamma_S GTz_S]}\}_{ZQC}\\
\{I_+S_+\mathrm{e}^{i[-(\omega_I+\omega_S)t_1'-\gamma_I GTz_I-\gamma_S GTz_S]}+I_-S_-\mathrm{e}^{i[(\omega_I+\omega_S)t_1'+\gamma_I GTz_I+\gamma_S GTz_S]}\}_{DQC}\xrightarrow{180^\circ_y}\\
\{I_+S_+\mathrm{e}^{i[-(\omega_I-\omega_S)t_1'-\gamma_I GTz_I+\gamma_S GTz_S]}+I_-S_-\mathrm{e}^{i[(\omega_I-\omega_S)t_1'+\gamma_I GTz_I-\gamma_S GTz_S]}\}_{ZQC\to DQC}\\
\{I_+S_-\mathrm{e}^{i[-(\omega_I+\omega_S)t_1'-\gamma_I GTz_I-\gamma_S GTz_S]}+I_-S_+\mathrm{e}^{i[(\omega_I+\omega_S)t_1'+\gamma_I GTz_I+\gamma_S GTz_S]}\}_{DQC\to ZQC}.
\end{gathered}\tag{7.10}$$

During the delay t_1'', the products will then be further dephased by the second gradient pulse, while evolving under chemical shift. At the conclusion of the delay, Expression 7.10 will have become:

$$\begin{gathered}
\{I_+S_+\mathrm{e}^{i[-(\omega_I-\omega_S)t_1'-\gamma_I GTz_I+\gamma_S GTz_S]}+I_-S_-\mathrm{e}^{i[(\omega_I-\omega_S)t_1'+\gamma_I GTz_I-\gamma_S GTz_S]}\}_{ZQC\to DQC}\\
\{I_+S_-\mathrm{e}^{i[-(\omega_I+\omega_S)t_1'-\gamma_I GTz_I-\gamma_S GTz_S]}+I_-S_+\mathrm{e}^{i[(\omega_I+\omega_S)t_1'+\gamma_I GTz_I+\gamma_S GTz_S]}\}_{DQC\to ZQC}\xrightarrow{t_1''}\\
\{I_+S_+\mathrm{e}^{i[-(\omega_I-\omega_S)t_1'-\gamma_I GTz_I+\gamma_S GTz_S]}\mathrm{e}^{i[-(\omega_I+\omega_S)t_1''-\gamma_I nGTz_I-\gamma_S nGTz_S]}+\\
I_-S_-\mathrm{e}^{i[(\omega_I-\omega_S)t_1'+\gamma_I GTz_I-\gamma_S GTz_S]}\mathrm{e}^{i[(\omega_I+\omega_S)t_1''+\gamma_I nGTz_I+\gamma_S nGTz_S]}\}_{ZQC\to DQC}\\
\{I_+S_-\mathrm{e}^{i[-(\omega_I+\omega_S)t_1'-\gamma_I GTz_I-\gamma_S GTz_S]}\mathrm{e}^{i[-(\omega_I-\omega_S)t_1''-\gamma_I nGTz_I+\gamma_S nGTz_S]}+\\
I_-S_+\mathrm{e}^{i[(\omega_I+\omega_S)t_1'+\gamma_I GTz_I+\gamma_S GTz_S]}\mathrm{e}^{i[(\omega_I-\omega_S)t_1''+\gamma_I nGTz_I-\gamma_S nGTz_S]}\}_{DQC\to ZQC}.
\end{gathered}\tag{7.11}$$

The third and final 90° pulse is applied onto both types of spins. As the receiver in Fig.7.5(b) is tuned to detect signal from I spin, we will only focus on the product operators that have S spins converted back to the z-axis and I spins on the transverse plane. Moreover, assuming the detection of coherences with a quantum coherence number of -1, another restraint is applied that only terms that have I_- is retained. These two conditions combine to give:

$$
\begin{aligned}
&\{I_+S_+\mathrm{e}^{i[-(\omega_I-\omega_S)t_1'-\gamma_I GTz_I+\gamma_S GTz_S]}\mathrm{e}^{i[-(\omega_I+\omega_S)t_1''-\gamma_I nGTz_I-\gamma_S nGTz_S]}+\\
&\quad I_-S_-\mathrm{e}^{i[(\omega_I-\omega_S)t_1'+\gamma_I GTz_I-\gamma_S GTz_S]}\mathrm{e}^{i[(\omega_I+\omega_S)t_1''+\gamma_I nGTz_I+\gamma_S nGTz_S]}\}_{ZQC\rightarrow DQC}\\
&\{\underline{I_+S_-\mathrm{e}^{i[-(\omega_I+\omega_S)t_1'-\gamma_I GTz_I-\gamma_S GTz_S]}\mathrm{e}^{i[-(\omega_I-\omega_S)t_1''-\gamma_I nGTz_I+\gamma_S nGTz_S]}}+\\
&\quad I_-S_+\mathrm{e}^{i[(\omega_I+\omega_S)t_1'+\gamma_I GTz_I+\gamma_S GTz_S]}\mathrm{e}^{i[(\omega_I-\omega_S)t_1''+\gamma_I nGTz_I-\gamma_S nGTz_S]}\}_{DQC\rightarrow ZQC}\xrightarrow[only\ surviving\ operators]{90^\circ_y}\\
&\{I_-S_z\mathrm{e}^{i[-(\omega_I-\omega_S)t_1'-\gamma_I GTz_I+\gamma_S GTz_S]}\mathrm{e}^{i[-(\omega_I+\omega_S)t_1''-\gamma_I nGTz_I-\gamma_S nGTz_S]}+\\
&\quad I_-S_z\mathrm{e}^{i[(\omega_I-\omega_S)t_1'+\gamma_I GTz_I-\gamma_S GTz_S]}\mathrm{e}^{i[(\omega_I+\omega_S)t_1''+\gamma_I nGTz_I+\gamma_S nGTz_S]}\}_{ZQC\rightarrow DQC\rightarrow SQC}\\
&\{\underline{I_-S_z\mathrm{e}^{i[-(\omega_I+\omega_S)t_1'-\gamma_I GTz_I-\gamma_S GTz_S]}\mathrm{e}^{i[-(\omega_I-\omega_S)t_1''-\gamma_I nGTz_I+\gamma_S nGTz_S]}}+\\
&\quad I_-S_z\mathrm{e}^{i[(\omega_I+\omega_S)t_1'+\gamma_I GTz_I+\gamma_S GTz_S]}\mathrm{e}^{i[(\omega_I-\omega_S)t_1''+\gamma_I nGTz_I-\gamma_S nGTz_S]}\}_{DQC\rightarrow ZQC\rightarrow SQC}.
\end{aligned}
\tag{7.12}
$$

During the delay t_2, the signal is refocused by the long-range dipolar coupling with the operator S_z stripped to yield a detectable signal, by virtue of Equation 4.7. With the difference of spatial location of both spins in z_I and z_S ignored, we can design a coherence pathway filter with the two gradient pulses such that the condition $(\gamma_I + \gamma_S)GTz + (\gamma_I - \gamma_S)nGTz = 0$ is satisfied, which requires that $n = \frac{\gamma_S+\gamma_I}{\gamma_S-\gamma_I}$. Under this condition, only the last two terms on the left hand side of Expression 7.12 will survive the coherence pathway filter. However, during delay t_2, the product operator will continue acquiring positive phase under the chemical shift of I_- operator. This means that only the third term, highlighted in Expression 7.12 by underline which has accumulated negative phase under the chemical shift during the previous delays, will be refocused when the condition $\mathrm{e}^{-i(\omega_I+\omega_S)t_1}\mathrm{e}^{-i(\omega_I-\omega_S)t_1''}\mathrm{e}^{i\omega_I t_2} = 1$ is satisfied, *i.e.* $t_2 = (1 + \frac{\omega_S}{\omega_I})t_1' + (1 - \frac{\omega_S}{\omega_I})t_1''$.

Under less ideal conditions, if z_I and z_S are different with $|z_I - z_S| \approx 10\mu m$, an extra phase of $(\gamma_I z_I + \gamma_S z_S + n\gamma_I z_I - n\gamma_S z_S)GT = \frac{2\gamma_I\gamma_S GT|z_I-z_S|}{\gamma_S-\gamma_I} \approx 10^{-1}$ will be introduced when the correlation distance is set at $d_c = \pi/\gamma_I GT$=100μm, which can be safely ignored. By stepping delays t_1' and t_1''

such that $\Delta t_1'' = \frac{\gamma_S+\gamma_I}{\gamma_S-\gamma_I}\Delta t_1'$, the signal will effectively evolve in the indirect dimension with a frequency of $\frac{(\omega_I+\omega_S)\Delta t_1'+(\omega_I-\omega_S)\Delta t_1''}{\Delta t_1'+\Delta t_1''} = \frac{(\omega_I+\omega_S)\Delta t_1'+(\omega_I-\omega_S)\frac{\gamma_S+\gamma_I}{\gamma_S-\gamma_I}\Delta t_1'}{\Delta t_1'+\frac{\gamma_S+\gamma_I}{\gamma_S-\gamma_I}\Delta t_1'} = \omega_I - \frac{\gamma_I}{\gamma_S}\omega_S$, whose spectra width is given by $SW = \frac{1}{\Delta t_1'+\Delta t_1''}$.

7.2.2 Methods

All spectroscopic studies were performed on a Varian Inova 500MHz NMR spectrometer (Varian NMR Systems, Palo Alto, CA) using a ^{1}H-^{19}F/^{15}N-^{31}P switchable broadband probe. The WAT/Muscle sample in Chapter 4 was used in this study. In order to detect LDX-methylene iDQC/iZQC signals using thermally polarized LDX spins, xenon had to be dissolved in the sample at high concentration. For this purpose, the WAT/muscle tissue was placed into a specially made high-pressure zirconium NMR tube, 3.4*mm* inner diameter with a total volume of 0.95*ml* (Daedalus Innovations, Aston, PA), rated to work continuously under 1 kbar. The tube was then submerged into liquid nitrogen and evacuated. A 200*ml* Tedlar bag filled with enriched xenon gas (86% ^{129}Xe) was attached to the NMR tube while in liquid nitrogen until the bag was completely deflated as xenon froze out in the NMR tube. The tube was then sealed and stored at room temperature for at least 24 hours to allow xenon to dissolve into the sample. All scans were performed within two days to minimize chances of the sample separation and degradation. Similar experiments could not be made on the emulsion samples as the structure of the emulsion was destroyed during the freeze-thaw cycle needed to dissolve large quantities of xenon in the samples. To compare the line-narrowing effects of the two sequences in Fig.7.5, experiments were also performed on a sample of pure phosphoric acids where both ^{1}H-^{31}P iZQC and ^{1}H-^{31}P iDQC/iZQC spectra were collected. To select the coherence pathway specified in Fig.7.5, n was set to 1.47 for the former and 2.36 for the latter.

7.2.3 Results

Fig.7.6 shows examples of the LDX-methylene iDQC/iZQC spectra acquired on the WAT/muscle sample by selecting a correlation distance of $100\mu m$. The 2D spectrum shows a prominent peak at (F1,F2)=(ω_{Xe}-$\frac{\gamma_{Xe}}{\gamma_H}\omega_f$, ω_{Xe}). Contaminations can be seen at several other locations but their intensities are less than 20% of the main peak and are thresholded out in the spectrum. Thanks to the large temperature coefficient of LDX, the shift of the LDX-methylene iDQC/iZQC peak with temperature can be clearly observed. The LDX-methylene iDQC/iZQC frequency was (2.048±0.019)ppm, (-0.018±0.017)ppm, (-2.370±0.020)ppm and (-3.904±0.022)ppm at 25.7°C, 32.8°C, 40.0°C and 46.0°C, respectively.

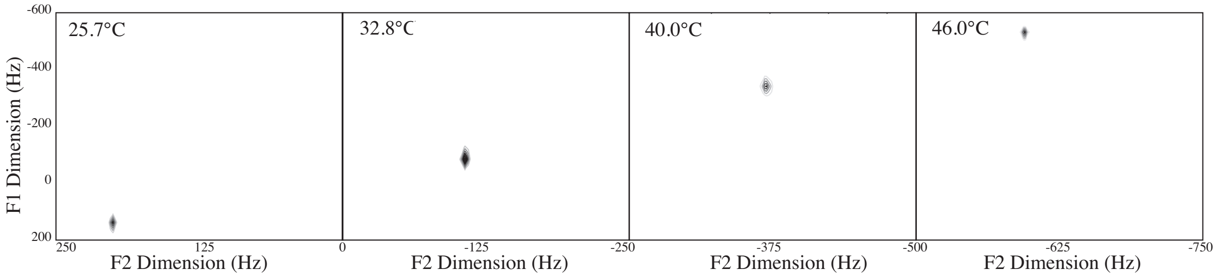

Figure 7.6: 2D spectra acquired on the WAT/Muscle sample at four temperatures showing the LDX-methylene iDQC/iZQC cross peak.

The LDX-methylene iDQC/iZQC frequency and its temperature dependence in the WAT/Muscle sample is reported in Fig.7.7. LDX-methylene resonance frequency differences as measured by 1D spectroscopic method is also reported in the figure. Compared with experimental results on water-fat iZQC frequency in Fig.4.8, the LDX-methylene temperature curves demonstrated a slightly better linearity, reflected in the R^2 value of ≥0.997. The temperature coefficient and the y-intercept, on the other hand, showed great consistency among different correlation distances, averaging to (-0.288±0.002)ppm/°C and (8.29±0.29)ppm, respectively. Moreover, the LDX-methylene frequency separation, as calculated from 1D spectra in ppm with respect to their relative center frequencies, nicely matched the LDX-methylene iDQC/iZQC resonance frequency.

Neither was variation seen in the LDX-methylene resonance frequency with respect to the correlation distance. This underlines how, for mixed heteronuclear spin systems, the choice of the correlation distance has no effect on their iDQC/iZQC resonance frequency.

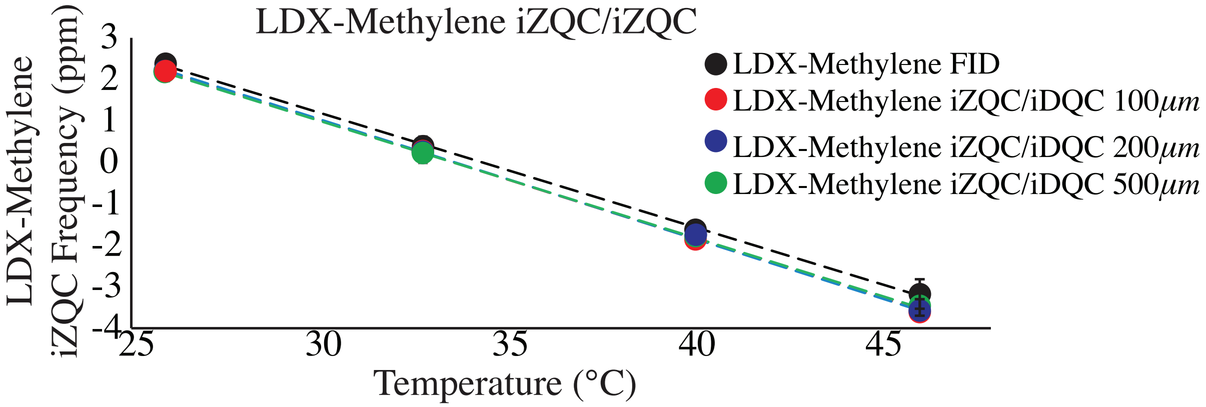

Figure 7.7: Dependence on correlation distance and temperature of the LDX-methylene iZQC/iDQC frequency.

Similar results were obtained from the phosphoric acid sample which are shown in Fig.7.8. As expected, the ^{1}H-^{31}P iZQC signal was unable to completely remove the effect of magnetic field inhomogeneities and a significant change of the ^{1}H-^{31}P iZQC frequency was observed as a function of the correlation distance in (a). A dependence of the peak linewidth on shimming conditions and correlation distance was also found. On the contrary, the iDQC/iZQC signal was capable of completely removing the effect of magnetic field inhomogeneities, as already pointed out in [9], and no variation of the ^{1}H-^{31}P iDQC/iZQC resonance frequency nor its linewidth was observed as function of the correlation distance in (c) and (d).

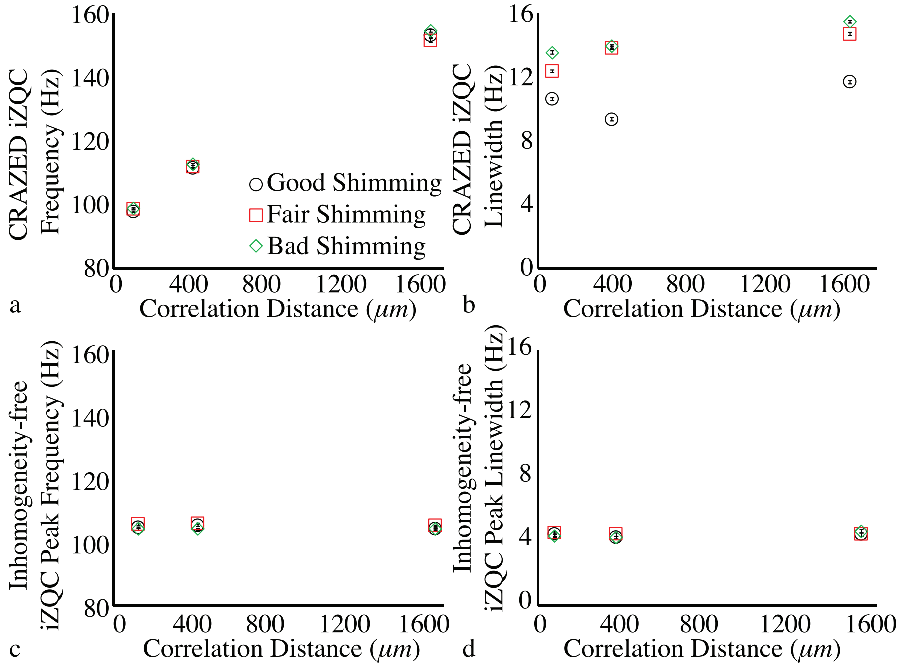

Figure 7.8: ^{1}H-^{31}P iZQC and iDQC/iZQC resonance frequencies (a&c) and linewidths (b&d) as measured for phosphoric acid as a function of the correlation distance.

7.2.4 Discussion

7.2.4.1 Accuracy of LDX iZQC/iDQC methods

Unlike the variability exhibited by the water-fat iZQC resonance frequency and by its temperature coefficient in Chapter 4, the heteronuclear iZQC/iDQC frequency in samples where spins mix at the molecular level or are in the same molecule is expected to deliver on the promise of completely removing the effect of macro and microscopic magnetic field gradients on the resonance frequencies. This is the case, for example, for ^{1}H and ^{31}P spins in phosphoric acids and LDX and methylene protons in fatty tissues. In these cases, however, because the correlated spins have different gyromagnetic ratios, the effect can be completely removed only if the iMQC signal is made to evolve in the indirect dimension at a frequency of $\omega_{Xe} - \frac{\gamma_{Xe}}{\gamma_H} \times \omega_H$. This possibly opens the door to absolute MR temperature measurements when temperature independent and temperature dependent spins that mix at the microscopic level can be found, as it is the case for methylene protons and LDX spins, assuming that the dependence on lipid composition of the LDX frequency is negligible, which will be a topic of investigation for future work.

7.2.4.2 Density dependence of LDX iZQC/iDQC

Unlike the temperature coefficient of fat-referenced LDX reported in a paper previously published by our group [124], which was measured at -0.2104ppm/°C, the LDX-methylene iZQC/iDQC frequency was measured using the ultrahigh pressure apparatus to have a temperature coefficient of -0.296ppm/°C. This difference can be attributed to the ^{129}Xe-^{129}Xe interactions described in Chapter 5 which impact the chemical shift of LDX. As shown in Chapter 5, the resonance frequency of LDX starts to show pressure dependence when its concentration exceeds the equivalence of 2 atm. To estimate the concentration of xenon in the WAT/muscle sample, the SNR of spectrum acquired under high xenon pressure were compared to the SNR of the spectrum acquired from the WAT/muscle sample at 1 atm, which is shown in Fig.3.8. Given the partition coefficient of xenon in fatty tissues of 2.06 at room temperature [212], LDX has a concentration of 2.4 amagat in the low-pressure WAT/muscle sample. The ratio of the SNRs of the two spectra, after being adjusted for the number of averages difference, was 47.5. As a result, the xenon concentration in the high-pressure sample can be derived to be about 113.9 amagat. Using Equation 5.9, this concentration will give an extra contribution of about 11.4ppm to the second virial coefficient σ_1. As the lower-pressure sample did not permit the acquisition of iZQC spectrum, the chemical shift difference between LDX and methylene peaks in their respective single pulse spectrum was used as a surrogate (which has been shown in Fig.7.7 as being very close to the LDX-methylene iZQC frequency). The resulting LDX-methylene chemical shift in the high-pressure sample was 12.5ppm higher than that of the low-pressure sample, which is fairly close to the theoretical value and can be considered to be within the range of uncertainty.

7.2.5 Conclusions

In summary, we have shown that the choice of the correlation distance and the specific distribution of water and fat spins at the microscopic level do not affect the iZQC frequency between spins that do mix at the molecular level. The new sequence designed to detect iZQC/iDQC signals between lipid-dissolved ^{129}Xe and methylene proton spins in particular can help to eliminate macro- and microscopic field inhomogeneities, opening the possibility for truly absolute MR thermometry methods.

CHAPTER 8: CONCLUSIONS

In this dissertation, I analyzed the effect of microscopic susceptibility gradients on PRF-based MR thermometry methods. Specifically, I showed that magnetic susceptibility gradients produce a local field perturbation that affects water and fat spins differently, in a manner that strongly depends on the water/fat distribution within the MR imaging voxel. Unless the exact water-fat distribution inside the MR imaging voxel is known, this effect cannot be compensated for.

Since the effect of microscopic susceptibility gradients is even stronger at the microscopic scale, water-fat iZQC frequencies cannot be used to obtain more accurate temperature information than PRF-based thermometry methods, as previously suggested. The value of the water-fat iZQC resonance frequency and its temperature dependence are strongly affected by the distribution of water and fat spins at the microscopic level, more than the fat-referenced PRF frequency. This leads to an extra sequence parameter dependence for iZQC sequence-based MR thermometry, in addition to the tissue dependence that fat-referenced PRF thermometry methods also experience.

At the same time, I also proposed an alternative method to accurately measure temperature in tissues that contain fat. This method takes advantage of the much higher temperature sensitivity of the LDX chemical shift, which is accurately characterized in this work. In addition to its higher temperature coefficient, the possibility of using nearby methylene protons as reference to completely remove the effect of macro and microscopic susceptibility gradients opens up new opportunities for *in vivo* absolute MR thermometry. I also showed that iZQC frequency between LDX and fat spins exhibited less dependence on the particular parameter used in the sequence.

In vivo absolute and relative temperature measurements by LDX-methylene MR thermometry with an accuracy better than 1°C are also demonstrated in rodents and tested in humans. This has demonstrated a great prospect of using this new MR thermal probe to measure absolute temperature.

REFERENCES

[1] Burant, A.; Branca, R. T. *J. Magn. Reson.* **2016**, *273*, 124–129.

[2] Ruset, I. C.; Ph.D. thesis; University of New Hampshire; 2005.

[3] Nikolaou, P.; Goodson, B. M.; Chekmenev, E. Y. *Chem. - A Eur. J.* **2015**, *21*, 3156–3166.

[4] Cleveland, Z. I.; Cofer, G. P.; Metz, G.; Beaver, D.; Nouls, J.; Kaushik, S. S.; Kraft, M.; Wolber, J.; Kelly, K. T.; McAdams, H. P.; Driehuys, B. *PLoS One* **2010**, *5*, e12192.

[5] Marques, J.; Bowtell, R. *Concepts Magn. Reson.* **2005**, *25B*, 65–78.

[6] Galiana, G.; Ph.D. thesis; Princeton University; 2008.

[7] Cheung, T. T. P. *J. Phys. Chem.* **1995**, *99*, 7089–7095.

[8] Granwehr, J.; Urban, J.; Trabesinger, A.; Pines, A. *J. Magn. Reson.* **2005**, *176*, 125–139.

[9] Branca, R. T.; Jenista, E. R.; Warren, W. S. *J. Magn. Reson.* **2011**, *209*, 347–351.

[10] Levitt, M. H. *Spin dynamics: basics of nuclear magnetic resonance*; John Wiley & Sons, Ltd, 2008.

[11] Laukien, D. D.; Weaver, D.; Tschopp, W. H. *Concepts Magn. Reson.* **1994**, *6*, 91–114.

[12] Russell, D. J.; Hadden, C. E.; Martin, G. E.; Gibson, A. A.; Zens, A. P.; Carolan, J. L. *J. Nat. Prod.* **2000**, *63*, 1047–1049.

[13] Kovacs, H.; Moskau, D. *Cryogenic NMR Probes*; Springer Berlin Heidelberg: Berlin, Heidelberg, 2013; pp 392–396.

[14] Wosik, J.; Nesteruk, K.; Tan, I.-C.; Qin, K.; Bankson, J. A. In *Proc. Intl. Soc. Magn. Reson. Med. 23,* **2015**; Toronto, ON; p 1997.

[15] Wijnen, J. P.; van der Kemp, W. J. M.; Luttje, M. P.; Korteweg, M. A.; Luijten, P. R.; Klomp, D. W. J. *Magn. Reson. Med.* **2012**, *68*, 339–348.

[16] Kraff, O.; Fischer, A.; Nagel, A. M.; Mönninghoff, C.; Ladd, M. E. *J. Magn. Reson. Imaging* **2015**, *41*, 13–33.

[17] de Graaf, R. A.; De Feyter, H. M.; Rothman, D. L. *Magn. Reson. Med.* **2015**, *74*, 903–914.

[18] Valkovič, L.; Clarke, W. T.; Purvis, L. A.; Schaller, B.; Robson, M. D.; Rodgers, C. T. *Magn. Reson. Med.* **2016**, 1–7.

[19] Li, S.; An, L.; Yu, S.; Ferraris Araneta, M.; Johnson, C. S.; Wang, S.; Shen, J. *Magn. Reson. Med.* **2016**, *75*, 954–961.

[20] Zhang, X.; Sweedler, J.; Webb, A. *J. Magn. Reson.* **2001**, *153*, 254 – 258.

[21] Webb, A. G.; Van de Moortele, P. F. *NMR Biomed.* **2016**, *29*, 1305–1315.

[22] Ertürk, M. A.; Raaijmakers, A. J.; Adriany, G.; Uurbil, K.; Metzger, G. J. *Magn. Reson. Med.* **2017**, *77*, 884–894.

[23] Walkup, L. L.; Woods, J. C. *NMR Biomed.* **2014**, *27*, 1429–1438.

[24] Rodrigues, T. B.; Serrao, E. M.; Kennedy, B. W. C.; Hu, D.-E.; Kettunen, M. I.; Brindle, K. M. *Nat. Med.* **2014**, *20*, 93–7.

[25] Burns, M. J.; Rayner, P. J.; Green, G. G. R.; Highton, L. A. R.; Mewis, R. E.; Duckett, S. B. *J. Phys. Chem. B* **2015**, *119*, 5020–5027.

[26] Bommerich, U.; Bernarding, J.; Lego, D.; Trantzschel, T.; Plaumann, M. In *Fluorine Magnetic Resonance Imaging*; Pan Stanford Publishing Pte. Ltd., 2016; pp 59–99.

[27] Shchepin, R. V.; Barskiy, D. A.; Coffey, A. M.; Theis, T.; Shi, F.; Warren, W. S.; Goodson, B. M.; Chekmenev, E. Y. *ACS Sensors* **2016**, *1*, 640–644.

[28] Barskiy, D. A.; Coffey, A. M.; Nikolaou, P.; Mikhaylov, D. M.; Goodson, B. M.; Branca, R. T.; Lu, G. J.; Shapiro, M. G.; Telkki, V.-V.; Zhivonitko, V. V.; Koptyug, I. V.; Salnikov, O. G.; Kovtunov, K. V.; Bukhtiyarov, V. I.; Rosen, M. S.; Barlow, M. J.; Safavi, S.; Hall, I. P.; Schröder, L.; Chekmenev, E. Y. *Chem. - A Eur. J.* **2017**, *23*, 725–751.

[29] Killian, T. J. *Phys. Rev.* **1926**, *27*, 578–587.

[30] Benumof, R. *Am. J. Phys.* **1965**, *33*, 151.

[31] Driehuys, B.; Cates, G. D.; Miron, E.; Sauer, K.; Walter, D. K.; Happer, W. *Appl. Phys. Lett.* **1996**, *69*, 1668.

[32] Romalis, M. V.; Miron, E.; Cates, G. D. *Phys. Rev. A* **1997**, *56*, 4569–4578.

[33] Pomeroy, V. R.; Ph.D. thesis; University of New Hampshire; 1998.

[34] Rosen, M. S.; Ph.D. thesis; University of Michigan; 2001.

[35] Happer, W. *Rev. Mod. Phys.* **1972**, *44*, 169–249.

[36] Wagshul, M. E.; Chupp, T. E. *Phys. Rev. A* **1994**, *49*, 3854–3869.

[37] Jau, Y. Y.; Kuzma, N. N.; Happer, W. *Phys. Rev. A* **2004**, *69*, 061401–1.

[38] Pascale, J.; Vandeplanque, J. *J. Chem. Phys.* **1974**, *60*, 2278–2289.

[39] Antonacci, M.; Burant, A.; Wagner, W.; Branca, R. T. *J. Magn. Reson.* **2017**, *279*, 60–67.

[40] Liang, Z.-P. L.; Lauterbur, P. C. *Principles of Magnetic Resonance Imaging: A Signal Processing Perspective*; The Institute of Electrical and Electronics Engineers Press, 1999.

[41] Chmurny, G. N.; Hoult, D. I. *Concepts Magn. Reson.* **1990**, *2*, 131–149.

[42] Hunt, E. R.; Carr, H. Y. *Phys. Rev.* **1963**, *130*, 2302–2305.

[43] Chann, B.; Nelson, I. A.; Anderson, L. W.; Driehuys, B.; Walker, T. G. *Phys. Rev. Lett.* **2002**, *88*, 113201.

[44] Anger, B. C.; Schrank, G.; Schoeck, A.; Butler, K. A.; Solum, M. S.; Pugmire, R. J.; Saam, B. *Phys. Rev. A* **2008**, *78*, 043406.

[45] Cates, G. D.; Schaefer, S. R.; Happer, W. *Phys. Rev. A* **1988**, *37*, 2877–2885.

[46] Rich, D. R.; Gentile, T. R.; Smith, T. B.; Thompson, A. K.; Jones, G. L. *Appl. Phys. Lett.* **2002**, *80*, 2210–2212.

[47] Gemmel, C.; Heil, W.; Karpuk, S.; Lenz, K.; Ludwig, C.; Sobolev, Y.; Tullney, K.; Burghoff, M.; Kilian, W.; Knappe-Grüneberg, S.; Müller, W.; Schnabel, A.; Seifert, F.; Trahms, L.; Baeßler, S. *Eur. Phys. J. D* **2010**, *57*, 303–320.

[48] Tullney, K.; Allmendinger, F.; Burghoff, M.; Heil, W.; Karpuk, S.; Kilian, W.; Knappe-Grüneberg, S.; Müller, W.; Schmidt, U.; Schnabel, A.; Seifert, F.; Sobolev, Y.; Trahms, L. *Phys. Rev. Lett.* **2013**, *111*, 100801.

[49] Repetto, M.; Babcock, E.; Blümler, P.; Heil, W.; Karpuk, S.; Tullney, K. *J. Magn. Reson.* **2015**, *252*, 163–169.

[50] Jameson, C. J.; Jameson, A. K.; Hwang, J. K. *J. Chem. Phys.* **1988**, *89*, 4074–4081.

[51] Mugler, J. P.; Driehuys, B.; Brookeman, J. R.; Cates, G. D.; Berr, S. S.; Bryant, R. G.; Daniel, T. M.; De Lange, E. E.; Downs, J. H.; Erickson, C. J.; Happer, W.; Hinton, D. P.; Kassel, N. F.; Maier, T.; Phillips, C. D.; Saam, B. T.; Sauer, K. L.; Wagshul, M. E. *Magn. Reson. Med.* **1997**, *37*, 809–815.

[52] Möller, H. E.; Chen, X.; Chawla, M. S.; Driehuys, B.; Hedlund, L. W.; Johnson, G. *J. Magn. Reson.* **1998**, *135*, 133–143.

[53] Patz, S.; Hersman, F. W.; Muradian, I.; Hrovat, M. I.; Ruset, I. C.; Ketel, S.; Jacobson, F.; Topulos, G. P.; Hatabu, H.; Butler, J. P. *Eur. J. Radiol.* **2007**, *64*, 335–344.

[54] Zhong, J.; Ruan, W.; Han, Y.; Sun, X.; Ye, C.; Zhou, X. *Sci. Rep.* **2016**, *6*, 25854.

[55] Wolber, J.; Cherubini, A.; Dzik-Jurasz, A. S. K.; Leach, M. O.; Bifone, A. *Proc. Natl. Acad. Sci.* **1999**, *96*, 3664–3669.

[56] Bifone, A.; Song, Y. Q.; Seydoux, R.; Taylor, R. E.; Goodson, B. M.; Pietrass, T.; Budinger, T. F.; Navon, G.; Pines, A. *Proc. Natl. Acad. Sci.* **1996**, *93*, 12932–12936.

[57] Albert, M. S.; Schepkin, V. D.; Budinger, T. F. *J. Comput. Assist. Tomogr.* **1995**, *19*, 975–978.

[58] Albert, M. S.; Balamore, D.; Sakai, K.; Kacher, D.; Walsworth, R. L.; Oteiza, E.; A., J. F. In *Proc. Int. Soc. Magn. Reson. Med. 4,* **1996**; p 1357.

[59] Pauling, L.; Coryell, C. D. *Proc. Natl. Acad. Sci.* **1936**, *22*, 159–163.

[60] Tseng, C.; Peled, S.; Nascimben, L.; Oteiza, E.; Walsworth, R.; Jolesz, F. *J. Magn. Reson.* **1997**, *126*, 79 – 86.

[61] Choquet, P.; Hyacinthe, J. N.; Duhamel, G.; Grillon, E.; Leviel, J. L.; Constantinesco, A.; Ziegler, A. *Magn. Reson. Med.* **2003**, *49*, 1014–1018.

[62] Wagshul, M. E.; Button, T. M.; Li, H. F.; Liang, Z.; Springer, C. S.; Zhong, K.; Wishnia, A. *Magn. Reson. Med.* **1996**, *36*, 183–191.

[63] Durney, C.; Bertolina, J.; Ailion, D.; Christman, R.; Cutillo, A.; Morris, A.; Hashemi, S. *J. Magn. Reson.* **1989**, *85*, 554–570.

[64] Chen, X. J.; Mller, H. E.; Chawla, M. S.; Cofer, G. P.; Driehuys, B.; Hedlund, L. W.; MacFall, J. R.; Johnson, G. A. *Magn. Reson. Med.* **1999**, *42*, 729–737.

[65] Patz, S.; Muradian, I.; Hrovat, M. I.; Ruset, I. C.; Topulos, G.; Covrig, S. D.; Frederick, E.; Hatabu, H.; Hersman, F.; Butler, J. P. *Acad. Radiol.* **2008**, *15*, 713–727.

[66] McRobbie, D. W.; Moore, E. A.; Graves, M. J.; Prince, M. R. *MRI: From Picture to Proton*; Cambridge University Press, 2006.

[67] Torrey, H. C. *Phys. Rev.* **1963**, *130*, 2306–2312.

[68] Miller, K. W.; Reo, N. V.; Schoot Uiterkamp, A. J.; Stengle, D. P.; Stengle, T. R.; Williamson, K. L. *Proc. Natl. Acad. Sci.* **1981**, *78*, 4946–4949.

[69] Chang, Y. V. *Magn. Reson. Med.* **2013**, *69*, 884–890.

[70] Abraham, M. H.; Kamlet, M. J.; Taft, R. W.; Doherty, R. M.; Weathersby, P. K. *J. Med. Chem.* **1985**, *28*, 865–870.

[71] Swanson, S. D.; Rosen, M. S.; Coulter, K. P.; Welsh, R. C.; Chupp, T. E. *Magn. Reson. Med.* **1999**, *42*, 1137–1145.

[72] Kaushik, S. S.; Freeman, M. S.; Yoon, S. W.; Liljeroth, M. G.; Stiles, J. V.; Roos, J. E.; Foster, W. M.; Rackley, C. R.; McAdams, H. P.; Driehuys, B. *J. Appl. Physiol.* **2014**, *117*, 577–85.

[73] Branca, R. T.; He, T.; Zhang, L.; Floyd, C. S.; Freeman, M.; White, C.; Burant, A. *Proc. Natl. Acad. Sci.* **2014**, *111*, 18001–18006.

[74] Goodson, B. M. *J. Magn. Reson.* **2002**, *155*, 157–216.

[75] Kilian, W.; Seifert, F.; Rinneberg, H. *Magn. Reson. Med.* **2004**, *51*, 843–847.

[76] Kershaw, J.; Nakamura, K.; Kondoh, Y.; Wakai, A.; Suzuki, N.; Kanno, I. *Magn. Reson. Med.* **2007**, *57*, 791–797.

[77] Rao, M.; Stewart, N. J.; Norquay, G.; Wild, J. M. In *Proc. Int. Soc. Magn. Reson. Med. 23,* **2015**; p 1445.

[78] Virgincar, R. S.; Robertson, S. H.; Nouls, J.; Degan, S.; Schrank, G. M.; He, M.; Driehuys, B. *Magn. Reson. Med.* **2017**, *77*, 1438–1445.

[79] Robertson, S. H.; Virgincar, R. S.; Bier, E. A.; He, M.; Schrank, G. M.; Smigla, R. M.; Rackley, C.; McAdams, H. P.; Driehuys, B. *Magn. Reson. Med.* **2016**, 1–10.

[80] Jain, M.; Goss, C. H. *Am. J. Respir. Crit. Care. Med.* **2014**, *189*, 1181–1186.

[81] Rao, S. *Arch. Dis. Child.* **2006**, *91*, 786–788.

[82] de Jong, P.; Lindblad, A.; Rubin, L.; Hop, W.; de Jongste, J.; Brink, M.; Tiddens, H. *Thorax* **2006**, *61*, 80–85.

[83] Lange, P.; Halpin, D.; O'Donnell, D.; MacNee, W. *Int. J. Chron. Obstruct. Pulmon. Dis.* **2016**, *11*, 3–12.

[84] Puderbach, M.; Hintze, C.; Ley, S.; Eichinger, M.; Kauczor, H. U.; Biederer, J. *Eur. J. Radiol.* **2007**, *64*, 345–355.

[85] Tibiletti, M.; Bianchi, A.; Stiller, D.; Rasche, V. *NMR Biomed.* **2016**, *29*, 1791–1799.

[86] Ebert, M.; Grossmann, T.; Heil, W.; Otten, E.; Surkau, R.; Thelen, M.; Leduc, M.; Bachert, P.; Knopp, M.; Schad, L. *Lancet* **1996**, *347*, 1297–1299.

[87] Branca, R. T.; Cleveland, Z. I.; Fubara, B.; Kumar, C. S. S. R.; Maronpot, R. R.; Leuschner, C.; Warren, W. S.; Driehuys, B. *Proc. Natl. Acad. Sci.* **2010**, *107*, 3693–3697.

[88] Ouriadov, A. V.; Santyr, G. E. *Magn. Reson. Med.* **2017**.

[89] Couch, M. J.; Ball, I. K.; Li, T.; Fox, M. S.; Ouriadov, A. V.; Biman, B.; Albert, M. S. *NMR Biomed.* **2014**, *27*, 1525–1534.

[90] Halaweish, A. F.; Moon, R. E.; Foster, W. M.; Soher, B. J.; McAdams, H. P.; MacFall, J. R.; Ainslie, M. D.; MacIntyre, N. R.; Charles, H. C. *Chest* **2013**, *144*, 1300–1310.

[91] Wolf, U.; Scholz, A.; Heussel, C. P.; Markstaller, K.; Schreiber, W. G. *Magn. Reson. Med.* **2006**, *55*, 948–951.

[92] Sakai, K.; Bilek, A. M.; Oteiza, E.; Walsworth, R. L.; Balamore, D.; Jolesz, F. A.; Albert, M. S. *J. Magn. Reson. Ser. B* **1996**, *111*, 300–304.

[93] Driehuys, B.; Cofer, G. P.; Pollaro, J.; Mackel, J. B.; Hedlund, L. W.; Johnson, G. A. *Proc. Natl. Acad. Sci.* **2006**, *103*, 18278–18283.

[94] Ebner, L.; Kammerman, J.; Driehuys, B.; Schiebler, M. L.; Cadman, R. V.; Fain, S. B. *Eur. J. Radiol.* **2017**, *86*, 343–352.

[95] Kuethe, D. O.; Caprihan, A.; Gach, H. M.; Lowe, I. J.; Fukushima, E. *J. Appl. Physiol.* **2000**, *88*, 2279–86.

[96] Zhang, L.; Branca, R. T.; He, T.; Ehre, C. In *Proc. Int. Soc. Magn. Reson. Med. 22,* **2014**; p 778.

[97] Mugler, J. P.; Altes, T. A. *J. Magn. Reson. Imaging* **2013**, *37*, 313–331.

[98] Liu, Z.; Araki, T.; Okajima, Y.; Albert, M.; Hatabu, H. *Eur. J. Radiol.* **2014**, *83*, 1282–1291.

[99] Stewart, N. J.; Norquay, G.; Griffiths, P. D.; Wild, J. M. *Magn. Reson. Med.* **2015**, *74*, 346–352.

[100] Ouriadov, A.; Fox, M.; Hegarty, E.; Parraga, G.; Wong, E.; Santyr, G. E. *Magn. Reson. Med.* **2016**, *75*, 2421–2431.

[101] Matin, T. N.; Rahman, N.; Nickol, A. H.; Chen, M.; Xu, X.; Stewart, N. J.; Doel, T.; Grau, V.; Wild, J. M.; Gleeson, F. V. *Radiology* **2017**, *282*, 152299.

[102] Viallon, M.; Berthezne, Y.; Callot, V.; Bourgeois, M.; Humblot, H.; Briguet, A.; Crmillieux, Y. *NMR Biomed.* **2000**, *13*, 207–213.

[103] Lethmate, R.; Ratiney, H.; Wajer, F. T. A. W.; Crémillieux, Y.; van Ormondt, D.; Graveron-Demilly, D. *Magn. Reson. Mater. Phys. Biol. Med.* **2003**, *16*, 21–28.

[104] Kirby, M.; Svenningsen, S.; Owrangi, A.; Wheatley, A.; Farag, A.; Ouriadov, A.; Santyr, G. E.; Etemad-Rezai, R.; Coxson, H. O.; McCormack, D. G.; Parraga, G. *Radiology* **2012**, *265*, 600–610.

[105] Ouriadov, A.; Farag, A.; Kirby, M.; McCormack, D. G.; Parraga, G.; Santyr, G. E. *Magn. Reson. Med.* **2013**, *70*, 1699–1706.

[106] Chang, Y. V.; Quirk, J. D.; Ruset, I. C.; Atkinson, J. J.; Hersman, F. W.; Woods, J. C. *Magn. Reson. Med.* **2014**, *71*, 339–344.

[107] Stewart, N. J.; Leung, G.; Norquay, G.; Marshall, H.; Parra-Robles, J.; Murphy, P. S.; Schulte, R. F.; Elliot, C.; Condliffe, R.; Griffiths, P. D.; Kiely, D. G.; Whyte, M. K.; Wolber, J.; Wild, J. M. *Magn. Reson. Med.* **2015**, *74*, 196–207.

[108] Qing, K.; Mugler, J. P.; Altes, T. A.; Jiang, Y.; Mata, J. F.; Miller, G. W.; Ruset, I. C.; Hersman, F. W.; Ruppert, K. *NMR Biomed.* **2014**, *27*, 1490–1501.

[109] Qing, K.; Ruppert, K.; Jiang, Y.; Mata, J. F.; Miller, G. W.; Shim, Y. M.; Wang, C.; Ruset, I. C.; Hersman, F. W.; Altes, T. A.; Mugler, J. P. *J. Magn. Reson. Imaging* **2014**, *39*, 346–359.

[110] Imai, H.; Kimura, A.; Ito, T.; Fujiwara, H. *Eur. J. Radiol.* **2010**, *73*, 196 – 205.

[111] Wolber, J.; McIntyre, D. J.; Rodrigues, L. M.; Carnochan, P.; Griffiths, J. R.; Leach, M. O.; Bifone, A. *Magn. Reson. Med.* **2001**, *46*, 586–591.

[112] Swanson, S. D.; Rosen, M. S.; Agranoff, B. W.; Coulter, K. P.; Welsh, R. C.; Chupp, T. E. *Magn. Reson. Med.* **1997**, *38*, 695–698.

[113] Burant, A.; Zhang, L.; McCallister, A.; Branca, R. T. In *Proc. 56th ENC Meeting,* **2015**; p 87.

[114] Spence, M. M.; Ruiz, E. J.; Rubin, S. M.; Lowery, T. J.; Winssinger, N.; Schultz, P. G.; Wemmer, D. E.; Pines, A. *J. Am. Chem. Soc.* **2004**, *126*, 15287–15294.

[115] Kunth, M.; Döpfert, J.; Witte, C.; Rossella, F.; Schröder, L. *Angew. Chem. Int. Edn Engl.* **2012**, *51*, 8217–8220.

[116] Spence, M. M.; Rubin, S. M.; Dimitrov, I. E.; Ruiz, E. J.; Wemmer, D. E.; Pines, A.; Yao, S. Q.; Tian, F.; Schultz, P. G. *Proc. Natl. Acad. Sci.* **2001**, *98*, 10654–10657.

[117] Chambers, J. M.; Hill, P. A.; Aaron, J. A.; Han, Z.; Christianson, D. W.; Kuzma, N. N.; Dmochowski, I. J. *J. Am. Chem. Soc.* **2009**, *131*, 563–569.

[118] Döpfert, J.; Witte, C.; Kunth, M.; Schröder, L. *Contrast Media Mol. Imag.* **2014**, *9*, 100–107.

[119] Quinn, S. D.; Gedroyc, W. M. *Int. J. Hyperth.* **2015**, *31*, 272–279.

[120] Chu, K. F.; Dupuy, D. E. *Nat. Rev. Cancer* **2014**, *14*, 199–208.

[121] Peek, M. C. L.; Ahmed, M.; Napoli, A.; ten Haken, B.; McWilliams, S.; Usiskin, S. I.; Pinder, S. E.; van Hemelrijck, M.; Douek, M. *Br. J. Surg.* **2015**, *102*, 873–882.

[122] Schlesinger, D.; Benedict, S.; Diederich, C.; Gedroyc, W.; Klibanov, A.; Larner, J. *Med. Phys.* **2013**, *40*, 080901.

[123] Van Der Zee, J.; Peer-Valstar, J. N.; Rietveld, P. J. M.; De Graaf-Strukowska, L.; Van Rhoon, G. C. *Int. J. Radiat. Oncol. Biol. Phys.* **1998**, *40*, 1205–1212.

[124] Zhang, L.; Burant, A.; McCallister, A.; Zhao, V.; Koshlap, K. M.; Degan, S.; Antonacci, M.; Branca, R. T. *Magn. Reson. Med.* **2016**.

[125] Johnson, F.; Eyring, H.; Stover, B. *Theory of rate processes in biology and medicine*; John Wiley & Sons, New York, 1974.

[126] Chen, J.; Daniel, B. L.; Pauly, K. B. *J. Magn. Reson. Imaging* **2006**, *23*, 430–434.

[127] Cline, H. E.; Schenck, J. F.; Watkins, R. D.; Hynynen, K.; Jolesz, F. A. *Magn. Reson. Med.* **1993**, *30*, 98–106.

[128] Graham, S. J.; Bronskill, M. J.; Henkelman, R. M. *Magn. Reson. Med.* **1998**, *39*, 198–203.

[129] Hynynen, K.; McDannold, N.; Mulkern, R. V.; Jolesz, F. A. *Magn. Reson. Med.* **2000**, *43*, 901–904.

[130] Young, I. R.; Hand, J. W.; Oatridge, A.; Prior, M. V. *Magn. Reson. Med.* **1994**, *32*, 358–369.

[131] Baron, P.; Ries, M.; Deckers, R.; de Greef, M.; Tanttu, J.; Köhler, M.; Viergever, M. A.; Moonen, C. T. W.; Bartels, L. W. *Magn. Reson. Med.* **2014**, *72*, 1057–1064.

[132] Parmala, M.; Eriksson, M.; Rytioja, M.; Tanttu, J.; Köhler, M. *J. Magn. Reson. Imaging* **2016**, *43*, 1171–1178.

[133] Le Bihan, D.; Delannoy, J.; Levin, R. L. *Radiology* **1989**, *171*, 853–857.

[134] Kozak, L.; Bango, M.; Szabo, M.; Rudas, G.; Vidnyanszky, Z.; Nagy, Z. *Acta Paediatr.* **2009**, *99*, 237–43.

[135] Moseley, M. E.; Cohen, Y.; Mintorovitch, J.; Chileuitt, L.; Shimizu, H.; Kucharczyk, J.; Wendland, M. F.; Weinstein, P. R. *Magn. Reson. Med.* **1990**, *14*, 330–346.

[136] Hindman, J. C. *J. Chem. Phys.* **1966**, *44*, 4582.

[137] Schneider, W. G.; Bernstein, H. J.; Pople, J. A. *J. Chem. Phys.* **1958**, *28*, 601–607.

[138] Keutsch, F. N.; Saykally, R. J. *Proc. Nat. Acad. Sci.* **2001**, *98*, 10533–10540.

[139] McDannold, N. *Int. J. Hyperth.* **2005**, *21*, 533–546.

[140] Vigen, K. K.; Daniel, B. L.; Pauly, J. M.; Butts, K. *Magn. Reson. Med.* **2003**, *50*, 1003–1010.

[141] de Zwart, J. A.; Vimeux, F. C.; Delalande, C.; Canioni, P.; Moonen, C. T. *Magn. Reson. Med.* **1999**, *42*, 53–59.

[142] Poorter, J. D. *Magn. Reson. Med.* **1995**, *34*, 359–367.

[143] Stollberger, R.; Ascher, P. W.; Huber, D.; Renhart, W.; Radner, H.; Ebner, F. *J. Magn. Reson. Imaging* **1998**, *8*, 188–196.

[144] Peters, R. D.; Hinks, R. S.; Henkelman, R. M. *Magn. Reson. Med.* **1999**, *41*, 909–918.

[145] Merckel, L. G.; Bartels, L. W.; Köhler, M. O.; van den Bongard, H. J. G. D.; Deckers, R.; Mali, W. P. T. M.; Binkert, C. A.; Moonen, C. T.; Gilhuijs, K. G. A.; van den Bosch, M. A. A. J. *Cardiovasc. Intervent. Radiol.* **2013**, *36*, 292–301.

[146] Baron, P.; Deckers, R.; Bouwman, J. G.; Bakker, C. J. G.; de Greef, M.; Viergever, M. A.; Moonen, C. T. W.; Bartels, L. W. *Magn. Reson. Med.* **2016**, *75*, 1187–1197.

[147] Baron, P.; Deckers, R.; de Greef, M.; Merckel, L. G.; Bakker, C. J.; Bouwman, J. G.; Bleys, R. L.; van den Bosch, M. A.; Bartels, L. W. *Magn. Reson. Med.* **2014**, *72*, 1580–1589.

[148] Rieke, V.; Vigen, K. K.; Sommer, G.; Daniel, B. L.; Pauly, J. M.; Butts, K. *Magn. Reson. Med.* **2004**, *51*, 1223–1231.

[149] de Senneville, B. D.; Mougenot, C.; Moonen, C. T. *Magn. Reson. Med.* **2007**, *57*, 319–330.

[150] Grissom, W. A.; Rieke, V.; Holbrook, A. B.; Medan, Y.; Lustig, M.; Santos, J.; McConnell, M. V.; Pauly, K. B. *Med. Phys.* **2010**, *37*, 5014.

[151] Zou, C.; Shen, H.; He, M.; Tie, C.; Chung, Y.-C.; Liu, X. *Phys. Med. Biol.* **2013**, *58*, 5735–5751.

[152] Zou, C.; Tie, C.; Pan, M.; Wan, Q.; Liang, C.; Liu, X.; Chung, Y.-C. *Phys. Med. Biol.* **2017**, *62*, 1–16.

[153] Kuroda, K.; Oshio, K.; Chung, A. H.; Hynynen, K.; Jolesz, F. A. *Magn. Reson. Med.* **1997**, *38*, 845–851.

[154] Soher, B. J.; Wyatt, C.; Reeder, S. B.; MacFall, J. R. *Magn. Reson. Med.* **2010**, *63*, 1238–1246.

[155] Thrippleton, M. J.; Parikh, J.; Harris, B. A.; Hammer, S. J.; Semple, S. I. K.; Andrews, P. J. D.; Wardlaw, J. M.; Marshall, I. *NMR Biomed.* **2013**, *27*, 183–190.

[156] Corbett, R. J.; Purdy, P. D.; Laptook, a. R.; Chaney, C.; Garcia, D. *Am. J. Neuroradiol.* **1999**, *20*, 1851–7.

[157] Dehkharghani, S.; Mao, H.; Howell, L.; Zhang, X.; Pate, K. S.; Magrath, P. R.; Tong, F.; Wei, L.; Qiu, D.; Fleischer, C.; Oshinski, J. N. *Am. J. Neuroradiol.* **2015**, *36*, 1128–1135.

[158] Lagemaat, M. W.; Breukels, V.; Vos, E. K.; Kerr, A. B.; Van Uden, M. J.; Orzada, S.; Bitz, A. K.; Maas, M. C.; Scheenen, T. W. J. *Magn. Reson. Med.* **2016**, *75*, 933–945.

[159] Odéen, H.; Todd, N.; Diakite, M.; Minalga, E.; Payne, A.; Parker, D. L. *Med. Phys.* **2014**, *41*, 092301.

[160] McDannold, N.; Hynynen, K.; Oshio, K.; Mulkern, R. V. *Med. Phys.* **2001**, *28*, 346.

[161] Liu, G.; Qin, Q.; Chan, K. W. Y.; Li, Y.; Bulte, J. W. M.; McMahon, M. T.; van Zijl, P. C. M.; Gilad, A. A. *NMR Biomed.* **2014**, *27*, 320–331.

[162] Sprinkhuizen, S. M.; Bakker, C. J. G.; Bartels, L. W. *Magn. Reson. Med.* **2010**, *64*, 239–248.

[163] Majumdar, S. *Magn. Reson. Med.* **1991**, *22*, 101–110.

[164] Majumdar, S.; Thomasson, D.; Shimakawa, A.; Genant, H. K. *Magn. Reson. Med.* **1991**, *22*, 111–127.

[165] Salomir, R.; de Senneville, B. D.; Moonen, C. T. *Concepts Magn. Reson.* **2003**, *19B*, 26–34.

[166] Deville, G.; Bernier, M.; Delrieux, J. M. *Phys. Rev. B* **1979**, *19*, 5666–5688.

[167] Hopkins, J. A.; Wehrli, F. W. *Magn. Reson. Med.* **1997**, *37*, 494–500.

[168] Jones, J. R.; Rowlands, D. L. G.; Monk, C. B. *Trans. Faraday Soc.* **1965**, *61*, 1384–1388.

[169] Sprinkhuizen, S. M.; Konings, M. K.; van der Bom, M. J.; Viergever, M. A.; Bakker, C. J. G.; Bartels, L. W. *Magn. Reson. Med.* **2010**, *64*, 1360–1372.

[170] Vathyam, S.; Lee, S.; Warren, W. S. *Science* **1996**, *272*, 92–96.

[171] Zhang, L.; McCallister, A.; Koshlap, K. M.; Branca, R. T. *Magn. Reson. Med.* **2017**.

[172] Goldman, M. *Quantum description of high resolution NMR in liquids*; Oxford University Press: New York, 1988.

[173] Richter, W.; Warren, W. S. *Concepts Magn. Reson.* **2000**, *12*, 396–409.

[174] Warren, W.; Richter, W.; Andreotti, A.; Farmer, B. *Science* **1993**, *262*, 2005–2009.

[175] Wang, J. H. *J. Phys. Chem.* **1965**, *69*, 4412–4412.

[176] Branca, R. T.; Galiana, G.; Warren, W. S. *J. Chem. Phys.* **2008**, *129*, 054502.

[177] Warren, W. S. *Science* **1998**, *281*, 247–251.

[178] Bowtell, R.; Gutteridge, S.; Ramanathan, C. *J. Magn. Reson.* **2001**, *150*, 147–155.

[179] Balla, D. Z.; Faber, C. *Magn. Reson. Mater. Physics, Biol. Med.* **2007**, *20*, 183–191.

[180] de Graaf, R. A.; Rothman, D. L.; Behar, K. L. *J. Magn. Reson.* **2007**, *187*, 320–326.

[181] Cho, J.-H.; Ahn, S.; Lee, C.; Hong, K. S.; Chung, K.-C.; Chang, S.-K.; Cheong, C.; Warren, W. S. *Magn. Reson. Imaging* **2007**, *25*, 626–633.

[182] Richter, W.; Richter, M.; Warren, W. S.; Merkle, H.; Andersen, P.; Adriany, G.; Ugurbil, K. *Magn. Reson. Imaging* **2000**, *18*, 489–494.

[183] Schäfer, A.; Möller, H. E. *Magn. Reson. Med.* **2007**, *58*, 696–704.

[184] Schneider, J. T.; Faber, C. *Magn. Reson. Med.* **2008**, *60*, 850–859.

[185] Branca, R. T.; Warren, W. S. *Magn. Reson. Med.* **2011**, *65*, 313–319.

[186] Bao, J.; Cui, X.; Cai, S.; Zhong, J.; Cai, C.; Chen, Z. *NMR Biomed.* **2013**, *26*, 1663–1671.

[187] Branca, R. T.; Zhang, L.; Warren, W. S.; Auerbach, E.; Khanna, A.; Degan, S.; Ugurbil, K.; Maronpot, R. *PLoS One* **2013**, *8*, e74206.

[188] Balla, D.; Faber, C. *Chem. Phys. Lett.* **2004**, *393*, 464–469.

[189] Faber, C.; Pracht, E.; Haase, A. *J. Magn. Reson.* **2003**, *161*, 265–274.

[190] Lin, Y.; Chen, Z.; Cai, C.; Chen, Z. *Spectrochim. Acta Part A Mol. Biomol. Spectrosc.* **2008**, *70*, 1025–1028.

[191] Chen, Z.; Cai, S.; Chen, Z.; Zhong, J. *J. Chem. Phys.* **2009**, *130*, 084504.

[192] Huang, Y.; Cai, S.; Chen, X.; Chen, Z. *J. Magn. Reson.* **2010**, *203*, 100–107.

[193] Lin, Y.; Gu, T.; Chen, Z.; Kennedy, S.; Jacob, M.; Zhong, J. *Magn. Reson. Med.* **2010**, *63*, 303–311.

[194] Lin, Y.-Y.; Ahn, S.; Murali, N.; Brey, W.; Bowers, C. R.; Warren, W. S. *Phys. Rev. Lett.* **2000**, *85*, 3732–3735.

[195] Zhang, Z.; Huang, Y.; Smith, P. E.; Wang, K.; Cai, S.; Chen, Z. *J. Magn. Reson.* **2014**, *242*, 49–56.

[196] Jiang, B.; Liu, H.; Liu, M.; Ye, C.; Mao, X. *J. Chem. Phys.* **2007**, *126*, 054502.

[197] Scruggs, B. E.; Gleason, K. K. *J. Magn. Reson.* **1992**, *99*, 149–160.

[198] Meriles, C.; Dong, W. *J. Magn. Reson.* **2006**, *181*, 331–335.

[199] Jenista, E. R.; Galiana, G.; Branca, R. T.; Yarmolenko, P. S.; Stokes, A. M.; Dewhirst, M. W.; Warren, W. S. *J. Magn. Reson.* **2010**, *204*, 208–218.

[200] Davis, R. M.; Warren, W. S. *Magn. Reson. Med.* **2015**, *74*, 63–70.

[201] Galiana, G.; Branca, R. T.; Jenista, E. R.; Warren, W. S. *Science* **2008**, *322*, 421–424.

[202] Jenista, E. R.; Branca, R. T.; Warren, W. S. *Int. J. Hyperth.* **2010**, *26*, 725–734.

[203] Davis, R. M.; Zhou, Z.; Chung, H.; Warren, W. S. *Magn. Reson. Med.* **2016**, *75*, 1958–1966.

[204] Garrett-Roe, S.; Warren, W. S. *J. Magn. Reson.* **2000**, *146*, 1–13.

[205] Branca, R. T.; Capuani, S.; Maraviglia, B. *Concepts Magn. Reson.* **2004**, *21A*, 22–36.

[206] Bernard, C. P.; Liney, G. P.; Manton, D. J.; Turnbull, L. W.; Langton, C. M. *J. Magn. Reson. Imaging* **2008**, *27*, 192–197.

[207] Cannon, B.; Nedergaard, J. *Physiol. Rev.* **2004**, *84*, 277–359.

[208] Lundström, E.; Strand, R.; Johansson, L.; Bergsten, P.; Ahlström, H.; Kullberg, J. *PLoS One* **2015**, *10*, e0126705.

[209] Stahl, V.; Maier, F.; Freitag, M. T.; Floca, R. O.; Berger, M. C.; Umathum, R.; Berriel Diaz, M.; Herzig, S.; Weber, M.-A.; Dimitrakopoulou-Strauss, A.; Rink, K.; Bachert, P.; Ladd, M. E.; Nagel, A. M. *J. Magn. Reson. Imaging* **2017**, *45*, 369–380.

[210] Schilling, F.; Schröder, L.; Palaniappan, K. K.; Zapf, S.; Wemmer, D. E.; Pines, A. *ChemPhysChem* **2010**, *11*, 3529–3533.

[211] Sears, D. N.; Jameson, C. J. *J. Chem. Phys.* **2003**, *119*, 12231.

[212] Clever, H. L. *Fluid Phase Equilib.* **1980**, *4*, 315–316.

[213] Venkatesh, A.; Kacher, D. K.; Kuroda, K.; Balamore, D.; Jolesz, F.; Albert, M. In *Proc. Int. Soc. Magn. Reson. Med. 9,* **2001**; p 2194.

[214] Kanegsberg, E.; Pass, B.; Carr, H. Y. *Phys. Rev. Lett.* **1969**, *23*, 572–574.

[215] Jameson, C. J.; Sears, D. N.; de Dios, A. C. *J. Chem. Phys.* **2003**, *118*, 2575.

[216] Stueber, D.; Jameson, C. J. *J. Chem. Phys.* **2004**, *120*, 1560.

[217] Jameson, C. J.; Stueber, D. *J. Chem. Phys.* **2004**, *120*, 10200.

[218] Jameson, C. J.; de Dios, A. C. *J. Chem. Phys.* **1992**, *97*, 417.

[219] Hore, P. *Nuclear magnetic resonance*; Oxford University Press, 1995.

[220] Buckingham, A. D. *Can. J. Chem.* **1960**, *38*, 300–307.

[221] Rummens, F. H. *J. Chim. Phys. & Phys.-Chim. Biol.* **1975**, *72*, 448–452.

[222] Dejaegere, A.; Claessens, M.; Luhmer, M.; Bardiaux, M.; Reisse, J. *J. Phys. Chem.* **1988**, *92*, 7093–7097.

[223] Luhmer, M.; Bartik, K. *J. Phys. Chem. A* **1997**, *101*, 5278–5283.

[224] Lim, Y. H.; King, A. D. *J. Phys. Chem.* **1993**, *97*, 12173–12177.

[225] Lim, Y. H.; Nugara, N.; King, A. D. *Appl. Magn. Reson.* **1995**, *8*, 521–534.

[226] Bonifacio, R. P.; Filipe, E. J. M.; Nunes, T. G. In *XEMAT2000,* **2000**; Sestri Levante, Italy; p 1.

[227] Ripmeester, J. A.; Ratcliffe, C. I. *J. Phys. Chem.* **1990**, *94*, 7652–7656.

[228] Kromhout, R. A.; Linder, B. *J. Magn. Reson.* **1969**, *1*, 450–463.

[229] Saunavaara, J.; Jokisaari, J. *J. Magn. Reson.* **2006**, *180*, 58–62.

[230] Ylihautala, M.; Lounila, J.; Jokisaari, J. *J. Chem. Phys.* **1999**, *110*, 6381–6388.

[231] Adrian, F. *Chem. Phys. Lett.* **1970**, *7*, 201–204.

[232] Jameson, C. J.; Jameson, A. K.; Cohen, S. M. *J. Chem. Phys.* **1973**, *59*, 4540.

[233] Sears, D. N.; Jameson, C. J. *J. Chem. Phys.* **2004**, *121*, 2151.

[234] Jameson, C. J. *J. Chem. Phys.* **1975**, *63*, 5296–5301.

[235] Jameson, C. J.; Jameson, A. K.; Cohen, S. M. *J. Chem. Phys.* **1975**, *62*, 4224–4226.

[236] Jameson, C. J.; Keith Jameson, A. *Mol. Phys.* **1971**, *20*, 957–959.

[237] Steward, A.; Allott, P. R.; Cowles, A. L.; Mapleson, W. W. *Br. J. Anaesth.* **1973**, *45*, 282–93.

[238] Nouls, J.; Fanarjian, M.; Hedlund, L.; Driehuys, B. *Concepts Magn. Reson.* **2011**, *39B*, 78–88.

[239] Rao, M.; Stewart, N. J.; Norquay, G.; Griffiths, P. D.; Wild, J. M. *Magn. Reson. Med.* **2016**, *75*, 2227–2234.

[240] Miller, G. W.; Cates Jr., Gordon, D.; Keder, D.; Altes, T. A.; Mata, J. F.; Qing, K.; Ruset, I.; Hersman, F. W.; Mugler III, J. P. In *Proc. Intl. Soc. Magn. Reson. Med.*; p 1182.

[241] Nicholls, D. G.; Locke, R. M. *Physiol. Rev.* **1984**, *64*, 1–64.

[242] Aherne, W.; Hull, D. *J. Pathol. Bacteriol.* **1966**, *91*, 223–234.

[243] Chechi, K.; Nedergaard, J.; Richard, D. *Obes. Rev.* **2014**, *15*, 92–106.

[244] Bartelt, A.; Bruns, O. T.; Reimer, R.; Hohenberg, H.; Ittrich, H.; Peldschus, K.; Kaul, M. G.; Tromsdorf, U. I.; Weller, H.; Waurisch, C.; Eychmüller, A.; Gordts, P. L. S. M.; Rinninger, F.; Bruegelmann, K.; Freund, B.; Nielsen, P.; Merkel, M.; Heeren, J. *Nat. Med.* **2011**, *17*, 200–205.

[245] Matsushita, M.; Yoneshiro, T.; Aita, S.; Kameya, T.; Sugie, H.; Saito, M. *Int. J. Obes.* **2014**, *38*, 812–817.

[246] Mukherjee, J.; Baranwal, A.; Schade, K. *Curr. Diabetes Rev.* **2016**, *12*, 414–428.

[247] Schrauwen, P.; van Marken Lichtenbelt, W. D.; Spiegelman, B. M. *Diabetologia* **2015**, *58*, 1704–1707.

[248] Thurlby, P. L.; Trayhurn, P. *Pflugers Arch.* **1980**, *385*, 193–201.

[249] Zhang, L.; Antonacci, M.; Burant, A.; McCallister, A.; Branca, R. T. *in preparation*.

[250] Cohade, C.; Osman, M.; Pannu, H. K.; Wahl, R. L. *J. Nucl. Med.* **2003**, *44*, 170–6.

[251] Zhang, L.; Antonacci, M.; Burant, A.; Koshlap, K. M.; Branca, R. T. *J. Chem. Phys.* **2016**, *145*, 194201.

[252] Augustine, M. P.; Zilm, K. W. *J. Magn. Reson. Ser. A* **1996**, *123*, 145–156.

[253] Bowtell, R. *J. Magn. Reson.* **1992**, *100*, 1–17.

[254] Lee, S.; Richter, W.; Vathyam, S.; Warren, W. S. *J. Chem. Phys.* **1996**, *105*, 874.

[255] Xiang, B. *Concepts Magn. Reson. Part A* **1999**, *11*, 393–408.

[256] Hoult, D.; Richards, R. *J. Magn. Reson.* **1976**, *24*, 71–85.

[257] Nikolaou, P.; Coffey, A. M.; Walkup, L. L.; Gust, B. M.; Whiting, N.; Newton, H.; Barcus, S.; Muradyan, I.; Dabaghyan, M.; Moroz, G. D.; Rosen, M. S.; Patz, S.; Barlow, M. J.; Chekmenev, E. Y.; Goodson, B. M. *Proc. Natl. Acad. Sci.* **2013**, *110*, 14150–14155.

[258] Huang, S. Y.; Lin, Y.-Y.; Lisitza, N.; Warren, W. S. *J. Chem. Phys.* **2002**, *116*, 10325.

[259] Osburn, J. O.; Stitzell, J. A.; Peterson, R. E. *J. Appl. Physiol.* **1969**, *27*, 624–9.